Université catholique de Louvain
Faculté des Sciences
Département de Physique
Unité de physique théorique et de physique mathématique
Centre for Particle Physics and Phenomenology

Quarkonium production phenomenology

Doctoral dissertation presented by

Pierre Artoisenet

in fulfilment of the requirements for the degree of Doctor in Sciences

Prof. F. Maltoni (Advisor)	UCL
Prof. D. Favart (Chairman)	UCL
Prof. G. Bruno	UCL
Prof. J. Weyers	UCL
Prof. N. Brambilla	TU Munich
Prof. M. Kraemer	RTWH Aachen
Prof. G. Bodwin	ANL Chicago

July 2009

Remerciements

Cette thèse est le fruit de divers projets réalisés en collaboration avec Eric Braaten, John Campbell, Jean-Philippe Lansberg, Fabio Maltoni, Tim Stelzer, et Francesco Tramontano. C'est avec plaisir que je les remercie tous vivement pour les interactions enrichissantes sur lesquelles ce travail prend appui.

Je tiens à remercier plus particulièrement mon promoteur de thèse, le professeur Fabio Maltoni. L'excellence de son encadrement tient à ses nombreuses qualités, tant au niveau scientifique que humain. Son dynamisme, son enthousiame, son esprit critique, sa disponibilité, sa rigueur ont apporté un support formidable à l'élaboration de cette thèse, dans une atmosphère stimulante dont il a le secret. Merci aussi pour les nombreuses opportunités de voyage dont j'ai bénéficié afin de présenter nos résultats lors de rencontres internationales.

Je remercie également tous les membres de mon jury ainsi que le professeur Jean-Marc Gérard pour leur enthousiasme et leur lecture attentive de ma thèse. Merci en particulier au professeur Geoffrey Bodwin pour l'aide dont j'ai bénéficié lors de la rédaction de ma thèse, et pour son hospitalité lors de mon séjour au Argonne National Laboratory.

Je remercie le Fonds de la Recherche Scientifique - FNRS qui a assuré le soutien financier de cette thèse.

Au cours de mon doctorat, j'ai eu le plaisir de travailler avec Olivier Mattelaer sur un projet annexe. Merci pour cette collaboration agréable et fructueuse. Merci également à Vincent Lemaître et à mon promoteur d'avoir supervisé ce projet.

Au quotidien de mon travail, j'ai également profité de l'aide précieuse des membres de l'équipe CP3, dont l'expertise et la disponibilité ont assuré un environement propice au développement de ma thèse. Merci à tous pour les nombreuses discussions enrichissantes de ces dernières années. Merci en particulier à Vincent Boucher, qui,

aussi serviable qu'efficace, a volé à mon secours à maintes reprises pour résoudre mes problèmes informatiques. Merci à Thomas Keutgen, Fabrice Charlier, Pavel Demin, et Fabian Boldrin pour leur support relatif au réseau informatique Fynu et à l'utilisation des clusters Ingrid et Fynu. Merci également aux secrétaires Ginette Tabordon, Carine Baras et Cathy Brichard pour leur aide pratique.

Merci à mes amis et à ma famille pour leur soutien en toute circonstance. Merci à Emma qui a gentillement accepté de vérifier l'orthographe du texte de ma thèse. Merci à mon épouse, Laure-Anne, pour l'élan d'amour et d'énergie qu'elle m'apporte chaque jour.

Contents

Introduction

The study of heavy-quarkonium states started with the discovery of the first charmonium states in 1974 [1, 2] and bottomonium states in 1977 [3]. Since then, many experiments have been dedicated to the analysis of the spectrum of quarkonia, and new states are still discovered nowadays. As a recent example, the η_b, i.e. the lowest state in the bottomonium system, has only been discovered for the first time in 2008 by the BABAR collaboration [4]. In addition to predicted quarkonium states, other exotic states have been found, whose interpretation is still unclear (see for example [5]).

On the theoretical side, heavy-quarkonium bound states provide a very rich ground to to probe QCD, the $SU(3)$ gauge theory of the strong interactions. Even if the confinement effects are not tractable from first principles, the mass of the heavy quarks provides us with a high scale that legitimates the use of perturbative techniques, by virtue of the asymptotic freedom behavior of QCD. Many properties of heavy quarkonium spectra, including the striking narrow width of the J/ψ, can be explained within this framework.

The use of perturbative QCD in the prediction of heavy-quarkonium production or decay rates is based on a factorization principle, that isolates the low-energy non-perturbative effects into a set of universal parameters in the expression of the rates. One of the first attempts at such a factorization procedure is the Color-Singlet Model (CSM) [6, 7, 8], in which the perturbative heavy quarks are assumed to be created on-shell, with the same quantum numbers as the physical quarkonium state. The total rate is expressed as the product of a process-dependent factor associated with the creation or the annihilation of the perturbative heavy quarks, and a universal factor that takes into account the transition between the heavy quarks and the physical quarkonium. Usually, this last factor is approximated by the value of a Schrödinger wave function at the origin, or its derivatives.

The CSM gives a simple prescription for the computation of the rates and is very predictive, but it has a certain number of drawbacks. For S-wave quarkonium decays, calculation beyond the static approximation revealed a very large relativistic correction at order v^2 [9], with v the velocity of the heavy quark in the quarkonium rest frame. As the CSM does not provide a correct prescription to compute the relativistic corrections in general, higher correction terms are a priori not under control. The situation is even worst for the P-waves, where the presence of infrared divergences appearing at higher orders in α_s explicitly breaks the validity of the factorization procedure adopted by the CSM.

In the search for a more rigorous factorization procedure, the theory of Non-Relativistic QCD was introduced in 1994 [10]. In this theory, perturbative amplitudes are systematically expanded in powers of v. In this approach, transitions in which the perturbative heavy-quark pair is created in a different quantum state than the physical quarkonium are also included, as such transitions arise naturally in the v expansion. For each transition $Q\bar{Q}(n) \to \mathcal{Q}$, a non-perturbative parameter enters in the expression of the decay/production rate. In NRQCD, these parameters, also called long-distance matrix elements (shortened as LDME), have a precise definition in terms of vacuum expectation of quantum field operators. They encode the low energy effects associated to the evolution of the heavy-quark pair into a quarkonium state. The infrared divergences that arise in the computation of the perturbative factors are consistently reabsorbed into these long-distance matrix elements through a matching procedure. As a result, one can properly handle the computation of quarkonium rates beyond the leading order in α_s. In particular, the QCD corrections to P-wave decay/production rates are then tractable [11, 12].

Despite its theoretical appeal and the undeniable successes, not all the predictions of the NRQCD factorization approach have been firmly established, and the experimental evidence of the universality of the LDME's still requires further phenomenological investigation. Among the questions still open stands the relevance of the color-octet contributions in the J/ψ production: they seem to play a dominant role at the Tevatron and in $\gamma\gamma$ collisions, but they look marginal at e^+e^- at low energy, in photoproduction at HERA [13] and in fixed-target experiments [14]. Moreover, NRQCD predicts a sizeable transverse polarization for J/ψ 's at high-p_T at the Tevatron, in contrast to the latest data, which now clearly indicate that J/ψ's are not transversely polarized [15].

Given such a puzzling landscape, it is mandatory to re-examine in detail the key observables and the corresponding theoretical predictions and to try to improve systematically upon them. The estimation of the impact of the transitions at work for quarkonium production relies on the accuracy with which the corresponding short-distance coefficients can be computed. Cross sections at leading order in α_S and v are normally affected by very large uncertainties and cannot give a reliable estimate of the yield. In

these cases, it can be problematic to gather information on the underlying production mechanism(s) from data. A first direction of research that has been followed in this thesis is the computation of higher-order corrections for specific processes, and the investigation of their phenomenological implications.

The second way to gain further insight on the mechanisms at work in quarkonium production is to extend the set of the typical observables that have been analyzed analyzed so far, not only by studying new processes but also by making predictions for more exclusive observables. Experimental analyses of potentially interesting new ideas can be simulated with the support of a multi-purpose matrix element based generator. This new generation of codes, which have become widely available recently, are born to ease phenomenology studies at colliders. They are able to create automatically the matrix elements corresponding to a given process and then to generate unweighted parton-level events that can be passed to standard Monte Carlo programs such as Pythia [16] or Herwig [17], for showering and hadronization, and eventually to detector simulation. As a second direction in this thesis, we present the work that we have done in the construction of an event generator for quarkonium production. Various examples of application of such a tool are given in details.

The thesis is organized as follows. In the first chapter, we review the concepts of the NRQCD theory, emphasing the features to keep in mind for the next chapters. In chapter 2, we present the techniques that we have developed to study physical observables in the framework of NRQCD. In chapter 3, we present our new results for quarkonium production at B-factories, at the Tevatron and LHC hadron colliders, and at HERA. We finally give our conclusion. Most of the results presented here can be found in the following publications:

- Charm-pair Rescattering Mechanism for Charmonium Production in High-energy Collisions.
  P. Artoisenet and E. Braaten.
  arXiv:0907.0025

- J/ψ production at HERA.
  P. Artoisenet, John M. Campbell, F. Maltoni, and F. Tramontano.
  Published in Phys. Rev. Lett., 102:142001, 2009.

- Υ Production at Fermilab Tevatron and LHC Energies.
  P. Artoisenet, John M. Campbell, J. P. Lansberg, F. Maltoni, and F. Tramontano.
  Published in Phys. Rev. Lett., 101:152001, 2008.

- Automatic generation of quarkonium amplitudes in NRQCD.
  P. Artoisenet, F. Maltoni, and T. Stelzer.
  Published in JHEP, 02:102, 2008.

- Hadroproduction of J/ψ and in association with a heavy-quark pair.
  P. Artoisenet, J. P. Lansberg, and F. Maltoni.
  Published in Phys. Lett., B653:60-66, 2007.

as well as in several conference proceedings [18, 19, 20, 21]. Some aspects are expanded in more detail, such as the spin correlation effects in the decay of vector-like quarkonium states (Section 2.2), the validity of the fragmentation approximation (Section 2.3), the Monte Carlo techniques (Section 2.4), the J/ψ hadroproduction in association with a charm-quark pair at the LHC (Section 3.3). We also present here for the first time some original results for the relativistic corrections to the inclusive J/ψ production in e^+e^- annihilation (Section 3.1).

Chapter 1

Quarkonium production in NRQCD

After several models had been proposed for the computation of heavy-quarkonium cross sections such as the color-singlet model or the color- evaporation model, a rigorous formalism that legitimates the use of perturbative QCD in heavy quarkonium physics has been provided with the theory of NRQCD [10]. As this theory is the reference theoretical ground for the work presented in this thesis, we review in this chapter the important features of the formalism that should be kept in mind in the next chapters. In Section 1.1, we recall the steps leading to the factorized expression of the cross section into a sum of products of short-distance coefficients and long-distance matrix elements. The general techniques for the computation of the short-distance coefficients are presented in Section 1.2. We next review some important properties of the long-distance matrix elements in Section 1.3. In the last Section of this chapter, we briefly discuss recent work on the investigation of the proof of the factorization theorem on which the NRQCD expansion is based.

1.1 NRQCD factorization

The production of quarkonium states is a multi-scale process. On the one hand, the creation of the heavy-quark pair involves energy scales of order m_Q of larger. On the other hand, the dynamics of the quarkonium state is characterized by much lower energy scales: if we denote by v the velocity of the heavy quark in the bound-state rest frame, the relative momentum between the quarks is of the order of vm_Q, and the

binding energy is of the order of $v^2 m_Q$. To the extend that v is a small parameter for heavy quarkonium states, these three scales are relatively well separated. The value of v^2 is of the order of 0.1 for the bottomonium ground state, and of the order of 0.3 for the charmonium ground state.

Provided that the mass of the heavy quark is much larger than $\Lambda_{\rm QCD}$, the creation of a heavy-quark pair involves a large energy scale at which the strong coupling constant can be treated as an expansion parameter. Hence one may hope to use perturbative techniques to calculate the rate of production of a heavy-quark pair [1]. However, the rate of production of heavy-quarkonium states also involves effects from the low-energy scales $v m_Q$, $v^2 m_Q$ associated with the dynamics of the quarkonium state. These effects cannot be handled by the formalism of perturbative QCD. Nevertheless, if high- and low-energy scales are well separated, one expects the dynamics of the bound state to be rather insensitive to the details of the creation of the heavy-quark pair. Indeed, the wave length associated with the bound state dynamics $\approx 1/v m_Q$ is too long to resolve the spatial extension $\approx 1/m_Q$ associated with the creation of the heavy-quark pair. Provided that v is sufficiently small, the creation of the heavy-quark pair appears to be almost point-like compared to the size of the bound state, and one expects to be able to factorize high-energy effects from low-energy effects in the production rate in a process-independent way.

The framework of effective field theories provides a powerful prescription to disentangle different energy scales. Non-Relativistic QCD (NRQCD) is the effective field theory that separates high-energy scales of order m_Q or higher from low-energy scales in quarkonium production or annihilation rates. The NRQCD Lagrangian is derived from the QCD Lagrangian by integrating out energy-momentum modes of order m_Q or higher. The resulting dynamical fields associated with the heavy quark and anti-quark are expressed in terms of two-component Pauli spinors ψ and χ, which correspond to the upper and lower components of the Dirac fields, respectively. The effective Lagrangian has a UV cutoff $\Lambda \sim m_Q$, that plays the rôle of a factorization scale. Energy-momentum modes above this factorization scale are encoded into the coupling constants of local operators, similar to the way in which the coupling constant G_F of a local 4-fermion interaction encodes the high energy modes of order M_W in the Fermi effective theory of the muon decay.

More precisely, the NRQCD Lagrangian has the following form

$$\mathcal{L} = \mathcal{L}_{\rm light} + \mathcal{L}_{\rm heavy} + \delta\mathcal{L}\,. \tag{1.1}$$

In this expression, the first term accounts for the low energy modes associated with the gluon and the light quarks. The term $\mathcal{L}_{\rm heavy}$ describes the low-momentum modes

[1] The perturbation expansion may be spoiled by soft gluon exchange between the heavy-quark pair and the other partons in the creation process, an issue that is addressed in the factorization of the different energy scales.

associated with the heavy quarks

$$\mathcal{L}_{\rm heavy} \;=\; \psi^\dagger \left(iD_t + \frac{\mathbf{D}^2}{2M} \right) \psi \;+\; \chi^\dagger \left(iD_t - \frac{\mathbf{D}^2}{2M} \right) \chi, \tag{1.2}$$

where ψ is the Pauli spinor field that annihilates a heavy quark, χ is the Pauli spinor field that creates a heavy anti-quark, D_t and $\boldsymbol{D}$ are the time and space components of the gauge covariant derivative D^μ. Spin and color indices are understood. High energy-momentum modes in the quarkonium rest frame correspond to the propagation of highly virtual states over short distances, and are incorporated in the NRQCD Lagrangian through local operators represented by the term $\delta\mathcal{L}$ in Eq. (1.1). By systematically including operators of higher dimension, the Green functions resulting from the NRQCD Lagrangian approximate the corresponding Green functions computed in the full QCD theory up to an arbitrary high order in v, the heavy quark velocity in the quarkonium rest frame. Provided that v is a small parameter, the expansion of the Green functions in v can be truncated within a certain accuracy, which corresponds to keep a finite number of terms in the NRQCD Lagrangian.

This procedure applies also to the computation of quarkonium production rates. The inclusive production process for a quarkonium H is accounted for in the NRQCD Lagrangian through the introduction of 4-fermion operators that have the general form

$$\mathcal{O}_n = \chi^\dagger \kappa_n \psi a_H^\dagger a_H(\Lambda) \psi^\dagger \kappa_n \chi \,, \tag{1.3}$$

where $a_H^\dagger a_H$ is the projector onto states that in the asymptotic future contain the quarkonium H plus light partons X

$$a_H^\dagger a_H(\Lambda) = \sum_X |H + X, t \to \infty\rangle\langle|H + X, t \to \infty|, \tag{1.4}$$

and the factorization scale Λ acts as a cutoff of the high energy modes[2]. The factors $\mathcal{K}_n$ and $\mathcal{K}'_n$ in Eq. (1.3) are products of a color matrix (either the unit matrix or T^a), a spin matrix (either the unit matrix or σ^i), and a polynomial in the covariant derivative $\mathbf{D}$ and other fields. These operators are evaluated in the quarkonium rest frame and have definite scaling with v. The operators of dimension 6 are

$$\mathcal{O}_1^H(^1S_0) \;=\; \chi^\dagger \psi \left(a_H^\dagger a_H \right) \psi^\dagger \chi, \tag{1.5}$$

$$\mathcal{O}_1^H(^3S_1) \;=\; \chi^\dagger \sigma^i \psi \left(a_H^\dagger a_H \right) \psi^\dagger \sigma^i \chi, \tag{1.6}$$

$$\mathcal{O}_8^H(^1S_0) \;=\; \chi^\dagger T^a \psi \left(a_H^\dagger a_H \right) \psi^\dagger T^a \chi, \tag{1.7}$$

$$\mathcal{O}_8^H(^3S_1) \;=\; \chi^\dagger \sigma^i T^a \psi \left(a_H^\dagger a_H \right) \psi^\dagger \sigma^i T^a \chi. \tag{1.8}$$

[2]It is understood that the projector in Eq. (1.4) is evaluated in the quarkonium rest frame.

The most relevant operators of dimension 8 for the phenomenology are

$$\mathcal{O}_1^H(^1P_1) = \chi^\dagger(-\tfrac{i}{2}\overleftrightarrow{D}^i)\psi\left(a_H^\dagger a_H\right)\psi^\dagger(-\tfrac{i}{2}\overleftrightarrow{D}^i)\chi, \quad (1.9)$$

$$\mathcal{O}_1^H(^3P_0) = \frac{1}{3}\,\chi^\dagger(-\tfrac{i}{2}\overleftrightarrow{\mathbf{D}}\cdot\boldsymbol{\sigma})\psi\left(a_H^\dagger a_H\right)\psi^\dagger(-\tfrac{i}{2}\overleftrightarrow{\mathbf{D}}\cdot\boldsymbol{\sigma})\chi, \quad (1.10)$$

$$\mathcal{O}_1^H(^3P_1) = \frac{1}{2}\,\chi^\dagger(-\tfrac{i}{2}\overleftrightarrow{\mathbf{D}}\times\boldsymbol{\sigma})^i\psi\left(a_H^\dagger a_H\right)\psi^\dagger(-\tfrac{i}{2}\overleftrightarrow{\mathbf{D}}\times\boldsymbol{\sigma})^i\chi, \quad (1.11)$$

$$\mathcal{O}_1^H(^3P_2) = \chi^\dagger(-\tfrac{i}{2}\overleftrightarrow{D}^{(i}\sigma^{j)})\psi\left(a_H^\dagger a_H\right)\psi^\dagger(-\tfrac{i}{2}\overleftrightarrow{D}^{(i}\sigma^{j)})\chi, \quad (1.12)$$

$$\mathcal{P}_1^H(^1S_0) = \frac{1}{2}\left[\chi^\dagger\psi\left(a_H^\dagger a_H\right)\psi^\dagger(-\tfrac{i}{2}\overleftrightarrow{\mathbf{D}})^2\chi + \text{h.c.}\right], \quad (1.13)$$

$$\mathcal{P}_1^H(^3S_1) = \frac{1}{2}\left[\chi^\dagger\sigma^i\psi\left(a_H^\dagger a_H\right)\psi^\dagger\sigma^i(-\tfrac{i}{2}\overleftrightarrow{\mathbf{D}})^2\chi + \text{h.c.}\right], \quad (1.14)$$

as well as the corresponding color-octet operators for the P-waves. The symbol $\overleftrightarrow{D}$ refers to the difference between the covariant derivative acting on the spinor to the right and on the spinor to the left. The notation $T^{(i,j)}$ refers to the symmetric traceless components of a rank-2 tensor. The rate of production of a quarkonium H is expressed in terms of the vacuum expectation value of the operators $\mathcal{O}_n^H$. The term $\psi^\dagger\kappa_n\chi|0\rangle$ (resp. $\langle 0|\chi^\dagger\kappa_n\psi$) corresponds to the creation (resp. the annihilation) of a heavy-quark pair in a state n at the same space-time point. The projector $a_H^\dagger a_H$ takes into account the evolution into a physical state that includes a quarkonium H.

In the expression of the cross section, each long-distance matrix element $\langle 0|\mathcal{O}_n(\Lambda)|0\rangle$ appears with a certain strength $\hat{\sigma}_n(\Lambda)$, also called the short-distance coefficient, which encodes the high-energy modes above the factorization scale Λ, that are associated with the creation of the heavy-quark pair in a definite state n. As a result, the cross section is given by

$$\sigma(H) = \sum_n \hat{\sigma}_n(\Lambda)\langle 0|\mathcal{O}_n^H(\Lambda)|0\rangle. \quad (1.15)$$

This formula can be read as a double expansion in α_s and in v. On the one hand, the short-distance coefficients are computed order by order in the QCD coupling constant α_s. They are process-dependent, i.e., they do depend on the collisions at work. On the other hand, the long-distance matrix elements encode the non-perturbative effects that lead to the formation of the quarkonium bound state and are universal. The scaling rules that apply to these matrix elements define the expansion in v. A summary of the power counting rules of the most relevant long-distance matrix elements can be found in [22]. In Eq. (1.15), the scale dependence in the short-distance coefficients is cancelled by the scale dependence in the long-distance matrix elements order by order in α_s and v.

The coefficients $\hat{\sigma}_n$ appearing in Eq. (1.15) can be obtained by requiring that the production rate of a perturbative heavy-quark pair computed within NRQCD matches the corresponding production rate computed within QCD. In other words, the short-distance coefficients are fixed by the matching condition

$$\sigma(Q\bar{Q})|_{\text{pert. QCD}} = \sum_n \hat{\sigma}_n \langle 0|\mathcal{O}_n^{Q\bar{Q}}(\Lambda)|0\rangle|_{\text{pert. NRQCD}}. \tag{1.16}$$

Beyond leading order in α_s, ultraviolet and infrared divergences arise in the calculation of the right-hand side of Eq. (1.16). UV divergences are removed by renormalization of the strong coupling constant and the heavy-quark mass. IR divergences cancel between the real and the virtual amplitude whenever the KLN theorem [23, 24] applies. The remaining IR poles are expected to factorize over the Born and to be reabsorbed by either the parton distribution functions, or the fragmentation functions, or NRQCD long-distance matrix elements. It is the goal of the factorization theorems to prove that this procedure can be applied at any order in α_s. Recent works have clarified the validity of the NRQCD factorization, as we will review in Section 1.5.

1.2 Short-distance coefficients

As explained in the previous section, the short-distance coefficients in a given process are obtained by matching the computation of the cross section for the production of a perturbative heavy-quark pair in the QCD and NRQCD frameworks. For the computation of a given coefficient, one can use covariant projectors [6] to select the relevant state of the heavy-quark pair. For calculations beyond the leading order in α_s, the projection method has been generalized in d dimension of space-time in order to handle the UV and IR pôles through dimensional regularization [25]. A potential drawback of the projection method is that a new computation is required for each short-distance coefficient. Instead, in the threshold expansion method [26, 12], one expands the full QCD amplitude in the heavy-quark relative momentum around $\boldsymbol{p} = 0$. Therefore, at each order in v, all of the relevant short-distance coefficients appear in this expansion.

In the next chapters we will use the projection method, as its numerical implementation is easier. In this section, we rederive the expression of the projectors, starting from the expansion of a generic heavy-quark production amplitude. We only consider tree-level processes and assume $d = 4$ dimensions of space-time. Thus the formalism below can be applied for computing the short-distance coefficients at the Born level. Beyond the leading order in α_s, the following approach can be followed for the computation of the real part of the short-distance coefficients. These quantities are infrared divergent in a four-dimensional space-time. However, infrared singularities factorize over lower-order contributions. In particular at next-to-leading order in

α_s, each infrared pôle factorizes over the Born amplitude in a universal way. One can take advantage of this property to build from the Born amplitude subtracted terms (e.g. dipoles [27]) that match the IR poles in the real amplitude. For the calculation of cross sections at NLO accuracy, such procedures do not require the knowledge of the real amplitude in generic d dimensions of space-time, and one can therefore consider $d = 4$ for the computation of the real part. This procedure has recently been generalized at NNLO (see for example [28]).

Let us denote u, p_1, r (resp. v, p_2, s) the Dirac spinor, the momentum and the spin index associated to the heavy quark (resp. heavy anti-quark). Color indices associated to the heavy quarks are understood. Let us consider the amplitude for a generic production process of a perturbative heavy-quark pair

$$\bar{u}(p_1, r) M v(p_2, s). \tag{1.17}$$

In Eq. (1.17), M is a matrix carrying Dirac and color indices. We first analyze the Dirac structure. Using the Dirac representation for the γ matrices, we can express the spinors $u(p_1, r)$ and $v(p_2, s)$ in the following way:

$$u(p_1, r) = \frac{\not{p}_1 + m}{\sqrt{E_1 + m}} u_0(r), \quad v(p_2, s) = \frac{-\not{p}_2 + m}{\sqrt{E_2 + m}} v_0(s). \tag{1.18}$$

In this expression, u_0 and v_0 are the rest-frame spinors. From now on, we consider the Dirac representation, which is more convenient for the non-relativistic limit. In this representation, the explicit representation of the spinors u_0 and v_0 reads

$$u_0(r) = \begin{pmatrix} \xi_r \\ 0 \end{pmatrix}, \quad v_0(s) = \begin{pmatrix} 0 \\ \eta_s \end{pmatrix} \tag{1.19}$$

where ξ_r and η_s are two components spinors with understood color indices. The spin indices r, s will also be dropped hereafter. We consider the following complete basis in the Dirac space:

$$\{\gamma^A\} = \{\mathbb{1}, \gamma^5, \gamma^\mu, \gamma^5\gamma^\mu, \gamma^0\gamma^i, \gamma^0\gamma^i\gamma^5\} \tag{1.20}$$

Any matrix N in the Dirac space can be decomposed in terms of the matrices γ^A:

$$N = \sum_A c_A \gamma^A, \quad c_A = \mathrm{Tr}(N\gamma^A)/\mathrm{Tr}(\gamma^A\gamma^A) \tag{1.21}$$

Applying this decomposition to the matrix $N = (\not{p}_1 + m)M(-\not{p}_2 + m)$, we find that the production amplitude reads

$$\begin{aligned}\frac{1}{4\sqrt{(E_1+m)(E_2+m)}}\Big\{ & \bar{u}_0 v_0 \mathrm{Tr}\left[(\not{p}_1 + m)\, M\, (-\not{p}_2 + m)\right] \\ & + \bar{u}_0 \gamma^5 v_0 \mathrm{Tr}\left[(\not{p}_1 + m)\, M\, (-\not{p}_2 + m)\, \gamma^5\right] \\ & + \bar{u}_0 \gamma^0 v_0 \mathrm{Tr}\left[(\not{p}_1 + m)\, M\, (-\not{p}_2 + m)\, \gamma^0\right] \\ & - \bar{u}_0 \gamma^0\gamma^5 v_0 \mathrm{Tr}\left[(\not{p}_1 + m)\, M\, (-\not{p}_2 + m)\, \gamma^0\gamma^5\right] \\ & - \bar{u}_0 \gamma^i v_0 \mathrm{Tr}\left[(\not{p}_1 + m)\, M\, (-\not{p}_2 + m)\, \gamma^i\right] \\ & + \bar{u}_0 \gamma^0\gamma^i v_0 \mathrm{Tr}\left[(\not{p}_1 + m)\, M\, (-\not{p}_2 + m)\, \gamma^0\gamma^i\right] \\ & + \bar{u}_0 \gamma^0\gamma^i\gamma^5 v_0 \mathrm{Tr}\left[(\not{p}_1 + m)\, M\, (-\not{p}_2 + m)\, \gamma^0\gamma^i\gamma^5\right] \Big\}.\end{aligned} \tag{1.22}$$

In the Dirac representation, the only non-vanishing terms in the above expression come from the sandwiched matrices with off-diagonal blocks

$$\bar{u}_0 \gamma^5 v_0 = \bar{u}_0 \gamma^0\gamma^5 v_0 = \xi^\dagger \eta \tag{1.23}$$

$$\bar{u}_0 \gamma^i v_0 = \bar{u}_0 \gamma^0\gamma^i v_0 = \xi^\dagger \sigma^i \eta \tag{1.24}$$

i.e. the production amplitude is decomposed into a spin 0, Eq. (1.23) and a spin 1, Eq. (1.24), contributions. This decomposition is obviously not Lorentz invariant. In the matching procedure aimed at identifying the short-distance cross sections, we work in the center-of-mass of the heavy-quark pair. In this frame, the relative momentum is noted $\boldsymbol{p}$, and $E = \sqrt{m^2 + \boldsymbol{p}^2}$ refers to the energy of either of the heavy quarks. Introducing the projector

$$P_- = \frac{\gamma^0 - \mathbb{1}}{2} \tag{1.25}$$

and

$$\Pi_0 = \frac{1}{\sqrt{2}(E+m)}(-\not{p}_2 + m)P_-\gamma^5(\not{p}_1 + m), \tag{1.26}$$

$$\Pi_1 = -\frac{1}{\sqrt{2}(E+m)}(-\not{p}_2 + m)P_-\gamma^i(\not{p}_1 + m), \tag{1.27}$$

we see that Eq. (1.22) reduces to

$$\frac{1}{\sqrt{2}}\xi^\dagger\eta \mathrm{Tr}\left[M\Pi_0\right] + \frac{1}{\sqrt{2}}\xi^\dagger\sigma^i\eta \mathrm{Tr}\left[M\Pi_1^i\right]. \tag{1.28}$$

The expressions defining the spin projectors in Eqs. (1.26, 1.27) should be evaluated in the $Q\bar{Q}$ center-of-mass frame. Such expressions do not have a covariant transformation law under Lorentz boosts, due to the projector $P_- \propto \gamma^0 - \mathbb{1}$, which leads to a

mixed transformation for Π_0 (pseudo-scalar + pseudo-vector) and for Π_1 (vector+rank 2 tensor). It is interesting to express these projectors in a covariant form, in such a way that the decomposition in Eq. (1.22) specific to the heavy-quark-pair center-of-mass frame can be easily obtained from the expression of the momenta in any frame. To this aim, we first redefine E and P_-

$$E = \frac{1}{2}\sqrt{(p_1+p_2)^2}, \quad P_- = \frac{(\not{p}_1+\not{p}_2)+2E}{4E}, \tag{1.29}$$

With this redefinition, the first trace in Eq. (1.28) is invariant under the Lorentz group, whereas the second trace transforms as a vector. We next decompose the color structure of the production amplitude. As the heavy-quark pair can be either in a singlet or in an octet state, we readily obtain

$$M = \frac{1}{N_c} Tr(M)\mathbb{1} + 2\sum_a Tr(T^a M)T^a \tag{1.30}$$

where the trace is now over the color indices of the heavy-quark line. For the sake of clarity, it is useful to introduce the color projectors

$$C^{[1]} = \frac{\mathbb{1}}{\sqrt{N_c}}, \quad C_a^{[8]} = \sqrt{2}T^a. \tag{1.31}$$

So far we have disentangled the spin singlet/triplet, color singlet/octet contributions in the production amplitude. We have not expanded yet the amplitude in powers of $\boldsymbol{v} = \boldsymbol{p}/E$. In particular, the spin projectors Π_0 and Π_1 defined in Eqs. (1.26,1.27) are accurate to all orders in v. Their expression is consistent with the form derived in [29].

We now proceed to square the amplitude. By color symmetry of the NRQCD operators, terms that mix a color-singlet state with a color-octet one vanish. However terms with different angular momentum states may interfere in the production rate. Indeed, states with different orbital momentum may have a non-zero overlap with a given physical state $|H+X\rangle$ in Eq. (1.15). When one computes the squared amplitude, the relative momentum in the amplitude $\boldsymbol{p}$ should be kept distinct from the relative momentum $\boldsymbol{p}'$ in the complex conjugated amplitude. We will assume $|\boldsymbol{p}| = |\boldsymbol{p}'|$, so that the energy of the heavy-quark pair is well defined. In a similar way, as heavy-quark spin symmetry is not an exact symmetry, terms belonging to different intrinsic spin representations may interfere. Keeping track of these interference terms, we find that

the squared amplitude reads

$$\frac{1}{2N_c}\eta'^{\dagger}\mathbb{1}_{\text{spin}}\otimes\mathbb{1}_{\text{col}}\xi'\xi^{\dagger}\mathbb{1}_{\text{spin}}\otimes\mathbb{1}_{\text{col}}\eta\text{Tr}\left[C^{[1]}M\Pi_0\right]^*_{\boldsymbol{p}'}\text{Tr}\left[C^{[1]}M\Pi_0\right]_{\boldsymbol{p}} \quad (1.32)$$

$$+\frac{1}{2N_c}\eta'^{\dagger}\sigma^i\otimes\mathbb{1}_{\text{col}}\xi'\xi^{\dagger}\sigma^j\otimes\mathbb{1}_{\text{col}}\eta\text{Tr}\left[C^{[1]}M\Pi_1^i\right]^*_{\boldsymbol{p}'}\text{Tr}\left[C^{[1]}M\Pi_1^j\right]_{\boldsymbol{p}} \quad (1.33)$$

$$+\frac{1}{2N_c}\eta'^{\dagger}\sigma^i\otimes\mathbb{1}_{\text{col}}\xi'\xi^{\dagger}\mathbb{1}_{\text{spin}}\otimes\mathbb{1}_{\text{col}}\eta\text{Tr}\left[C^{[1]}M\Pi_0\right]^*_{\boldsymbol{p}'}\text{Tr}\left[C^{[1]}M\Pi_1^i\right]_{\boldsymbol{p}} \quad (1.34)$$

$$+\frac{1}{2N_c}\eta'^{\dagger}\mathbb{1}_{\text{spin}}\otimes\mathbb{1}_{\text{col}}\xi'\xi^{\dagger}\sigma^i\otimes\mathbb{1}_{\text{col}}\eta\text{Tr}\left[C^{[1]}M\Pi_1^i\right]^*_{\boldsymbol{p}'}\text{Tr}\left[C^{[1]}M\Pi_0\right]_{\boldsymbol{p}} \quad (1.35)$$

$$+\eta'^{\dagger}\mathbb{1}_{\text{spin}}\otimes T^a\xi'\xi^{\dagger}\mathbb{1}_{\text{spin}}\otimes T^b\eta\text{Tr}\left[C_a^{[8]}M\Pi_0\right]^*_{\boldsymbol{p}'}\text{Tr}\left[C_b^{[8]}M\Pi_0\right]_{\boldsymbol{p}} \quad (1.36)$$

$$+\eta'^{\dagger}\sigma^i\otimes T^a\xi'\xi^{\dagger}\sigma^j\otimes T^b\eta\text{Tr}\left[C_a^{[8]}M\Pi_1^i\right]^*_{\boldsymbol{p}'}\text{Tr}\left[C_b^{[8]}M\Pi_1^j\right]_{\boldsymbol{p}} \quad (1.37)$$

$$+\eta'^{\dagger}\sigma^i\otimes T^a\xi'\xi^{\dagger}\mathbb{1}_{\text{spin}}\otimes T^b\eta\text{Tr}\left[C_a^{[8]}M\Pi_1^i\right]^*_{\boldsymbol{p}'}\text{Tr}\left[C_b^{[8]}M\Pi_0\right]_{\boldsymbol{p}} \quad (1.38)$$

$$+\eta'^{\dagger}\mathbb{1}_{\text{spin}}\otimes T^a\xi'\xi^{\dagger}\sigma^i\otimes T^b\eta\text{Tr}\left[C_a^{[8]}M\Pi_0\right]^*_{\boldsymbol{p}'}\text{Tr}\left[C_b^{[8]}M\Pi_1^i\right]_{\boldsymbol{p}}. \quad (1.39)$$

Gauge invariance of the NRQCD operators implies that the product of the two traces in Eqs. (1.36-1.39) is proportional to δ_{ab}:

$$\text{Tr}\left[C_a^{[8]}M\Pi\right]^*\text{Tr}\left[C_b^{[8]}M\Pi\right]=\frac{\delta_{ab}}{N_c^2-1}\text{Tr}\left[C_d^{[8]}M\Pi\right]^*\text{Tr}\left[C_d^{[8]}M\Pi\right], \quad (1.40)$$

where from now on, a sum over repeated indices is understood.

We now proceed to carry out the phase-space integration. We integrate over all unobserved quantities, except the relative momentum between the heavy quarks. The Lorentz invariant expression of the phase-space measure for N final particles

$$d\phi=\prod_{i=1}^{N}\frac{d^3P_i}{(2\pi)^3 2E_i} \quad (1.41)$$

is used consistently with the relativistic normalization adopted so far. Let us denote by $d\widetilde{\phi}$ the Lorentz-invariant phase-space measure for the $Q\bar{Q}$ state of total momentum P and for the other final particles. The density of states associated with the heavy-quark pair depends on the normalization of the external states. In evaluating the right-hand side of Eq. (1.16), it is convenient to choose a non-relativistic normalization for the heavy-quark state $|Q\bar{Q}(p)\rangle$. As a result, the appropriate phase-space factor to integrate the amplitude in Eqs. (1.32-1.39) reads

$$\frac{2(E_1+E_2)}{4E_1E_2}\times d\widetilde{\phi}. \quad (1.42)$$

where E_1 (E_2) is the energy of the heavy (anti-)quark. In the first factor of Eq. (1.42), the numerator compensates for the relativistic phase space in $d\widetilde{\phi}$, and the denominator compensates for the relativistic normalization of the spin projectors. We recall that the matching procedure aimed at determining the short distance coefficients is carried on in the center-of-mass frame of the heavy quarks. In this frame, the first factor in Eq. (1.42) reduces to $\frac{1}{E}$, with E introduced earlier. This factor is usually reabsorbed into the definition of the spin projectors. As it is universal, we prefer to keep it factorized. Its origin can be traced back in the different choices of normalization in QCD and NRQCD theories. The phase-space measure $d\widetilde{\phi}$ can be evaluated in any frame, as it is Lorentz invariant.

We also expand the amplitude in $\boldsymbol{p}$. We first consider the production of S-wave states, as they are leading in $v = \frac{|\boldsymbol{p}|}{E}$. At leading order, the relative momentum is merely set to zero, such that the integration of the traces in Eqs. (1.32,1.33) gives

$$\frac{1}{2N_c m}\int \widetilde{d\phi}\mathrm{Tr}\left[C^{[1]}M\Pi_0\right]^*\mathrm{Tr}\left[C^{[1]}M\Pi_0\right] \equiv \hat{\sigma}({}^1S_0^{[1]}) \tag{1.43}$$

$$\frac{1}{2N_c m}\int \widetilde{d\phi}\mathrm{Tr}\left[C^{[1]}M\Pi_1^i\right]^*\mathrm{Tr}\left[C^{[1]}M\Pi_1^j\right] \equiv \hat{\sigma}^{ij}({}^3S_1^{[1]}) \tag{1.44}$$

$$\frac{1}{(N_c^2-1)m}\int \widetilde{d\phi}\mathrm{Tr}\left[C_a^{[8]}M\Pi_0\right]^*\mathrm{Tr}\left[C_a^{[8]}M\Pi_0\right] \equiv \hat{\sigma}({}^1S_0^{[8]}) \tag{1.45}$$

$$\frac{1}{(N_c^2-1)m}\int \widetilde{d\phi}\mathrm{Tr}\left[C_a^{[8]}M\Pi_1^i\right]^*\mathrm{Tr}\left[C_a^{[8]}M\Pi_1^j\right] \equiv \hat{\sigma}^{ij}({}^3S_1^{[8]}). \tag{1.46}$$

At this order in v, invariance of the NRQCD operators under rotation implies that the crossed terms in Eqs. (1.34,1.35, 1.38,1.39) vanish. So the squared amplitude reduces to

$$\hat{\sigma}\left({}^1S_0^{[1]}\right)\eta'^\dagger \mathbb{1}_{\text{spin}}\otimes\mathbb{1}_{\text{col}}\xi'\xi^\dagger\mathbb{1}_{\text{spin}}\otimes\mathbb{1}_{\text{col}}\eta \tag{1.47}$$

$$+\quad \hat{\sigma}^{ij}\left({}^3S_1^{[1]}\right)\eta'^\dagger\sigma^i\otimes\mathbb{1}_{\text{col}}\xi'\xi^\dagger\sigma^j\otimes\mathbb{1}_{\text{col}}\eta \tag{1.48}$$

$$+\quad \hat{\sigma}\left({}^1S_0^{[1]}\right)\eta'^\dagger\mathbb{1}_{\text{spin}}\otimes T^a\xi'\xi^\dagger\mathbb{1}_{\text{spin}}\otimes T^a\eta \tag{1.49}$$

$$+\quad \hat{\sigma}^{ij}\left({}^3S_1^{[1]}\right)\eta'^\dagger\sigma^i\otimes T^a\xi'\xi^\dagger\sigma^j\otimes T^a\eta. \tag{1.50}$$

The four-spinors products in Eqs. (1.47-1.50) can be identified with the matrix elements of the NRQCD operators in Eqs. (1.5-1.8) after the replacement $a_H^\dagger a_H \to a^\dagger_{QQ'(p')}a_{QQ(p)}$, up to spin correlation effects. In the computation of unpolarized cross section for a physical quarkonium H, the spin indices in the long-distance matrix element decouple from those in the short-distance coefficient which allows us to reduce the number of long-distance matrix elements. By rotational invariance we have

$$\langle\chi^\dagger\sigma^i\psi\left(a_H^\dagger a_H\right)\psi^\dagger\sigma^j\chi\rangle = \frac{\delta^{ij}}{3}\langle\chi^\dagger\sigma^l\psi\left(a_H^\dagger a_H\right)\psi^\dagger\sigma^l\chi\rangle, \tag{1.51}$$

and similarly for the corresponding color-octet matrix elements. We therefore introduce the scalar short-distance coefficients $\hat{\sigma}\left({}^3S_1^{[1,8]}\right) = \frac{1}{3}\hat{\sigma}^{ii}\left({}^3S_1^{[1,8]}\right)$.

The perturbative P-wave states appear at higher order in v. The terms in Eqs (1.32,1.36) expanded at order $\mathcal{O}(p,p')$ give the leading contribution for the spin-singlet P-wave state. Introducing the coefficients

$$\hat{\sigma}^{mn}({}^1P_1^{[1]}) = \frac{1}{2N_c m} \times \int \widetilde{d\phi} \left\{ \nabla_{p'}^m \left(\mathrm{Tr}\left[C^{[1]} M \Pi_0 \right]^* \right) \right\} \Big|_{p'=0} \left\{ \nabla_p^n \left(\mathrm{Tr}\left[C^{[1]} M \Pi_0 \right] \right) \right\} \Big|_{p=0} \quad (1.52)$$

$$\hat{\sigma}^{mn}({}^1P_1^{[8]}) = \frac{1}{(N_c^2-1) m} \times \int \widetilde{d\phi} \left\{ \nabla_{p'}^m \left(\mathrm{Tr}\left[C_a^{[8]} M \Pi_0 \right]^* \right) \right\} \Big|_{p'=0} \left\{ \nabla_p^n \left(\mathrm{Tr}\left[C_a^{[8]} M \Pi_0 \right] \right) \right\} \Big|_{p=0} \quad (1.53)$$

we get the following contributions

$$\hat{\sigma}^{mn}\left({}^1P_1^{[1]}\right) \eta'^{\dagger} p^m \mathbb{1}_{\text{spin}} \otimes \mathbb{1}_{\text{col}} \xi' \xi^{\dagger} p^n \mathbb{1}_{\text{spin}} \otimes \mathbb{1}_{\text{col}} \eta \quad (1.54)$$

$$+\hat{\sigma}^{mn}\left({}^1P_1^{[8]}\right) \eta'^{\dagger} p^m \mathbb{1}_{\text{spin}} \otimes T^a \xi' \xi^{\dagger} p^n \mathbb{1}_{\text{spin}} \otimes T^a \eta. \quad (1.55)$$

The four-spinors products in Eq. (1.54) can be identified with the matrix elements of the NRQCD operators in Eq. (1.9) after the replacement $a_H^{\dagger} a_H \to a_{QQ'(p')}^{\dagger} a_{QQ(p)}$, up to spin correlation effects. Again, in the case of unpolarized cross section, rotational invariance can be used to decouple the vector indices so that only one scalar matrix element is left. The resulting scalar short-distance coefficient is defined by $\hat{\sigma}\left({}^1P_1^{[1]}\right) = \frac{1}{3}\hat{\sigma}^{mm}\left({}^1P_1^{[1]}\right)$. In Eq. 1.55, the identification of the octet ${}^1P_1$ matrix element works in the same way, and leads to the definition of the scalar short-distance coefficient $\hat{\sigma}\left({}^1P_1^{[8]}\right) = \frac{1}{3}\hat{\sigma}^{mm}\left({}^1P_1^{[8]}\right)$.

For the P-wave spin-triplet piece at order $\mathcal{O}(p,p')$, the short-distance coefficient is a rank-4 tensor. Considering the color-singlet part, we define

$$\hat{\sigma}^{im,jn}({}^3P_1^{[1]}) = \frac{1}{2N_c m} \times \int \widetilde{d\phi} \left\{ \nabla_p^m \left(\mathrm{Tr}\left[C^{[1]} M \Pi_1^i \right]^* \right) \right\} \Big|_{p=0} \left\{ \nabla_{p'}^n \left(\mathrm{Tr}\left[C^{[1]} M \Pi_1^j \right] \right) \right\} \Big|_{p'=0} \quad (1.56)$$

In the case of unpolarized cross section, this tensor is contracted with a operator that is a rank-4 rotation tensor. The vacuum expectation of this operator is invariant under

rotations. As the tensor representation $(\otimes\underline{1})^4$ contains three times the representation $\underline{0}$, there are three independent reduced scalar matrix elements, corresponding to the states with definite total angular momentum $J = 0, 1$ or 2. The corresponding short-distance coefficients can be identified by projecting Eq. (1.56) onto the tensors $\frac{1}{3}\delta^{mi}\delta^{nj}$, $\frac{1}{2}(\delta^{mn}\delta^{ij} - \delta^{mj}\delta^{ni})$ and $\frac{1}{2}(\delta^{mn}\delta^{ij} + \delta^{mj}\delta^{ni}) - \frac{1}{3}\delta^{mi}\delta^{nj}$. We readily find

$$\hat{\sigma}\left({}^3P_0^{[1]}\right) = \frac{1}{3}\hat{\sigma}^{aa,bb} \tag{1.57}$$

$$\hat{\sigma}\left({}^3P_1^{[1]}\right) = \frac{1}{3}\left[\frac{1}{2}\left(\hat{\sigma}^{ab,ab} - \hat{\sigma}^{ab,ba}\right)\right] \tag{1.58}$$

$$\hat{\sigma}\left({}^3P_2^{[1]}\right) = \frac{1}{5}\left[\frac{1}{2}\left(\hat{\sigma}^{ab,ab} + \hat{\sigma}^{ab,ba}\right) - \frac{1}{3}\hat{\sigma}^{aa,bb}\right] \tag{1.59}$$

The corresponding color-octet short-distance cross section $\hat{\sigma}\left({}^3P_0^{[8]}\right)$, $\hat{\sigma}\left({}^3P_1^{[8]}\right)$ and $\hat{\sigma}\left({}^3P_2^{[8]}\right)$ can be obtained in a similar way.

To summarize the results of this section, we have derived the expression of the unpolarized short-distance coefficients for the S- and P-wave states. In our conventions, the short-distance coefficients include a factor $1/(2N_c)$ in the case of color-singlet transition, and a factor $1/(N_c^2 - 1)$ in the case of color-octet transitions. We have also included a spin average factor $1/(2J + 1)$ in the definition of the short-distance coefficients, as well as a factor $1/E$ (expanded at the correct order in v) for the normalization of the quarkonium state. As a final remark, we note that we can obtain the short-distance coefficients of the long-distance matrix elements in Eqs. (1.13, 1.14), which give a correction term of order v^2 to the color-singlet production of S-wave states. These coefficients come from collecting the $\boldsymbol{p}^2$ and $\boldsymbol{p}'^2$ terms Eqs. (1.32, 1.33), as well as the $\boldsymbol{p}^2$ arising from the expansion of the phase space measure in Eq. (1.42).

1.3 Long-distance matrix elements

The long-distance matrix elements that appear in Eq. (1.15) encode the non-perturbative evolution of a heavy-quark pair into a physical quarkonium state. At present, they cannot be computed from first principles, but they are expected to be process-independent, i.e., they do not depend on the details of the production of the perturbative heavy quarks. Based on this universality, their value at a certain scale can be extracted from experimental data relative to a given production process and then used to predict the cross section in another experiment. The evolution with the factorization scale can be predicted on the basis of a perturbative calculation. The NRQCD formalism is predictive, provided that the relative velocity is sufficiently small. In such a case, the

series defined in Eq. (1.15) can be truncated at a given accuracy in v. Only a restricted number of long-distance matrix elements contribute to the production rate. In order to increase the predictive power, approximate relations among these matrix elements can be derived, as we review in this section.

Vacuum-saturation approximation

This approximation [30] allows us to relate production matrix elements to those involved in the decay in the case of color-singlet transitions. Such a relation appears when we assume that the sum in Eq. (1.4) is dominated by the quarkonium state H plus the NRQCD vacuum. The decay and production matrix elements are then identical, up to a factor $2J+1$ that is the number of polarization degrees of freedom of the quarkonium H. The vacuum-saturation approximation is accurate up to corrections of relative order v^4.

Color-singlet matrix elements for the decay are related in turn to the $Q\bar{Q}$ wave functions at the origin, or their derivatives. Potential models can then be used to evaluate these wave functions [31]. Within this approximation, there are no free parameters left for the production of quarkonium via color-singlet transitions.

Heavy-quark spin symmetry

Heavy-quark spin symmetry is only an approximate symmetry of the NRQCD Lagrangian. Indeed, at order v^2 relative to the leading term, the Lagrangian includes the term $\psi^\dagger \boldsymbol{B}.\boldsymbol{\sigma}\psi - \chi^\dagger \boldsymbol{B}.\boldsymbol{\sigma}\chi$, which breaks the spin symmetry. If we neglect corrections of relative order v^2, then the spin of the perturbative heavy-quark pair matches the spin of the quarkonium state. This leads to approximate relations for the polarized long-distance matrix elements. In particular, for the production of a spin-triplet S-wave quarkonium state of polarization λ, we have [26]

$$\langle \chi^\dagger \sigma^i a^\dagger_{H(\lambda)} a_{H(\lambda)} \psi^\dagger \sigma^j \chi \rangle = \frac{1}{3} \epsilon^i_\lambda \epsilon^{*j}_\lambda \langle \mathcal{O}^H_1(^3S_1) \rangle, \tag{1.60}$$

$$\langle \chi^\dagger \sigma^i T^a a^\dagger_{H(\lambda)} a_{H(\lambda)} \psi^\dagger \sigma^j T^a \chi \rangle = \frac{1}{3} \epsilon^i_\lambda \epsilon^{*j}_\lambda \langle \mathcal{O}^H_8(^3S_1) \rangle, \tag{1.61}$$

$$\langle \chi^\dagger \sigma^i (-\frac{i}{2} \overleftrightarrow{D}^m) T^a a^\dagger_{H(\lambda)} a_{H(\lambda)} \psi^\dagger \sigma^j (-\frac{i}{2} \overleftrightarrow{D}^n) T^a \chi \rangle = \epsilon^i_\lambda \epsilon^{*j}_\lambda \delta^{mn} \langle \mathcal{O}^H_8(^3P_0) \rangle. \tag{1.62}$$

1.4 Quarkonium production at high energy

In the previous sections, we have seen how the formalism of NRQCD succeeds in separating momentum scales of order $m_Q v$ or smaller from momentum scales of order m_Q or higher. On the one hand, the order of magnitude of the long-distance matrix elements is controlled by the mean relative velocity v inside the quarkonium state. On the other hand, the relative sizes of the short-distance cross sections are controlled by the strong-coupling constant α_s. The amplitude related to the high-energy process (or equivalently the short-distance process) can be computed within the perturbation theory, as the strong interaction is perturbative above the energy scale m_Q. As v is also a small parameter, quarkonium production amplitudes can be expanded up to a certain order in α_s and in v.

At large energy, a new range of perturbative scales becomes relevant. The perturbative expansion is not entirely under the control of the strong-coupling constant. Although additional parton emissions are suppressed by powers of α_s, the phase-space for such emissions increases rapidly. This feature manifests itself in the cross section by the presence of large logarithms , that can spoil the perturbation expansion. In such cases, there is a need to rearrange the perturbative expansion to boost the convergence of the cross section, which can be achieved by resumming the leading logarithm behavior of the cross section.

1.4.1 Fragmentation processes at large transverse momentum

We first analyze the case of quarkonium production at large transverse momentum $P_T \gg m_Q$. In this limit, a new hierarchy of energy scales appears in the short-distance process, and the leading contribution is not guaranteed to be given by the lowest order term in the strong coupling constant. If we assume that all infrared sensitivity has been factorized into non-perturbative parameters, the short-distance process is characterized by momentum flow ranging from m_Q to P_T. Exchange of particles with virtualities of order P_T suppresses the probability amplitude, as it corresponds to the scattering of particles in a very small volume $\frac{1}{P_T^3}$. For some mechanisms though, intermediate particles are kinematically allowed to travel over distances of order $(\frac{1}{m_Q})$, which lead to an enhancement of $\frac{P_T}{m_Q}$ compared to the previous case. Therefore, if the energy scales m_Q and P_T are well-separated, the kinematics of the mechanism under work is a determinant factor to estimate the size of its contribution to the probability amplitude, together with the strong coupling constant.

Owing to this feature, channels opening at higher order in the strong-coupling constant can dominate the cross section the limit $\frac{m_Q}{P_T} \to 0$, if they receive a kinematic enhancement $\left(\frac{P_T}{m_Q}\right)^n$ compared to the Born-level mechanism. In such a situation, reliable phenomenological studies must take into account NLO or even NNLO contributions in order to include these mechanisms in which the parton-level production takes place in a volume of order $\frac{1}{m_Q^3}$. At this stage, beside the technical difficulty of performing such higher order calculations in the frame work of NRQCD, there is another problem that can spoil the *entire* convergence of the α_s expansion. Considering the amplitude $|M|^2$ at order n, the contribution at order $n+1$ from radiation of an extra gluon from the heavy-quark line gives a correction term $\sim \alpha_s \log\left(\frac{m_Q}{P_T}\right) \times |M|^2$, which is not small compare to $|M^2|$ if $P_T \gg m_Q$. This issue points out the need to disentangle the two energy scales m_Q and P_T in the short-distance coefficients in order to avoid large logarithms of the ratio of these scales. The realization of this new factorization within the fragmentation picture also proves to simplify greatly the calculation of quarkonium amplitudes, as we will see in the next section.

Historically, the importance of the fragmentation contributions in quarkonium production was first realized in the case of S-wave quarkonium states in the framework of the color-singlet model [32], and the implications for the phenomenology in electron-positron collisions and at hadron colliders were investigated soon thereafter. Fragmentation processes originate from the production of intermediate partons that subsequently split into a heavy-quark pair (and possibly other partons). At large transverse momentum, the dominant contribution is characterized by a virtuality for the intermediate parton of the order of m_Q, which is much lower than the energy in the center-of-mass frame. Gluon-fragmentation channels into S-wave charmonium states open up at order α_s^4 and α_s^5 for the ${}^1S_0^{[1]}$ and the ${}^3S_1^{[1]}$ states, respectively, whereas charm-fragmentation channels open up at order α_s^4 for both the spin 0 and the spin 1 quarkonium states. Although the fragmentation mechanisms appear at higher order in α_s, they are enhanced by a factor $(\frac{P_T}{m_Q})^n$ compared to the Born-level contribution, which therefore becomes subdominant at sufficiently large P_T.

In the limit $\frac{m_Q}{P_T} \to 0$, the fragmentation piece decouples from the production amplitude squared associated with the production of the intermediate parton, such that the cross section can be written as

$$d\sigma_{\mathcal{Q}} = \sum_i \int_0^1 dz d\hat{\sigma}_i(\frac{p}{z}) D_{i\to\mathcal{Q}}(z,\mu), \tag{1.63}$$

up to corrections of order $\frac{m_Q}{P_T}$. In Eq. (1.63), $d\hat{\sigma}_i(\frac{p}{z})$ corresponds to the production of a parton i with momentum $\frac{p}{z}$. All of the dependence on m_Q has been factorized in the fragmentation function $D_{i\to\mathcal{Q}}$, which describes the splitting of this parton into a quarkonium state of momentum p. As the intermediate parton is not observed, all

species must be taken into account. The fragmentation approximation, which disregards correction terms of order $\frac{m_Q}{P_T}$, greatly simplifies the calculation. As the fragmentation contributions to quarkonium production often occur at higher-order in α_s, a complete calculation is generally much more difficult to handle.

When we consider the radiative corrections to the fragmentation contributions, the intermediate parton can experience multiple splitting before giving rise to the heavy-quark pair. These splittings generates large logarithms of $\frac{m_Q}{P_T}$ in the amplitude. These logs a priori spoil the factorization of the different energy scales and compromise the perturbative expansion. As usual, this issue is solved by introducing a factorization scale μ

$$\log \frac{m_Q}{P_T} = \log \frac{\mu}{P_T} + \log \frac{m_Q}{\mu} \,. \tag{1.64}$$

The second term is reabsorbed in the fragmentation function, and the factorization scale μ is set to $\approx P_T$ in order to avoid large logs in the short-distance amplitude. In the framework of the color-singlet model, the fragmentation function $D_{i\to\mathcal{Q}}(z,\mu)$ can be computed perturbatively at the scale μ corresponding to the minimum invariant mass of the splitting parton (which is necessarily above $2m_Q$), and hence can be evolved to an arbitrary scale by using the evolution equation

$$\mu\frac{\partial}{\partial\mu}D_{i\to\mathcal{Q}}(z,\mu) = \sum_j \int_z^1 \frac{dy}{y} P_{i\to j}(\frac{z}{y},\mu) D_{j\to\mathcal{Q}}(y,\mu). \tag{1.65}$$

The fragmentation functions $D(c\to c\bar{c}\left[^{2S+1}L_J[1]\right)$ have been derived in [32] for S-wave states and in [33, 34] for P-wave states. Gluon fragmentation into quarkonia have been derived in [12, 35, 36] for S-wave sates and in [12, 37, 38] for P-wave states. This last process provides a very nice illustration of the NRQCD factorization procedure. At order α_s, only the color-octet transition $^3S_1^{[8]}$ contributes to the fragmentation function for P-wave state. The color-singlet short-distance coefficient at order α_s^2 develops an infrared pôle, that matches the infrared pôle in the radiative correction to the color-octet matrix element $\langle\mathcal{O}^{\chi_Q}(^3S_1^{[8]})\rangle$. As a result, the IR pôle in the perturbative amplitude can be reabsorbed into this NRQCD matrix element. The color-octet matrix element also develops a UV pôle that is removed by renormalization. It acquires a dependence in the factorization scale introduced by the regularization procedure. The color-singlet short distance coefficient also depends on the factorization scale in such a way that the overall scale dependence cancels in the fragmentation function.

1.4.2 k_t factorization at small x

Another large ratio of perturbative scales that appears in hadron collisions at high energy is $\hat{s}/s = x_1x_2$, where s refers to the center-of-mass energy squared of the

colliding hadrons, $\hat{s}$ to the center-of-mass energy squared of the colliding partons, and x_1, x_2 are the Bjorken fractions. At very small x, the evolution of the parton distribution function proceeds over a large region in rapidity, and effects of finite transverse momenta of the partons cannot be ignored. In this region, the cross section can be expressed as the convolution of an off-shell k_t dependent partonic cross section and a k_t-unintegrated parton density function $\mathcal{F}(z, k_t^2)$. This unintegrated gluon density is described by the BFKL evolution equation. We refer to Refs [39, 40] for a nice review of the k_t factorization approach.

In the case of heavy-quark production in hadronic collisions, the leading-order off-shell matrix element for the $gg \to Q\bar{Q}$ process estimates the impact of the on-shell NNLO process $gg \to ggQ\bar{Q}$. In this respect, the k_t factorization approach can be seen as a prescription to obtain the leading behavior of the α_s^2-suppressed cross section computed in the collinear factorization frame work, in the high energy limit $\hat{s}/s \to 0$. This procedure also applies for quarkonium production, which has been intensively studied in the framework of the k_t factorization [41, 42, 43, 44, 45, 46, 47]. A parallelism can be made with the fragmentation approximation, which extracts the leading behavior of the cross section in the limit $\frac{m_Q}{P_T} \to 0$.

1.5 Proof of the NRQCD factorization

As we have seen in the previous section, the formalism of NRQCD allows to factorize the non-perturbative effects inherent to the quarkonium states into a finite number of parameters, expressed as matrix elements of 4-fermion operators. The uncancelled infrared pôles that arise beyond the leading order in α_s must be reabsorbed into these NRQCD long-distance matrix elements. A well known example of application is the production of a P-wave quarkonium state from the fragmentation of a gluon, as we mentioned in Section 1.4.1.

Whether such a procedure can be applied at all order in α_s and in v is not obvious. In particular, it is not clear that all the uncanceled pôles in the computation of the short-distance coefficients can always be matched by the NRQCD matrix elements. The investigation of this issue is of capital importance, as it is the fundamental ground for the use of perturbative QCD in the computation of heavy quarkonium cross sections. Several efforts have recently been made to analyze the validity of the NRQCD factorization approach at higher order in α_s. We briefly review some of these new results.

Nayak et al. [48, 49] have investigated the production of quarkonium states at large P_T from gluon fragmentation. At NNLO accuracy in α_s, they found uncanceled pôles that do not appear in the perturbative calculation of the long-distance matrix elements.

They showed that, if the color-octet matrix elements are modified by the introduction of Wilson lines that make them gauge invariant, the factorization is restored at NNLO. This restoration makes use of the fact that the IR pôle does not depend on the direction of the Wilson line. It is therefore unclear whether the factorization holds at higher order in α_S.

In more recent papers [50, 51], Nayak *et al* have analyzed associated heavy quarkonium production, i.e. the production of a quarkonium state plus a heavy-quark pair of the same flavor. They showed that the standard NRQCD factorization procedure does not apply in phase-space regions in which one of the passive quarks is co-moving with the active heavy-quark pair with almost zero relative momentum. In such a configuration, color exchange between the active and passive heavy quarks leads to an infrared pôle that cannot be matched by any of the standard NRQCD long distance matrix elements.

Recently Bodwin *et al.* [52] have outlined the proof of the factorization theorems for exclusive two-body charmonium production in B-meson decay and in e^+e^- annihilation, both of these processes being particularly relevant from the phenomenological point of view. Considering all orders in the strong coupling constant, they find that factorized expressions hold up to corrections of order m_c/m_b in B-meson decay, and up to corrections of order m_c^2/s in e^+e^- annihilation, where m_c, m_b and $\sqrt{s}$ are the charm-quark mass, the bottom quark mass and the e^+e^- center-of-mass energy, respectively. For the specific process of $e^+e^- \to J/\psi + \chi_{c0}$, the NLO cross section has been computed explicitly in [53]. The factorization has been found to hold exactly at this order, provided that the relative velocity inside the S-wave quarkonium state is set to zero.

Chapter 2

Improving our predictions

The main subject of this thesis is the study of the phenomenological consequences of NRQCD. In order to assess whether the factorization principles summarized in the previous Section are experimentally validated, predictions and measurements have to be confronted with each other, through observables that allow us to identify the mechanism(s) at work in the production of quarkonium states. This procedure entails the computation of the short-distance coefficients perturbatively in the strong-coupling constant α_s. Here we will consider the Feynman-diagram techniques to compute the amplitude at a given order in α_s. Because of the number of diagrams, the calculation of scattering amplitudes cannot be achieved by hand when the number of external particles is large. Also in this case, the handling of the phase-space integration may not be straightforward. In this chapter, we describe how we have automated these steps through numerical algorithms for quarkonium production.

2.1 NRQCD amplitudes at tree-level

As we have seen in the first chapter, quarkonium squared amplitudes in the framework of NRQCD are obtained by means of an expansion in powers of the relative velocity v between the heavy quarks. At leading order in v, the intermediate $Q\bar{Q}$ state can be specified by the spectroscopic notation

$$n = {}^{2S+1}L_J^{[c]}\,, \tag{2.1}$$

where S identifies the spin state of the heavy-quark pair, L the orbital momentum state, J the total angular momentum state, and $c = 1, 8$ the color state.

To evaluate the short-distance coefficients we use the general algorithms for Feynman-diagram based computations that are available in MadGraph [54]. MadGraph can provide partonic helicity amplitudes for any process in the Standard Model, and for many processes beyond the Standard Model, at the tree level. In the case of quarkonium, we start from the helicity amplitude information for open quark-antiquark production and then apply several projection operators that select the specific quantum state numbers, ${}^{2S+1}L_J^{[c]}$. The projectors are universal and depend only on the quantum numbers to be selected and not on the specific process requested. In fact, only the color projection has to be performed within MadGraph itself since it changes the way the amplitudes are calculated (and in particular selects which diagrams contribute) while spin projections and velocity expansions are performed at runtime. Our method entails that any squared matrix amplitude $|\mathcal{M}(ij \to Q\bar{Q}({}^{2S+1}L_J^{[c]}) + X)|^2$ can be generated in any of the models available in MadGraph. Limitations are typical to Feynman-diagram based matrix element generators and are connected to the factorial growth in the number of diagrams.

Let us stress a few important points. First, our implementation also allows the calculation of the relativistic corrections for S-wave state production. Second, the employed projectors are general enough to handle the case in which the quark and the anti-quark are of different flavor, and therefore have a different mass. In our approach, the full polarization information is kept, so that the interface with a quarkonium decay algorithm with all spin correlation effects included is possible. It is also direct to extend our procedure so that it can also handle the production of non-relativistic exotic states, such as those introduced in the literature [55, 56]. Generalization to double heavy-quarkonium is straightforward.

2.1.1 Projection method and its implementation

In this Section, we discuss how to combine the open-quark helicity amplitudes generated by MadGraph in order to select a specific configuration ${}^{2S+1}L_J^{[c]}$ for the heavy-quark pair. We restrict ourselves to S- and P-wave states, although the algorithm can be extended to higher orbital-angular-momentum configurations. Our method can be seen as a generalization and automation of that proposed in Refs. [57, 58].

First we address the computation of the color factors. In MadGraph, the color structure of the parton-level amplitude is obtained by organizing the amplitude into gauge invariant subsets, corresponding to different color flows in the large-N_C limit [59]. The total amplitude is then expressed as a sum over the color flows

$$\mathcal{M} = \sum_m f_m(a, b, \dots) A_m \,, \tag{2.2}$$

where the f_m's are color factors (orthogonal in the large N_c limit) that depend on color indices $a, b, \ldots$ carried by gluons and quarks, and the A_m's are gauge invariant quantities, the so-called partial amplitudes. These amplitudes are computed in MadGraph with the help of HELAS subroutines [60]. The color factors are evaluated at the level of the squared amplitude, each color index being contracted:

$$|\mathcal{M}|^2 = (A_1^*, A_2^*, \ldots) \begin{pmatrix} f_1^* f_1 & f_1^* f_2 & \cdots \\ f_2^* f_1 & f_2^* f_2 & \cdots \\ \vdots & \vdots & \end{pmatrix} \begin{pmatrix} A_1 \\ A_2 \\ \vdots \end{pmatrix} . \tag{2.3}$$

The decomposition of the partonic amplitude into partial gauge-invariant amplitudes, as well as the evaluation of the matrix of color factors, are computed automatically for any process at tree-level.

In order to compute the color structure related to the process $ij \to Q\bar{Q}(^{2S+1}L_J^{[c]}) + X$, the quark and anti-quark are required to be in a given color state $[c]$. Given that $3 \otimes \bar{3} = 1 \oplus 8$ the pair can be either in a singlet or an octet state that can be obtained by using the projectors [25]

$$\mathcal{C}_1 = \frac{\delta_{ij}}{\sqrt{N_C}}, \quad \mathcal{C}_8 = \sqrt{2}(T^a)_{ij}, \tag{2.4}$$

where i and j are the color indices of the heavy quarks. These projectors have been implemented in MadGraph. The color structure for the quarkonium production amplitude is then computed by using the same technique as for the open quark production.

Next we consider the projection of the amplitude onto a definite total spin state of the heavy-quark pair. The spin projectors were first derived in Ref. [6, 7, 8], and we employ the normalization of Ref. [25]. Since the code is also designed for the production of heavy quarkonia of mixed flavors, we distinguish the mass of the quark (m_1) from that of the anti-quark (m_2). p_1 (p_2), the momentum of the heavy quark (anti-quark) can be expressed in terms of the total momentum P and the relative momentum p:

$$p_1 = \frac{E_1}{E_1 + E_2} P + p, \quad p_2 = \frac{E_2}{E_1 + E_2} P - p\,, \tag{2.5}$$

where E_1 (E_2) stands for the energy of the quark (anti-quark) in the quarkonium rest frame. The partial helicity amplitudes can be combined to yield a specific spin state for the heavy-quark pair:

$$\mathcal{M}(ij \to Q\bar{Q}(S, \lambda) + X) = \sum_{\lambda_1, \lambda_2} N(\lambda | \lambda_1, \lambda_2) \mathcal{M}(ij \to Q(\lambda_1)\bar{Q}(\lambda_2) + X)\,, \tag{2.6}$$

where the Clebsch-Gordan coefficients $N(\lambda|\lambda_1,\lambda_2)$ can be written in terms of the heavy-quark spinors [1],

$$N(\lambda|\lambda_1,\lambda_2) = \frac{1}{\sqrt{8m_1m_2}}\bar{v}(p_2,\lambda_2)\Gamma_S u(p_1,\lambda_1)\ , \tag{2.7}$$

with $\Gamma_{S=1} = \epsilon_\mu^\lambda\gamma^\mu$ for a spin-one $Q\bar{Q}$ state (ϵ_μ^λ being the polarization vector), and $\Gamma_{S=0} = \gamma_5$ for a spin-zero $Q\bar{Q}$ state. Note that this expression is accurate only at leading order in the relative momentum p. The helicity amplitudes $\mathcal{M}(ij \to Q(\lambda_1)\bar{Q}(\lambda_2)+X)$ are computed by MadGraph in a specific Dirac representation employed in the HELAS subroutines [60]. These subroutines can also be invoked for the evaluation of the current in the rhs of Eq. (2.7). The spin projection formula in Eq. (2.6) can then be easily incorporated in a generic numerical algorithm.

We then consider the projection onto a specific orbital-angular-momentum state. For S-wave state production at leading order in v, one can simply set $p=0$ in the short-distance amplitude. For P-wave state, the leading order contribution in v is given by the derivative of the amplitude with respect to the relative momentum. We approach this derivative numerically by examining the quotient

$$\frac{\mathcal{M}(\Delta p^i) - \mathcal{M}(0)}{\Delta p^i} \tag{2.8}$$

in the quarkonium rest frame in the limit $\Delta p^i \to 0$.

Eventually, for spin-one P-wave states, the spin index is combined with the orbital-angular-momentum index in order to select a given angular momentum state, $J=0,1$ or 2.

2.1.2 Polarized amplitudes

Contributions to the squared amplitude from different spin states are disentangled in our procedure. By default, the spin quantization axis $\hat{s}$ is the direction of the quarkonium state in the partonic center-of-mass frame, but any other choice can easily be implemented. In the quarkonium rest frame, the polarization vectors ϵ_a's are defined by

$$\boldsymbol{T}.\hat{s}\epsilon_a = a\epsilon_a, \quad \text{for } a=-1,0,1. \tag{2.9}$$

where $\boldsymbol{T}$ is the spin 1 representation of the $SO(3)$ generators. The definition of the polarization vectors in Eq. (2.9) is extended to any frame by Lorentz transformation.

[1] We use the normalization $\bar{u}(p_i,\lambda_i)u(p_i,\lambda_i) = 2m_i = -\bar{v}(p_i,\lambda_i)v(p_i,\lambda_i)$.

In the case of ${}^3S_1$ and ${}^1P_1$ intermediate states, helicity amplitudes are directly obtained by contracting the polarization vector in the helicity basis with either the index of the spin projector or the orbital-angular-momentum index of the amplitude (see Eqs. 2.6-2.8). In the case ${}^3P_J$ intermediate states, we apply the reduction $1 \otimes 1 = 0 \oplus 1 \oplus 2$ to separate the different helicity components. If we denote by $M^{\mu\nu}$ the rank-2 tensor amplitude, the reduction reads

$$\mathcal{A}({}^3P_0) = M_{\mu\nu}\frac{\epsilon_1^\mu\epsilon_{-1}^\nu+\epsilon_{-1}^\mu\epsilon_1^\nu-\epsilon_0^\mu\epsilon_0^\nu}{\sqrt{3}}, \tag{2.10}$$

$$\mathcal{A}({}^3P_1,\lambda=1) = M_{\mu\nu}\frac{\epsilon_1^\mu\epsilon_0^\nu-\epsilon_0^\mu\epsilon_1^\nu}{\sqrt{2}}, \tag{2.11}$$

$$\mathcal{A}({}^3P_1,\lambda=0) = M_{\mu\nu}\frac{\epsilon_1^\mu\epsilon_{-1}^\nu-\epsilon_{-1}^\mu\epsilon_1^\nu}{\sqrt{2}}, \tag{2.12}$$

$$\mathcal{A}({}^3P_1,\lambda=-1) = M_{\mu\nu}\frac{\epsilon_0^\mu\epsilon_{-1}^\nu-\epsilon_{-1}^\mu\epsilon_0^\nu}{\sqrt{2}}, \tag{2.13}$$

$$\mathcal{A}(\chi_{c2},\lambda=2) = M_{\mu\nu}\epsilon_1^\mu\epsilon_1^\nu, \tag{2.14}$$

$$\mathcal{A}({}^3P_2,\lambda=1) = M_{\mu\nu}\frac{\epsilon_1^\mu\epsilon_0^\nu+\epsilon_0^\mu\epsilon_1^\nu}{\sqrt{2}}, \tag{2.15}$$

$$\mathcal{A}({}^3P_2,\lambda=0) = M_{\mu\nu}\frac{\epsilon_1^\mu\epsilon_{-1}^\nu+\epsilon_{-1}^\mu\epsilon_1^\nu+2\epsilon_0^\mu\epsilon_0^\nu}{\sqrt{6}}, \tag{2.16}$$

$$\mathcal{A}({}^3P_2,\lambda=-1) = M_{\mu\nu}\frac{\epsilon_0^\mu\epsilon_{-1}^\nu+\epsilon_{-1}^\mu\epsilon_0^\nu}{\sqrt{2}}, \tag{2.17}$$

$$\mathcal{A}({}^3P_2,\lambda=-2) = M_{\mu\nu}\epsilon_{-1}^\mu\epsilon_{-1}^\nu. \tag{2.18}$$

In this way, desired polarization information is easily extracted: the spin-density matrix for a given choice of the spin quantization axis can be readily evaluated. It is than easy to interface the code with a routine for quarkonium decays that takes into account all spin correlation effects. In the case of electromagnetic decay of vector-like quarkonium states, the decay into leptons has been implemented in MadOnia (see Section 2.2).

An additional comment should be added for the production of vector-like quarkonium states via a color-octet P-wave transition:

$$Q\bar{Q}\left({}^3P_J^{[8]}\right) \to \mathcal{Q}(1^{--})\,. \tag{2.19}$$

Up to now, we have explained how to derive numerically the squared amplitude projected onto definite states of total angular momentum J, J_z of the intermediate pair. Although this will give the correct unpolarized cross section, this procedure will fail to predict the polarization of a physical quarkonium state produced via a ${}^3P_J^{[8]}$ pair [26, 61, 62]. Since heavy-quark symmetry is an approximate symmetry in the NRQCD Lagrangian, the intrinsic angular momentum of the intermediate heavy-quark pair is transferred to the physical quarkonium state, up to v^2 corrections. A correct way to account for the polarization in this case is to project the amplitude onto states

of definite orbital momentum L, L_z and intrinsic angular momentum S, S_z, to square the amplitude, and then to sum over orbital-angular momentum degrees of freedom:

$$\sigma(ij \to Q\bar{Q}(^3P_J^{[8]}) + X \to \mathcal{Q}(\boldsymbol{\epsilon}(\hat{n})) + X) = \sum_{\boldsymbol{L}.\hat{n}} \hat{\sigma}\left[ij \to Q\bar{Q}\left(\boldsymbol{L}.\hat{n}, \boldsymbol{\epsilon}(\hat{n})\right) + X\right] \langle {}^3P_0^{[8]} \rangle_{\mathcal{Q}} \tag{2.20}$$

This projection procedure has been implemented as an option in our code.

2.1.3 Relativistic corrections to S-wave state production

The relativistic corrections to S-wave-state cross sections arise when the relative momentum p between the heavy quarks is kept different from zero in the computation of the squared amplitude and in the phase-space parametrization.

The computation of such corrections requires the use of spin projectors accurate to all orders in p. As we have seen in the first chapter, and according to the result of Ref. [29], the Clebsch-Gordan coefficients can be written as

$$N(\lambda|\lambda_1, \lambda_2) = \frac{1}{\sqrt{2}(E+m)} \bar{v}(p_2, \lambda_2) \frac{\not{P} + 2E}{4E} \Gamma_S u(p_1, \lambda_1) \ , \tag{2.21}$$

where $E = \frac{\sqrt{P^2}}{2}$ (in this case we assume that the quark and the anti-quark are of the same flavor, $m_1 = m_2 = m$). The contribution to an S-wave configuration is selected by projecting the amplitude onto the spherical harmonic $Y_{l=0}^{m=0}$. This entails an average of the amplitude over the direction of the relative momentum which can be performed during the phase-space integration: the relative momentum appearing in the amplitude and in the complex conjugated amplitude are kept distinct and their directions determined on an event-by-event basis by the phase space generator. In addition, $\boldsymbol{p}^2$ corrections to the mass of the quarkonium state are accounted for in the phase-space parametrization. The output of the computation is the short-distance cross section $\hat{\sigma}(\boldsymbol{p}^2)$ for an input value of $|\boldsymbol{p}|$. The part of the algorithm connected with the phase space has not been automatized yet.

Once the short-distance cross section $\hat{\sigma}(\boldsymbol{p}^2)$ is at hand, it can be expanded to extract the v^2 correction, bypassing the tedious relativistic expansion of the amplitude and of the phase-space measure. As our algorithm does not explicitly perform the Taylor-expansion, it can be also used to resum the relativistic corrections arising from the wave function, as proposed in Refs. [63, 64].

2.1.4 Validation

Preliminary checks

In order to gain confidence in our implementation, we have performed several checks listed below.

- Gauge invariance has been systematically verified for all the processes considered by using longitudinal polarization for the external photons or gluons.
- Numerical cancellation among diagrams has been checked for amplitudes that vanish by symmetry considerations:

$$
\begin{aligned}
&A(^1S_0^{[1]} + (2k+1)\,\text{photons}) = 0,\\
&A(^3S_1^{[1]} + 2k\,\text{photons}) = 0,\\
&A(^3P_{0,2}^{[1]} + (2k+1)\,\text{photons}) = 0,\\
&A(^1P_1^{[1]} + 2k\,\text{photons}) = 0,\\
&A(^3P_1^{[1]} + 2k\,\text{photons}) = 0,
\end{aligned}
$$

  with $k = 1, 2, 3$. The first three equations result from the Furry's theorem, whereas the last two equations result from the Yang's theorem (a spin-one particle cannot decay into two photons).

- We have compared our numerical amplitudes against the analytic results point-by-point in phase space for ($i, j, k =$ quarks or gluons):

  1. $ij \to \mathcal{Q}k$ for all S- and P-wave states, both color-singlet and color-octet amplitudes, [8][65][66];
  2. $ij \to \mathcal{Q}V$, with $V = Z, W$ for the relevant S- and P-wave states, both color-singlet and color-octet amplitudes [67];
  3. $ij \to \mathcal{Q}\phi$, ϕ being a scalar or pseudo-scalar for the relevant S- and P-wave states, both color-singlet and color-octet amplitudes [68];

  The agreement for S-wave amplitudes is at the level of the machine precision, while for P-waves, which are obtained through a numerical derivative, it is typically at the 10^{-5} level.

(fb)	${}^1S_0^{[1]}$	${}^3S_1^{[1]}$	${}^1P_1^{[1]}$	${}^3P_0^{[1]}$	${}^3P_1^{[1]}$	${}^3P_2^{[1]}$
$e^+e^-@m_Z$	$1.69 \cdot 10^3$	$2.37 \cdot 10^3$	$1.78 \cdot 10^2$	$1.08 \cdot 10^2$	$2.23 \cdot 10^2$	$2.40 \cdot 10^2$
$\gamma\gamma$@LEP II	0.519	5.23	0.162	$2.69 \cdot 10^{-2}$	$5.80 \cdot 10^{-2}$	0.266
γp@HERA	$3.66 \cdot 10^2$	$1.76 \cdot 10^3$	85.4	21.7	51.7	$2.02 \cdot 10^2$
pp@LHC(gg)	$3.94 \cdot 10^7$	$9.83 \cdot 10^7$	$5.20 \cdot 10^6$	$1.82 \cdot 10^6$	$4.40 \cdot 10^6$	$1.05 \cdot 10^7$
pp@LHC$(q\bar{q})$	$1.37 \cdot 10^5$	$8.34 \cdot 10^5$	$2.95 \cdot 10^4$	$1.10 \cdot 10^4$	$2.69 \cdot 10^4$	$7.26 \cdot 10^4$
$p\bar{p}$@Tev II(gg)	$2.56 \cdot 10^6$	$6.30 \cdot 10^6$	$3.28 \cdot 10^5$	$1.24 \cdot 10^5$	$2.83 \cdot 10^5$	$6.62 \cdot 10^5$
$p\bar{p}$@Tev II$(q\bar{q})$	$2.64 \cdot 10^4$	$1.62 \cdot 10^5$	$5.70 \cdot 10^3$	$2.12 \cdot 10^3$	$5.21 \cdot 10^3$	$1.41 \cdot 10^4$

Table 2.1: Cross sections (femtobarn) for the color-singlet contributions to the inclusive production of B_c.

(fb)	${}^1S_0^{[8]}$	${}^3S_1^{[8]}$	${}^1P_1^{[8]}$	${}^3P_0^{[8]}$	${}^3P_1^{[8]}$	${}^3P_2^{[8]}$
$e^+e^-@m_Z$	1.59	2.22	0.167	0.102	0.209	0.225
$\gamma\gamma$@LEP II	$4.9 \cdot 10^{-4}$	$4.9 \cdot 10^{-3}$	$1.5 \cdot 10^{-4}$	$2.5 \cdot 10^{-5}$	$5.4 \cdot 10^{-5}$	$2.5 \cdot 10^{-4}$
γp@HERA	1.18	8.46	0.506	$7.64 \cdot 10^{-2}$	0.244	1.61
pp@LHC(gg)	$4.11 \cdot 10^5$	$1.79 \cdot 10^6$	$1.17 \cdot 10^5$	$1.38 \cdot 10^4$	$6.23 \cdot 10^4$	$2.29 \cdot 10^5$
pp@LHC(qq)	$1.03 \cdot 10^3$	$7.03 \cdot 10^3$	251	30.7	174	616
$p\bar{p}$@Tev II(gg)	$2.85 \cdot 10^4$	$1.26 \cdot 10^5$	$8.13 \cdot 10^3$	$9.80 \cdot 10^2$	$4.25 \cdot 10^3$	$1.57 \cdot 10^4$
$p\bar{p}$@Tev II(qq)	199	$1.37 \cdot 10^3$	48.6	5.95	33.7	120

Table 2.2: Cross sections (femtobarn) for the color-octet contributions to the inclusive production of B_c.

Example 1: B_c production at various colliders

B_c production has been extensively studied at various colliders, and the many available results provide us with a further testing ground for our code.

We present the results for inclusive cross sections at several colliders for all the $S-$ and $P-$wave states, both color-singlet and color-octet. Since our purpose is to provide reference numbers, we use a very simple set of input parameters common to all processes:

- $m_b = 4.9$ GeV, $m_c = 1.5$ GeV, $m_{B_c} = 6.4$ GeV,
- $\langle O\left({}^{2S+1}S_J^{[1]}\right)\rangle = (2J+1)\,0.736\,\text{GeV}^3$,
- $\langle O\left({}^{2S+1}P_J^{[1]}\right)\rangle = (2J+1)\,0.287\,\text{GeV}^5$,
- $\langle O^{[8]}\rangle = 0.01\langle O^{[1]}\rangle$,
- $\mu_{epa} = \mu_F = \mu_R = 12.8$ GeV ,
- $\alpha_S(\mu_R) = 0.189$,
- pdf set: cteq6l1,
- $\alpha_{EM} = \frac{1}{137}$.

Our results are summarized in Tables 2.1 and 2.2. For the processes $gg \to B_c b\bar{c}$ we compared with Refs. [69, 70], and found agreement for all intermediate states. For color-singlet S-wave-state production in γg interactions, our results agree with those of Ref. [71]. For color-singlet B_c photo-production, our code has reproduced the results of Refs. [72, 73]. Several of the results in the Tables are new and provided as reference for future projects.

Example 2: Relativistic corrections to $e^+e^- \to J/\psi\,\eta_c$

Double S-wave charmonium production at B factories has attracted attention, as the leading order NRQCD prediction for the cross section [74, 75] is far below the measurements [76, 77].

The v^2 correction to the leading-order (in α_S and v^2) cross section for $e^+e^- \to J/\psi\,\eta_c$ was computed analytically in [74] and offers the possibility to check the algorithm discussed in Section 2.1.3. We have reproduced this result using the package

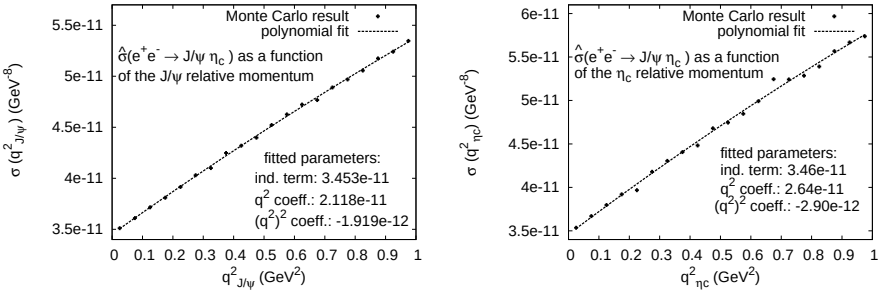

Figure 2.1: Short-distance cross section $\hat{\sigma}(e^+e^- \to J/\psi\eta_c)$, as a function of the relative momentum in the spin-one charm-quark pair (a), in the spin-zero charm quark pair (b).

FeynCalc [78]. The analytic forms for the derivatives of the short-distance cross sections with respect to the relative momentum in the J/ψ ($\boldsymbol{q}_{J/\psi}$) or in the η_c ($\boldsymbol{q}_{\eta_c}$) are [74, 75]

$$\frac{1}{\hat{\sigma}_0}\frac{d\hat{\sigma}}{d\boldsymbol{q}^2_{J/\psi}}\Big|_{\boldsymbol{q}^2_{J/\psi}=0} = \left(\frac{2}{m_c^2} - \frac{40}{3s} - 12\frac{s}{\lambda(s,(2m_c)^2,(2m_c)^2)}\right), \quad (2.22)$$

$$\frac{1}{\hat{\sigma}_0}\frac{d\hat{\sigma}}{d\boldsymbol{q}^2_{\eta_c}}\Big|_{\boldsymbol{q}^2_{\eta_c}=0} = \left(\frac{14}{6m_c^2} - \frac{40}{3s} - 12\frac{s}{\lambda(s,(2m_c)^2,(2m_c)^2)}\right), \quad (2.23)$$

where m_c is the mass of the charm quark, s is the squared center-of-mass energy, $\hat{\sigma}_0 = \hat{\sigma}(\boldsymbol{q} = \boldsymbol{0})$ is the leading-order short-distance cross section and $\lambda(x,y,z) = x^2+y^2+z^2-2xy-2xz-2yz$. In Eq. (2.22) (Eq. (2.23)), the two first terms come from the derivative of the squared amplitude with respect to $\boldsymbol{q}_{J/\psi}$ ($\boldsymbol{q}_{\eta_c}$), whereas the last term comes from the expansion of the phase space measure. There is no factor associated with the normalization of the wave function, as it has been factorized out of the short-distance cross section. Using $m_c = 1.5$ GeV and $\sqrt{s} = 10.6$ GeV, one finds

$$\frac{1}{\hat{\sigma}_0}\frac{d\hat{\sigma}}{d\boldsymbol{q}^2_{J/\psi}}\Big|_{\boldsymbol{q}^2_{J/\psi}=0} = 0.613\ \text{GeV}^{-2}, \qquad \frac{1}{\hat{\sigma}_0}\frac{d\hat{\sigma}}{d\boldsymbol{q}^2_{\eta_c}}\Big|_{\boldsymbol{q}^2_{\eta_c}=0} = 0.761\ \text{GeV}^{-2}. \quad (2.24)$$

Our procedure is as follows. We first set $\boldsymbol{q}_{\eta_c} = 0$ and compute the short-distance cross section as a function of $\boldsymbol{q}_{J/\psi}$. We then fit the result with a polynomial in $\boldsymbol{q}^2_{J/\psi}$

$$\hat{\sigma}(\boldsymbol{q}^2_{J/\psi}) = \alpha + \beta\boldsymbol{q}^2_{J/\psi} + \gamma(\boldsymbol{q}^2_{J/\psi})^2 + \ldots \quad (2.25)$$

where α, β, γ, ... are obtained by the fitting procedure. The value of α gives the leading-order cross section:

$$\sigma_0 = \alpha \times \langle \mathcal{O}^{J/\psi}({}^3S_1^{[1]})\rangle \langle \mathcal{O}^{\eta_c}({}^3S_1^{[1]})\rangle = 6.04 \text{ fb}. \tag{2.26}$$

The expression in Eq. (2.22) is approximated by the ratio of β and α, which is found

$$\frac{1}{\hat{\sigma}_0}\frac{d\hat{\sigma}}{d\boldsymbol{q}^2_{J/\psi}}\Big|_{\boldsymbol{q}^2_{J/\psi}=0} = \frac{\beta}{\alpha} = 0.613 \text{ GeV}^{-2}\,, \tag{2.27}$$

which is in agreement with the analytical result of Eq. (2.22). Moreover, we learn from the linearity of the plot in Fig. 2.1 (a) that, although the v^2 correction is large, higher-order corrections that are due to the relative motion of the quarks are well under control. Analogous steps can be repeated to find the correction associated to the relative momentum in the η_c (see Fig. 2.1 (b)), giving

$$\frac{1}{\hat{\sigma}_0}\frac{d\hat{\sigma}}{d\boldsymbol{q}^2_{\eta_c}}\Big|_{\boldsymbol{q}^2_{\eta_c}=0} = 0.762 \text{ GeV}^{-2}\,, \tag{2.28}$$

which is also in good agreement with the analytic value of Eq. (2.23).

2.2 Decay of vector-like quarkonia into leptons

The electromagnetic decay of $J^{PC} = 1^{--}$ quarkonium states is particularly important in phenomenological studies. Indeed, in hadron collisions at high energy a vector-like quarkonium state is observed through its decay into leptons and the polarization of the quarkonium can be determined by analyzing the angular distribution of the leptons. In this case, a general way to account correctly for the polarization information is to decay the vector-like quarkonium state into leptons at the matrix element level. In the Feynman gauge, this can be achieved by replacing the polarization vector of the quarkonium by the leptonic current

$$J^\mu_{\text{em}}(k_1, k_1, \lambda_1, \lambda_2) = \frac{\sqrt{3}}{8m\sqrt{\pi}}\bar{u}_{\ell^-}(k_1, \lambda_1)\gamma_\mu v_{\ell^+}(k_2, \lambda_2)\,. \tag{2.29}$$

The normalization is fixed by the condition

$$\sum_{\lambda_1,\lambda_2}\int d\Omega J^\mu_{\text{em}}(k_1, k_2, \lambda_1, \lambda_2)J^{\nu\dagger}_{\text{em}}(k_1, k_1, \lambda_1, \lambda_2) = -g^{\mu\nu} + \frac{P^\mu P^\nu}{m^2_{\mathcal{Q}}}, \tag{2.30}$$

where $d\Omega$ is the infinitesimal solid angle associated to the direction $\boldsymbol{k_1}$, $P = k_1 + k_2$ is the momentum of the quarkonium state, and $m_{\mathcal{Q}}$ is its mass.

The cross section then reads:

$$\sigma(J/\psi) = \frac{1}{2s}\int d\phi M_{\mu\nu}\sum_{\lambda_1,\lambda_2}\int d\Omega J^{\mu}_{\text{em}}(k_1,k_2,\lambda_1,\lambda_2)J^{\nu\dagger}_{\text{em}}(k_1,k_1,\lambda_1,\lambda_2). \quad (2.31)$$

This method has two main advantages. First it is directly connected to the experimental analysis. The acceptance of the detector may bias the measurement of the cross section and polarization. However, even when cuts are applied, the angular distribution of the leptons is the physical observable that can be used to compare theory and measurements. Second, it is Lorentz invariant and therefore does not impose an a priori choice for the frame where the polarization information is extracted. The decay of vector-like quarkonium states has been set-up as an option in our code.

2.2.1 Tracing back the polarization content

The connection between the quarkonium polarization and the angular distribution of the leptons originating from the quarkonium decay is made easier in the quarkonium rest frame, where a natural basis for the polarization vectors is given by the eigenstates of the spin-one representation of the rotation generator around the quantization axis [79]. If, in addition, we choose a frame in which the quantization axis is aligned in the $\hat{z}$ direction, the corresponding spin eigenstates read

$$\epsilon_{-1} = \frac{1}{\sqrt{2}}(0, e^{i\gamma}, ie^{i\gamma}, 0), \quad \epsilon_0 = (0,0,0,e^{i\alpha}), \quad \epsilon_1 = \frac{1}{\sqrt{2}}(0, -e^{i\beta}, ie^{i\beta}, 0), \quad (2.32)$$

where α, β and γ are arbitrary phases. The spin matrix associated with this choice of quantization axis is defined by

$$\rho_{\lambda,\lambda'} = M_{\mu\nu}\epsilon^{\mu}_{\lambda}\epsilon^{*\nu}_{\lambda'}. \quad (2.33)$$

This matrix is hermitian. From now on we set the arbitrary phases α, β and γ to zero. Then, from the expression of the polarization vector, we directly find that $\rho_{1,0} = -\rho_{-1,0}$. Moreover, if we assume that $M^{\mu\nu}$ is a symmetric tensor, we have $\rho_{1,1} = \rho_{-1,-1}$.

We can then use the completeness relation

$$\sum_{\lambda}\epsilon^{\mu}_{\lambda}\epsilon^{*\nu}_{\lambda} = -g^{\mu\nu} + \frac{P^{\mu}P^{\nu}}{m^2_{\mathcal{Q}}} \quad (2.34)$$

to identify the contribution of each spin matrix component in Eq. (2.31). Dropping the arguments of the electromagnetic current, we can express the cross section as

$$\sigma(\mathcal{Q}) = \frac{1}{2s}\int d\phi \sum_{\lambda,\lambda'}\rho_{\lambda,\lambda'}\int d\Omega \epsilon^{*\mu}_{\lambda}\epsilon^{\nu}_{\lambda'}J_{\text{em},\mu}J^{\dagger}_{\text{em},\nu}. \quad (2.35)$$

In the quarkonium rest frame, the lepton momenta read

$$\begin{aligned} k_1 &= m(1, \sin\theta\cos\phi, \sin\theta\sin\phi, \cos\theta), \\ k_2 &= m(1, -\sin\theta\cos\phi, -\sin\theta\sin\phi, -\cos\theta). \end{aligned} \tag{2.36}$$

After introducing the expression for $J_{\text{em},\mu} J^{\dagger}_{\text{em},\nu}$ in the quarkonium rest frame, we directly obtain the expression for the squared amplitude in terms of the spin matrix $\rho_{\lambda,\lambda'}$ and the angles θ and ϕ:

$$\begin{aligned} \sigma(\mathcal{Q} \to l^+ l^-) = \frac{1}{2s} \int d\phi \frac{3}{8\pi} \int d\Omega \Big\{ & \frac{1}{2}(\rho_{1,1} + \rho_{-1,-1})(1 + \cos^2\theta) \\ & + \rho_{0,0}(1 - \cos^2\theta) + \sin^2\theta Re\left(e^{-2i\phi}\rho_{1,-1}\right) \\ & + \frac{1}{\sqrt{2}} \sin 2\theta Re\left(e^{-i\phi}\rho_{1,0}\right) - \frac{1}{\sqrt{2}} \sin 2\theta Re\left(e^{i\phi}\rho_{-1,0}\right) \Big\}. \end{aligned} \tag{2.37}$$

The expression in Eq. (2.35) can be simplified in the case in which only the momenta of the muons and the initial particles are resolved. Indeed, the directions associated with these momenta are coplanar in the lab frame. The same plane is generated by the direction of the initial momenta in the quarkonium rest frame, where we sit from now on. Assuming that the quantization axis —denoted $\hat{z}$— is contained in this plane, we can choose the $\hat{y}$ axis to be orthogonal to this plane. With our choice of phases $\alpha = \beta = \gamma = 0$ in Eq. (2.32), any three-product of $\boldsymbol{\epsilon}_\lambda$ with one of the initial-particle momenta is real. As a result, the spin matrix components will be real, provided that we integrate over all degrees of freedom except the initial momenta and the momentum of the quarkonium state.

In this case, the angular distribution reads [79]

$$\frac{d\sigma}{d\Omega dy} \propto 1 + \lambda(y)\cos^2\theta + \mu(y)\sin 2\theta\cos\phi + \frac{\nu(y)}{2}\sin^2\theta\cos 2\phi$$

where y stands for a certain (set of) kinematics variable(s) associated with the quarkonium state. The parameters λ, μ, ν are related to the spin density matrix elements through:

$$\lambda = \frac{\rho_{1,1} - \rho_{0,0}}{\rho_{1,1} + \rho_{0,0}}, \quad \mu = \frac{\sqrt{2}\rho_{1,0}}{\rho_{1,1} + \rho_{0,0}}, \quad \nu = \frac{2\rho_{1,-1}}{\rho_{1,1} + \rho_{0,0}}. \tag{2.38}$$

Notice that the relation between the parameters μ, ν and the components of the spin density matrix depends on the phase convention for the polarization vectors. The λ parameter measures the relative contributions of the transverse and longitudinal components with respect to the quantization axis. Equivalently, it is connected to the polar

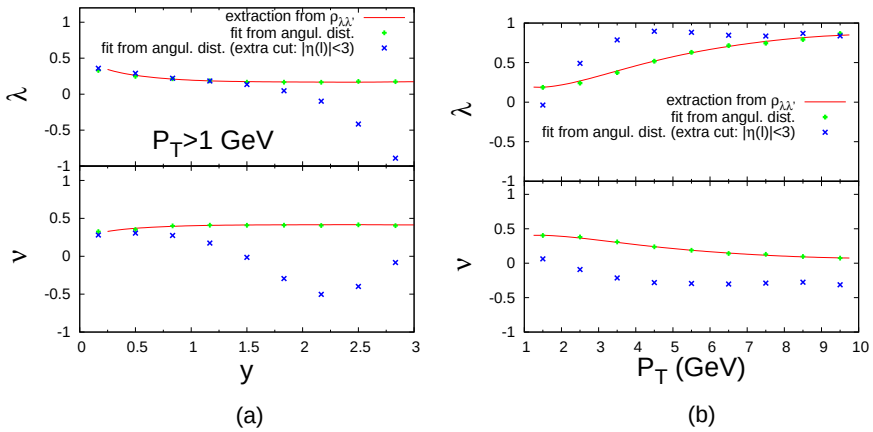

Figure 2.2: Helicity parameters λ and ν for the J/ψ produced from pp collisions at $\sqrt{s} = 10$ TeV at leading order in α_s and in v, as functions of the rapidity of the J/ψ (a) and the P_T of the J/ψ (b). The red line is based on the extraction of the helicity parameters from the spin density matrix. The green dots are the result of the fit of the angular distribution of the leptons. The blue crosses have also been obtained from fitting the lepton angular distribution, but with the extra cut $|\eta(l^{\pm})| < 3$ on the pseudo-rapidity of the leptons.

anisotropy in the distribution of the leptons in the quarkonium rest frame. After averaging over the polar angle, the azimuthal anisotropy is described by the ν parameter. The μ parameter disappears after integration over either θ of ϕ and is therefore difficult to extract experimentally.

2.2.2 Illustration

As we have mentioned in the previous section, cuts on leptons originating from the vector-like quarkonium state can affect the relation in Eq. (2.38) between the lepton angular distribution and the components of the spin density matrix. In order to illustrate this feature, let us consider the J/ψ production from proton-proton collisions at leading order in α_s and v. The corresponding parton-level process $gg \to gc\bar{c}\left({}^3S_1^{[1]}\right)$ includes six Feynman diagrams, which are obtained by attaching the three gluons to the charm quark line in the 3! possible ways.

The polarization of the J/ψ depends on the choice of the spin quantization axis. Here we choose the flight line of the J/ψ in the lab frame. We only discuss the prediction for the polarization parameters λ and ν relative to this choice of axis. According to the discussion in previous section, these parameters can either be obtained directly from the component of the spin density matrix, or from the angular distribution of the leptons originating from the J/ψ. As long as no cut is applied to the leptons, the two methods must give the same result, as is illustrated in Fig. 2.2 by the red curves and the green dots.

If we now reject all events with at least one lepton with a pseudo-rapidity larger than three, the values of the parameters λ and ν fitted from the angular distribution of the leptons change substantially. This is illustrated by the blue crosses in Fig. 2.2. In the region where the J/ψ has a low rapidity, the effect is only marginal. At higher rapidity, the production is still dominated by J/ψ events with a low transverse momentum. In order to pass the cut criteria, the leptons must be emitted preferentially in the direction transverse to the beam. This explains why the value of the λ parameter is decreased compared to the case where no cut is applied directly to the leptons. This effect is also observed in the distribution in Fig. 2.2 (b), but only at very low P_T. When the J/ψ has a larger transverse momentum, it is most of the time emitted in the direction transverse to the beam, and the leptons are preferentially emitted along the flight line of the J/ψ to pass the cut.

2.3 Validity of the fragmentation approximation

As we have seen in Section 1.4, it is easy to understand the importance of the fragmentation contributions at sufficiently high P_T. One illustration is provided by the color-singlet production of a J/ψ at the Tevatron. As analyzed in [80, 81], the charm-quark fragmentation channel dominates the α_s leading-order mechanism already above $P_T = 6$ GeV.

However, working within the fragmentation approximation, one has to keep in mind that it is only accurate up to correction scaling as $\frac{m_Q}{P_T}$. Although these terms vanish at very large P_T, their contribution in the phase space region accessible to experimentalists is a priori not known. We address this problem in the present Section, for some specific fragmentation processes.

One way to estimate the correction to the fragmentation approximation is to compare the P_T spectrum derived from Eq. (1.63) with the one obtained using the full matrix element associated with the fragmentation process. This matrix element includes naturally topologies that are not taken into account in the fragmentation approximation. In general such a comparison is not possible, because the corresponding full matrix

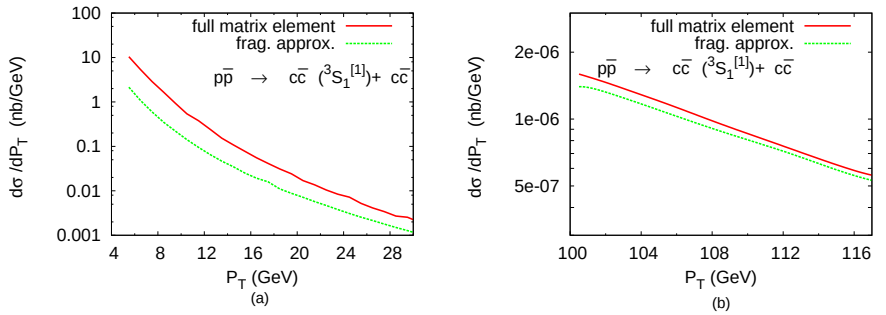

Figure 2.3: Comparison of the color-singlet fragmentation process $c \to c\bar{c}\left({}^3S_1^{[1]}\right) c$ with the full computation at small (a) and large P_T (b).

element is not known. For example, in the case of the color-singlet gluon fragmentation into η_c, this comparison would require the knowledge of the full order-α_s^4 matrix element, which is not available. For this reason, we focus in the following on the associated production

$$gg \to c\bar{c}c\bar{c}\left({}^{2S+1}L_J^{[n]}\right), \tag{2.39}$$

since in this case, the full matrix element requires only a tree-level computation which can be achieved automatically with MadOnia. In Eq. (2.39), $c\bar{c}\left({}^{2S+1}L_J^{[n]}\right)$ denotes a charm-quark pair forced into a specific configuration.

2.3.1 Color-singlet fragmentation from a charm quark

We start by considering the fragmentation process

$$gg \to \bar{c}\left(c \to c\bar{c}\left({}^{2S+1}L_J^{[1]}\right) c\right) \tag{2.40}$$

at the Tevatron, run II ($\sqrt{s} = 1.96$ TeV). We compare the P_T spectrum derived in the fragmentation approximation with the one obtained from a full matrix element computation, for which we use MadOnia. As our purpose is to quantify the validity of the fragmentation approximation we use fixed-order fragmentation functions at the initial scale $\mu = 3m_c$, i.e. we do not resum the emission of soft gluons. We fix the factorization and renormalization scales at $2m_c$ both in the fragmentation and in the full matrix element calculation.

We first consider the J/ψ, which is the most important case from the phenomenological point of view. Using $\langle \mathcal{O}^{J/\psi}\left({}^3S_1^{[1]}\right)\rangle = 1.16$ GeV, and the PDF set cteq6l1, we

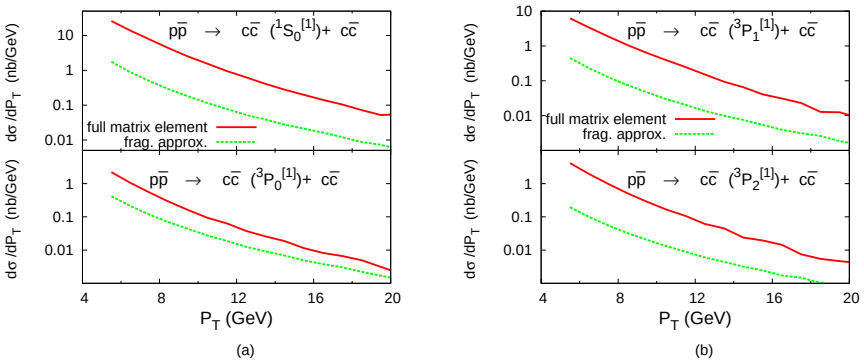

Figure 2.4: Charm-quark fragmentation approximation in the color-singlet approximation versus full matrix element computation for the η_c, χ_{c0} (a) and for the χ_{c1}, χ_{c2}.

obtain the comparison displayed in Fig. 2.3. At small P_T, the fragmentation approximation underestimates the yield by a large factor. In particular, it cannot be trusted in the P_T range $0 - 30$ GeV accessible to experiment at the Tevatron. As is illustrated by Fig. 2.3 (b), the gap between the two curves is reduced to a discrepancy of 10 percent at 100 GeV. It is interesting to note that for J/ψ production from e^+e^- annihilation, the fragmentation approximation is only 6% away from the full contribution at $\sqrt{s} = 50$ GeV [57].

One may try to gather an intuitive explanation for such glaring difference by considering the Feynman diagrams contributing to the two processes. In e^+e^- annihilation, there are only four diagrams at the leading order, all of which contribute to the fragmentation topologies. On the other hand, the dynamics underlying the ${}^3S_1$-quarkonia production at the Tevatron is much more involved. The number of Feynman diagrams is significantly larger and only a few of them give rise to fragmentation topologies. As a result, the fragmentation approximation starts to be relevant at a much higher regime in P_T. The same observation was made for the process $\gamma\gamma \to J/\psi c\bar{c}$ [82]. A similar situation exists also for the B_c^* hadroproduction, for which it was noticed that the fragmentation approximation was not reliable at the Tevatron [83, 84].

The performance of the charm-quark fragmentation approximation strongly depends on the quantum numbers of the bound state. For the χ_{c0}, the situation is a bit less dramatic than in the J/ψ case, as is illustrated in Fig. 2.4 (a) (lower panel). On

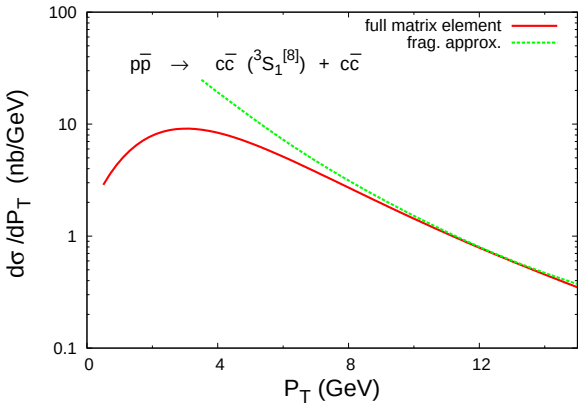

Figure 2.5: Double charm-quark pair production via a ${}^3S_1^{[8]}$ transition. The full matrix element result is compared with the fragmentation approximation.

the other hand, the fragmentation approximation is completely off in the case of the $\eta_c, \chi_{c1}, \chi_{c2}$ states, for which the comparison is also displayed in Fig. 2.4.

2.3.2 Color-octet fragmentation from a gluon

We now turn to the color-octet transition via a spin-triplet S-wave state. We consider the full matrix element for the process

$$gg \to c\bar{c}c\bar{c}({}^3S_1^{[8]}) \tag{2.41}$$

and compare its P_T spectrum with the result from the fragmentation approximation.

As we can see in Fig. 2.5 the fragmentation approximation in this case is very accurate already at $P_T \approx 8$ GeV. In the phase-space region above this threshold, topologies in which the projected $c\bar{c}$ pair is produced by one gluon of virtuality $2m_c$ largely dominate over the other topologies.

We close this Section by noting that a similar approach could be followed to investigate at which energy the k_t factorization formalism extract the leading behavior of the (N)NLO collinear cross section. Although this formalism is well motivated in the asymptotic high energy limit (or equivalently small x), it is not guaranteed that it captures the relevant features of the cross section at the Tevatron collider.

2.4 Monte Carlo techniques

In Section 2.1, we have described a general algorithm aimed at generating any quarkonium amplitudes at tree-level in the framework of NRQCD[2]. However, we have not discussed yet how to generate distributions of events that can be compared to measurements. We go back to this point is this Section.

In Section 2.4.1, we first detail the Monte Carlo integrator that has been interfaced with the amplitude generator of Section 2.1 to produce differential distributions or more generally any desired distributions of quarkonium events. In Section 2.4.2, we discuss the generation of unweighted events and the interface to a shower Monte-Carlo program.

2.4.1 Multi-channel phase-space integration

Among the various algorithms aimed at performing the numerical integration over the phase space, the Monte Carlo techniques are particularly suitable. First, their convergence is independent of the number of dimensions, which makes them more efficient than other methods when the number of external particles is large. Second, their random nature brings them closer to the experimental conditions of a real measurement, a point that will be clear in Section 2.4.2.

A Monte Carlo program generates random points in order to approximate the integral $I \equiv \int d\boldsymbol{z} f(\boldsymbol{z})$, ($\boldsymbol{z}$ is a d-vector in $[0,1]^d$) by the estimator

$$E = \frac{1}{N}\sum_{n=1}^{N} f(z_n). \tag{2.42}$$

This estimator converges to the true value of the integral I owing to the large number law. The standard deviation of the estimator σ_I is related to the variance of the function $\sigma^2(f)$ —$\sigma_I = \frac{\sigma(f)}{\sqrt{N}}$— which can be approximated by:

$$\sigma^2(f) \approx \frac{1}{N-1}\sum_{n=1}^{N}\left[f(\boldsymbol{z}_n) - E\right]^2 = \frac{1}{N-1}\sum_{n=1}^{N}(f(\boldsymbol{z}_n))^2 - \frac{N}{N-1}E^2. \tag{2.43}$$

Even with Monte-Carlo techniques, the integration of scattering amplitudes is a complicated problem, as the integrand varies over several order of magnitudes over the phase space. The propagators in the amplitude introduce a structure in peaks, controlled by the invariant masses of the exchanged particles. As a result the variance of the integrand is large and the convergence is slow.

[2] As discussed in Section 2.1 there are some limitations.

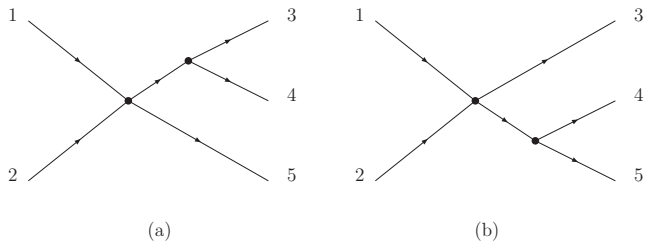

Figure 2.6: Illustration of two different channels in a single process: in (a), the invariant mass of particles 3 and 4 should be mapped onto a single phase-space variable; in (b), the invariant mass of particles 4 and 5 should be mapped onto a single phase-space variable.

One way to speed up the convergence is to use an adaptive Monte Carlo integrator [85], which learns about the function as it proceeds. The random points are then distributed according to a grid, which is adapted iteration by iteration to probe with higher-statistics regions in which the integrand is the largest in magnitude. Owing to storage and efficiency requirements, the grid is usually expressed as a separable function in d dimensions. In this case, the adaptive algorithm is only efficient if the variable that controls the size of each peak in the integrand is mapped onto a single variable of integration. In an adaptive Monte Carlo integration, the parametrization of the phase space is therefore crucial for the rapidity of convergence. After having identified the peak structure, one should map it onto a set of variables (or *channel*) in which all the peaks in the integrand are controlled by decoupled phase-space variables.

Let us review first how the phase-space integration is achieved in the case of open-quark production [86, 87]. For a given Feynman diagram, the peak structure is directly related to the kinematic invariants appearing in the propagators, such that the phase-space mapping is straightforward. The integration of the squared scattering amplitude requires in general more than one channel, since each Feynman diagram can a priori be mapped to a different channel (see illustration in Fig. 2.6). The question is then which weight should be given to a specific channel [88]. Among the possible solutions to this problem, we stick to the Single-Diagram-Enhanced multi-channel technique, (implemented in the integrator MadEvent [89]). In this method, the weight attached to a given channel is proportional to the squared amplitude of the corresponding diagram. More precisely, the squared amplitude is expressed in the following way

$$|M|^2 = \sum_j \frac{|A_j|^2}{\sum_i |A_i|^2} |M|^2, \tag{2.44}$$

where A_i is the amplitude corresponding to a single Feynman diagram. Each of the terms in the sum over j is then integrated using the channel j corresponding to the propagator structure of the diagram A_j.

We apply the same technique to integrate quarkonium amplitudes over the phase space. Each diagram $|A_j|$ is associated with a specific channel, and the corresponding weight is given by $\frac{|A_j|^2}{\sum_i |A_i|^2}$. As the two heavy quarks are bound into a single particle, we map a diagram with a propagator structure leading to m final particles to a channel with only $m-1$ particles. For sake of simplicity, this channel is chosen among the channels defined for the production of point-like $m-1$ particles [86]. This is a potential source of inefficiency, as not all the invariants associated with the propagators are mapped onto distinct phase-space variables.

Choosing the correct phase-space mapping for a given Feynman diagram is therefore not straightforward in the case of quarkonium production. In our automatic procedure, only the kinematic invariants associated with propagators which are not connected to one of the heavy-quark lines leading to the quarkonium state are guaranteed to be correctly mapped onto uncorrelated phase-space variables. For the other propagators, the associated invariants do not necessarily enter into the phase-space parametrization. In general, if the center-of-mass energy is of the order of the quarkonium mass, there is no problem of efficiency, as the range of variation for the virtuality of each exchanged particle is restricted. On the other hand, at large energies $E \gg m_{\mathcal{Q}}$, one has to be more careful about the channels used for the integration.

One example of difficulties that arise in the large-energy regime is given by the production of a charmonium state in association with a charm-quark pair. Two specific Feynman diagrams for this process are displayed in Fig. 2.7. In our algorithm, the first diagram is mapped onto the correct channel, where the invariant $(p_1+p_2)^2$ is mapped onto a single phase-space variable. If the center-of-mass energy E_{cm} is much larger than $2m_c$, then the dominant phase-space region is characterized by $(p_1+p_2)^2 \approx (3m_c)^2$, and is properly emphasized in by the adjustment of the grid. The second diagram in Fig. 2.7 also contributes to the fragmentation piece in a general gauge. Therefore, the contribution of this diagram at high energy is a peaked function of the invariant $(p_1+p_2)^2$, or equivalently $(\frac{p_1}{2}+p_2)^2$ i.e. the invariant mass squared of the exchanged gluon. The channel used for the integration of this diagram must be identified with the channel associated with the first diagram in Fig. 2.7.

Although the mapping between diagrams and channels is done automatically in MadOnia, one should keep in mind that this procedure might not be optimal for some cases. If problems of low efficiency are encountered, it is still very easy to rewrite channels that are more appropriate to the kinematics at work.

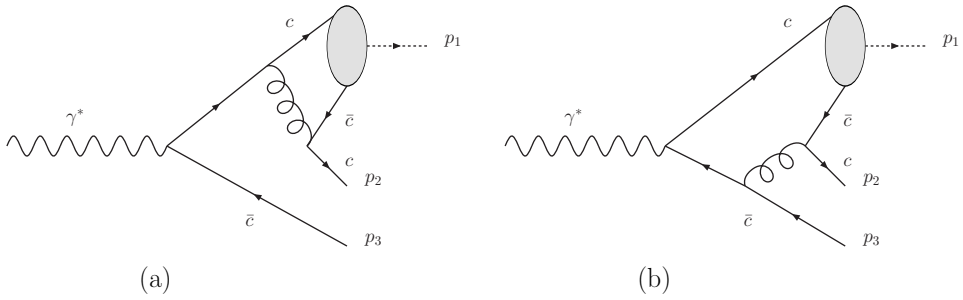

Figure 2.7: Two Feynman diagrams contributing to the fragmentation of a charm quark into a charmonium state.

2.4.2 Quarkonium event generator

As we recalled in the previous Section, a Monte Carlo integration consists of generating a series of random phase-space points, which we will also call *parton-level events*. To each event is attached a weight that is the product of the squared matrix element and the phase-space measure. The adjustment of the grid also leads to a non-uniform weight over the phase space, which can be accounted for in the phase-space measure. The total cross section is then expressed as the sum over the events of the weights associated with each event.

Within this procedure, it is extremely easy to get the distribution of the weights with respect to specific observables, and hence to derive differential cross sections. Indeed, one has merely to add up the weights according to a certain binning of the selected observables during the integration process. The resulting distributions give the cross sections differential in these observables. It is also clear that parton-level cuts can readily be implemented in a Monte Carlo integration: kinematic conditions are imposed on each generated event, and the weights associated with the points that failed the cuts are simply disregarded.

Despite the merits of a Monte Carlo integrator to facilitate the comparison between predictions and measurements, at this stage we are still far from a simulation of the experimental environment inherent in the reconstruction of quarkonium events. The weights that we have considered so far are attached to parton-level events. However, partons are not directly observed. As a result, cuts cannot be imposed on the kinematics of the partons themselves. Instead, partons in a given configuration are expected to undergo multiple QCD radiations (*showering*), before confinement turns them into hadrons (*hadronization*). The kinematics of these hadrons are then reconstructed in the detector within a certain accuracy.

The showering and hadronization process can be simulated by algorithms such as Pythia [16] or Herwig [17]. These programs need to know the color structure of the parton-level events, as partons will ultimately be turned into colorless states. For this reason, we keep track in MadOnia of the color-flow information, as well as all other parton quantum numbers. After the event has been evolved into a hadron-level configuration, it can be passed through another algorithm that simulates the reconstruction in the detector. Through the whole process, the weight initially attached to the parton-level event is not affected [3].

The interface with showering, hadronization and detector-simulation algorithms brings the prediction much closer to the experimental conditions inherent to a realistic measurement of a scattering process. The whole event generator can also serve as a tool to optimize selection criteria for a given process. However, such analyses are highly CPU-consuming, owing to the complexity of the detector. The time required for the processing of one event is large enough that we do not want to spend time on an event that has a small weight relative to the other events. For this reason, it is preferable to work with unweighted events, i.e. events that all have the same weight. In this case, distributions of the weights are just the same as distribution of events, (up to a normalization factor), which is also a source of simplification. The unweighting procedure makes use of the adjustment of the grid in order to the flatten the weight distribution as much as possible. The rest of the job is achieved by throwing away a certain number of events.

In our quarkonium studies, we make use of the unweighting procedure implemented in MadEvent [90]. The efficiency of production is in general less than for the case of open production, since the adjustment of the grid itself is less efficient (see the discussion of the previous Section).

2.5 Next-to-leading-order real amplitudes

Beside the tree-level predictions, we will also present new observables computed at NLO in the strong coupling constant α_s. In Section 3.3 we will discuss the NLO corrections to the J/ψ and Υ production at the Tevatron. In Section 3.4 we will present the new NLO prediction for the polarization of the J/ψ in photoproduction.

The NLO results for polarization observables presented in the next chapter make use of MadOnia for the computation of the polarized real amplitude in $d = 4$ dimensions of space time. Along with the virtual piece [91], these real amplitudes have been implemented in the Monte Carlo program MCFM [92]. This code makes use of the

[3] Events can of course be rejected if they do not pass experimental cuts during the reconstruction process

dipole-subtraction scheme developed in [93] in which the cross sections are expressed in the following way:

$$\sigma^{\rm NLO} = \int_{m+1} \left[d\sigma^R - d\sigma^A \right] + \int_m \left[d\sigma^V + \int_1 d\sigma^A \right]. \tag{2.45}$$

The subtracted dipoles $d\sigma^A$ in the first term on the rhs cancel all the IR singularities in the real amplitude $d\sigma^R$, such that the integration over the $m+1$-particle phase space is finite. The IR singularities present in the integrated dipole $\int_1 d\sigma^A$ are either canceled by the IR poles in the virtual amplitude $d\sigma^V$, or factorized into a universal non-perturbative function.

This scheme allows us to consider the computation of the real amplitude at NLO only in 4 dimensions of space time, which can be generated with MadOnia. However, it is important to check that the resulting numerical amplitude demonstrates a very good stability when either the soft or the collinear region is approached. Let us first consider the soft limit[4], i.e. when the momentum p_j of a final-state gluon becomes soft. This limit can be parametrized in terms of a four-vector q^μ and a scale parameter:

$$p_j^\mu = \lambda q^\mu, \quad \lambda \to 0. \tag{2.46}$$

In the soft limit, we obtain the following factorization formula:

$$|M_{m+1}(1,\dots,j,\dots,m+1)| \to -\frac{1}{\lambda^2} 4\pi\alpha_s M_m^*[J^\mu(q)]^\dagger [J_\mu(q)]) M_m, \tag{2.47}$$

where $J^\mu(q)$ is the eikonal current for the emission of the soft gluon q

$$J^\mu(q) = \sum_i \boldsymbol{T}_i \frac{p_i^\mu}{p_i.q} \tag{2.48}$$

and $\boldsymbol{T}_i$ is a operator that acts on the color space of the hard partons in the Born amplitude M_m. Owing to this color correlation, the squared amplitude $|M_{m+1}|^2$ factorizes over the Born amplitude squared only up to color rearrangements.

The collinear limit of momenta p_i and p_j can be parametrized in the following way:

$$\begin{aligned} &p_i^\mu = z p^\mu + k_\perp - \frac{k_\perp^2}{z}\frac{n^\mu}{2p.n}, \quad p_j^\mu = (1-z)p^\mu - k_\perp - \frac{k_\perp^2}{1-z}\frac{n^\mu}{2p.n}, \\ &2p_i.p_j = -\frac{k_\perp^2}{z(1-z)}, \quad k_\perp \to 0, \end{aligned} \tag{2.49}$$

where p^μ and n^μ are two light-like vectors satisfying $p.k_\perp = n.k_\perp = 0$, and $k_\perp$ is a space-like vector that controls the deviation from the collinear limit. In the collinear

[4] Our presentation for the soft and collinear limits follows closely ref. [93]

limit, the $m+1$ amplitude squared factorizes over the Born amplitude squared in the following way:

$$|M_{m+1}(1,\ldots,i,\ldots,j,\ldots,m+1)| \to \\ \frac{1}{p_i.p_j} 4\pi\alpha_s(\hat{P}_{(ij),i}(z,k_\perp))_{ss'}|M_m(1,\ldots,ij,\ldots,m+1))|_{s's}, \qquad (2.50)$$

where the m-parton matrix element on the rhs of Eq. (2.50) is obtained by replacing the partons i and j with a single parton ij carrying the quantum numbers of the pair $i+j$ in the collinear limit. $(\hat{P}_{(ij),i})_{ss'}$ denotes the Altarelli-Parisi splitting function in four dimension, which acts on the helicity space associated with the parton ij.

The Eqs (2.47) and (2.50) have been proven for any analytic real amplitudes. In our code, though, the limited numerical accuracy may spoil these relations when either the soft or the collinear limit is approached too closely. Hence, one has to check the numerical stability of the amplitudes. Here we stick to one specific example: we consider the J/ψ color-singlet process

$$g(p_1)g(p_2) \to g(p_3)g(p_4)J/\psi(p_5) \qquad (2.51)$$

and analyze the behavior of the squared amplitude in the collinear limit

$$p_3.p_4 \to 0. \qquad (2.52)$$

As is illustrated in Fig. 2.8, the amplitude shows a very good stability down to $p_3.p_4 = 10^{-8}$ GeV^2. The horizontal line is the product of the Altarelli-Parisi splitting function $\hat{P}_{gg}(z,k_\perp)$ with the Born-level matrix element $|M(g(p_1)g(p_2) \to g(p_3+p_4)J/\psi(p_5))|$, with appropriate contraction of the helicity of the final gluon.

2.6 Applications

2.6.1 Higgs decay into $\Upsilon + X$.

In this Section we illustrate through a very simple example how a multi-purpose matrix element code allows one to quickly assess the phenomenological relevance of new ideas.

A light Higgs of $m_H \lesssim 140$ GeV in the Standard Model as well as in extensions such as in SUSY or in generic two-Higgs-doublet models (2HDM), decays predominantly into $b\bar{b}$. If we assume a $2 \to 1$ production mechanism at hadron colliders, such as gg

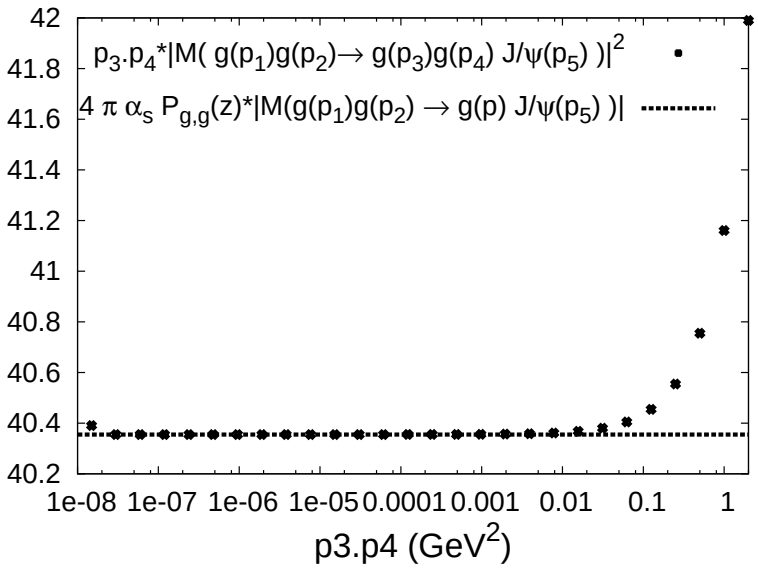

Figure 2.8: Illustration of the stability of the amplitude squared in the collinear limit $p_3.p_4 \to 0$.

or $b\bar{b}$ fusion, a two b-jet signature is obtained. Such events are extremely difficult to trigger on and to select from the enormous QCD two-jet background. In fact, in this mass range, the golden channel for discovery is $H \to \gamma\gamma$ which has a branching ratio of the order of only 10^{-3} in the SM but has a very clean signature: it can be triggered on and the invariant mass determination is very accurate, giving the possibility of reconstructing a small Breit-Wigner peak over a very large background. However, in some scenarios beyond the standard model, such as for example at large $\tan\beta$ in SUSY or in a generic 2HDM, the branching ratio to two photons is highly suppressed and other decay modes need to be considered.

The presence of an Υ in the final state could help both in the triggering (through the $\mu^+\mu^-$ pair) and in the invariant-mass reconstruction and give a viable discovery mode [32]. Let us consider two cases.

As the simplest decay mode, consider $H \to \Upsilon b\bar{b}$ [Fig 2.9 (left)]. This is analogous to $Z \to \Upsilon b\bar{b}$, which can also be described by the fragmentation-function approach. The full tree-level matrix element calculation gives:

$$\frac{\Gamma(H \to \Upsilon b\bar{b})}{\Gamma(H \to b\bar{b})} \quad = \quad 1.56 \cdot 10^{-5}\,, \tag{2.53}$$

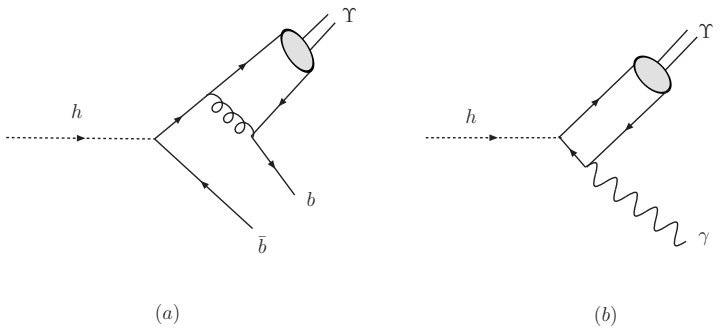

Figure 2.9: Higgs decays into Υ: in association with a $b\bar{b}$ pair (a) and with a photon (b).

where we have used $m_H = 120$ GeV, $\langle O_\Upsilon(^3S_1^{[1]})\rangle = 9.28$ GeV^3 and $\alpha_S = 0.118$.

Another, potentially cleaner mode, which would have excellent invariant mass resolution, is the decay $H \to \gamma\Upsilon$, Fig 2.9 (right) Note that the crossed decay $\Upsilon \to \gamma H$ has been considered before in the literature [94, 95, 96, 97] as a search mode for a light scalar or pseudoscalar and it is known at the NLO accuracy [98]. By means of our code, we obtain

$$\frac{\Gamma(H \to \Upsilon\gamma)}{\Gamma(H \to b\bar{b})} \quad = \quad 6.17 \cdot 10^{-7}\,, \tag{2.54}$$

where we have used $m_H = 120$ GeV, $\langle O_\Upsilon(^3S_1^{[1]})\rangle = 9.28$ GeV^3 and $\alpha_{EM} = 1/137$.

The BR's for both decay modes in the SM (and also in SUSY, since possible large $\tan\beta$ enhancements cancel in the ratio of the widths), are found to be rather small, especially considering that the branching ratio of the quarkonium state into leptons has yet to be included.

2.6.2 $\gamma\gamma \to J/\psi + X$ at LEP II

J/ψ production in $\gamma\gamma$ collisions at LEP II ($\sqrt{S} = 196$ GeV) has been studied in Ref [99]. In that paper, the direct ($\gamma\gamma$), the single resolved (γg) and the double resolved (gg) components have been taken into account. However, the only direct contribution that has been considered is the color-octet transition

$$\gamma\gamma \to c\bar{c}\left(^3S_1^{[8]}\right) g\,, \tag{2.55}$$

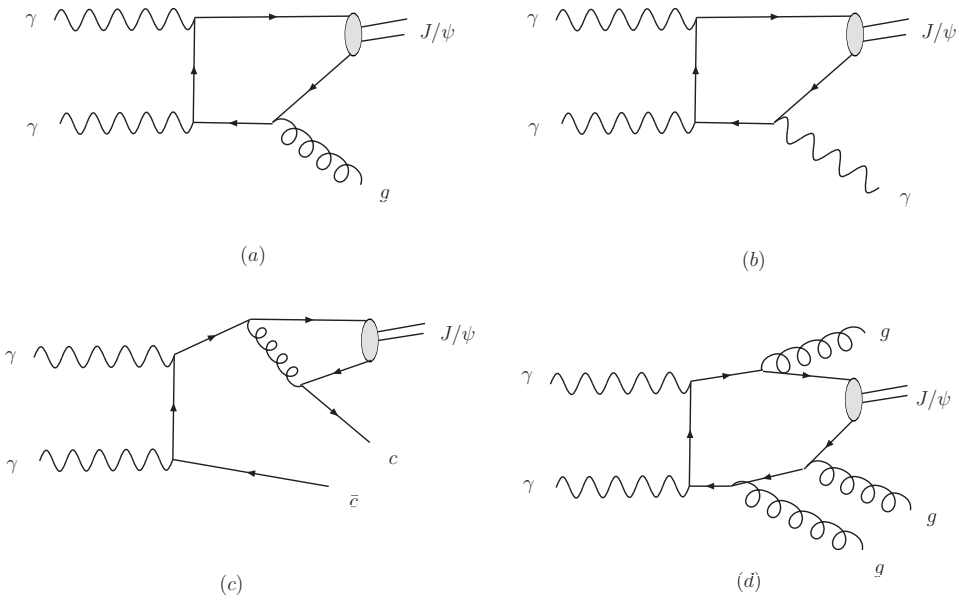

Figure 2.10: J/ψ direct photoproduction. Production mechanism (a) proceeds via a ${}^3S_1^{[8]}$ state, while the photon-associated (b), the $c\bar{c}$-associated and the multi-gluon (d) mechanisms can proceed via a color-singlet transition.

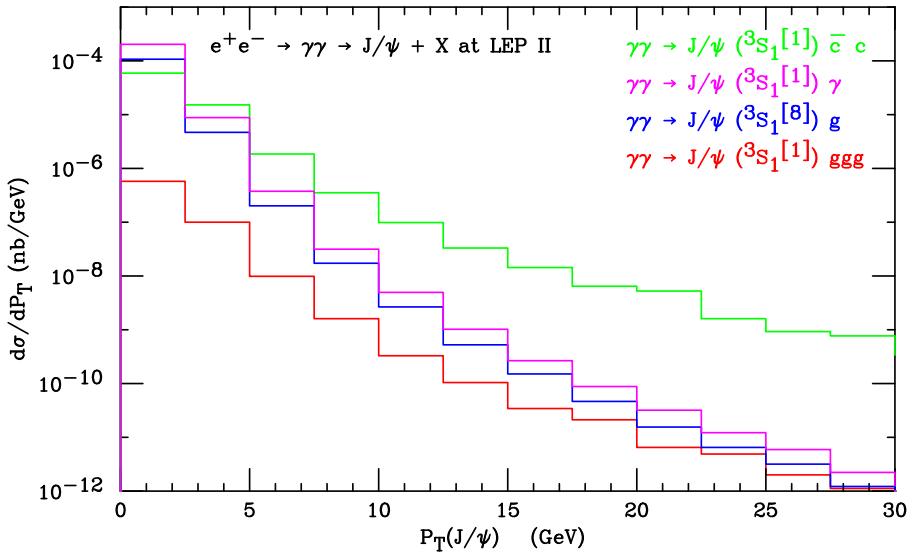

Figure 2.11: Transverse momentum distributions for J/ψ production in $\gamma\gamma$ collisions

displayed in Fig. 2.10 (a). We now address the evaluation of the color-singlet J/ψ production in (unresolved) $\gamma\gamma$ interactions. Owing to color conservation, the final state $c\bar{c}\left({}^3S_1^{[1]}\right) g$ is forbidden. However, if we turn the gluon into a photon, the corresponding α_{EM}^3-process is allowed [Fig. 2.10 (b)]. Charge conjugation conservation forbids the final state $c\bar{c}\left({}^3S_1^{[1]}\right) gg$, so the only color-singlet process at order $\alpha_{EM}^2\alpha_S^2$ is the associated production of a $c\bar{c}$ pair [Fig. 2.10 (c)]. Finally, the channel $J/\psi+$ light partons occurs at order $\alpha_{EM}^2\alpha_S^3$ [Fig. 2.10 (d)], so the Born-level contributions for the color-singlet production are given by

$$\gamma\gamma \to c\bar{c}\left({}^3S_1^{[1]}\right)\gamma, \qquad \gamma\gamma \to c\bar{c}\left({}^3S_1^{[1]}\right)c\bar{c}, \qquad \gamma\gamma \to c\bar{c}\left({}^3S_1^{[1]}\right)ggg. \quad (2.56)$$

Note also that the final state $c\bar{c}\left({}^3S_1^{[1]}\right) gq\bar{q}$ is also allowed, but is not finite: the fragmentation part $\gamma \to q\bar{q} \to q\bar{q}g$ is effectively included in the single-resolved contributions.

Using the Weiszäcker-Williams approximation at LEP2, $\alpha_S = 0.189$, $m_{J/\psi} = 2m_c = 3$ GeV, $\alpha_{EM} = 1/137$, $\langle O\left({}^3S_1^{[1]}\right)\rangle = 1.16$ GeV^3, $\langle O\left({}^3S_1^{[8]}\right)\rangle = 1.06 \cdot 10^{-2}$ GeV^3, we obtain the P_T spectra displayed in Fig. 2.11 for the color-singlet and color-octet processes. We find that the associated $c\bar{c}$ production is by far the dominant one for $p_T(J/\psi) > 5$ GeV.

Chapter 3

Quarkonium phenomenology

3.1 Charmonium production in e^+e^- collisions

Quarkonium production in electron-positron annihilation provides a rich ground to test the factorization principles of NRQCD. Both exclusive and inclusive measurements have been reported at B-factories [76, 77, 100], and have been compared intensively with theoretical predictions for several years.

One of the most striking result reported by the Belle and BABAR collaboration is the cross section for exclusive $J/\psi + \eta_c$ production [77, 100]. The measurement appeared to be one order of magnitude larger than the leading order NRQCD prediction [74, 75], a situation which has been referred to as the largest discrepancy in the standard model [101]. The full NLO correction, computed in [102, 103], was shown to be large, pushing the predicted cross section closer to the measurement. As the v^2 correction [74] proved to be large, it was then suggested that a non-relativistic expansion was not appropriate to describe this process, and an alternative approach in term of a light cone wave function was proposed to reproduce the measured cross section [104]. A following work then showed that part of the enhancement in the light-cone approach actually corresponds to correction of relative-order α_s in the NRQCD formalism [105]. Moreover, a resummation of a class of relativistic corrections to S-wave states production [64] demonstrates that the NRQCD expansion is actually well behaved. Applying this resummation and taking into account the fragmentation contribution to the pure QED amplitude, the inclusion of the effects of the running of α and the inclusion of the contribution that arises from the interference between the relativistic corrections and the corrections of next-to-leading order in α_s, a refined analysis of

the theoretical uncertainties showed that the discrepancy was resolved [106]. More recently, the factorization theorem on which this NRQCD result is based was proved to hold at all orders in α_s up to corrections of order m_c^2/s [52]. The Belle collaboration also reported a measurement of double production of S-wave + P-wave charmonium states. The corresponding NRQCD prediction at NLO accuracy [53] in α_s was shown to reach the lower bound of experiment.

Another chalenge was addressed to the quarkonium production community with the measurement of the inclusive J/ψ cross section [76, 107, 108]. In this case as well, the leading-order NRQCD prediction [57, 109, 110] turns out to underestimate the experimental yield. Moreover, the Belle collaboration reported that of most the reconstructed J/ψ are produced in association with charm mesons: the most recent measurement [108] for the ratio

$$R_{cc} = \frac{\sigma[e^+e^- \to J/\psi + c\bar{c} + X]}{\sigma[e^+e^- \to J/\psi + X]} = 0.63 \pm 0.23 \tag{3.1}$$

is in disagreement with the NRQCD leading-order prediction $R_{cc} = 0.1 - 0.3$. The computation of the QCD correction for both processes $e^+e^- \to J/\psi + c\bar{c} + X$ and $e^+e^- \to J/\psi + gg + X$ have been completed [111, 112] recently, and found to bring the ratio R_{cc} in better agreement with the experimental result. In the meantime, standard NRQCD factorization has been shown to break down for the associated production at NNLO in α_s, due to color transfer between co-moving active and passive charm quarks [50, 51]. This effect is expected to catalyze the production rate when one of the charm quark is produced in the same direction as the J/ψ. It could in principle be quantified experimentally by measuring the angular separation bewteen the J/ψ and the charm meson.

3.1.1 Relativistic correction to inclusive J/ψ production

The relativistic correction to inclusive J/ψ production is another source that can affect the ratio R_{cc} defined in the previous Section. We present here an original computation of the v^2 correction to $J/\psi + c\bar{c}$ production at B-factories. In the writing of this thesis, the computation of the v^2 correction to this process was achieved by the authors of Ref. [113]. In that work, they decided not to expand the phase-space measure in v. Instead they used the physical mass of the J/ψ in the phase-space factor so that corrections of higher-order in v in the phase space are taken into account to all orders in v. In contrary to the procedure in Ref. [113], we also expand the phase-space measure and find that the resulting correction is the dominant source of v^2 correction. Moreover, we argue that the order-v^4 correction to the wave function is small, so that the NRQCD expansion is well behaved.

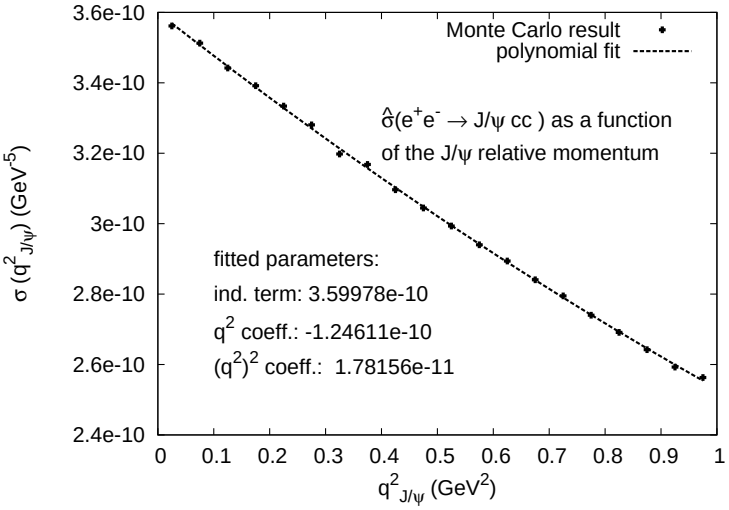

Figure 3.1: Short distance cross section $\hat{\sigma}(e^+e^- \to J/\psi c\bar{c})$, as a function of the relative momentum in the spin one charm-quark pair.

We follow essentially the same approach as in Section 2.1.4, i.e., we compute the short-distance cross section as a function of the relative momentum associated with the bound heavy-quark pair. Using $m_c = 1.5$ GeV, $\sqrt{s} = 10.58$ GeV, $\alpha_{em} = 1/129.6$, $\alpha_s = 0.258$, we obtain the curve displayed in Fig. 3.1. We fit the result with a polynomial in $\boldsymbol{q}^2_{J/\psi}$:

$$\hat{\sigma}(\boldsymbol{q}^2_{J/\psi}) = a + b\boldsymbol{q}^2_{J/\psi} + c(\boldsymbol{q}^2_{J/\psi})^2 + \dots \tag{3.2}$$

where $a, b, c, \dots$ are obtained by the fitting procedure. The value of a gives the cross section at leading order in v:

$$\sigma^0 = a \times \langle \mathcal{O}^{J/\psi}(^3S_1) \rangle = 163 \text{ fb}, \tag{3.3}$$

if we set $\langle \mathcal{O}^{J/\psi}(^3S_1) \rangle = 1.16$ GeV^3. The v^2 correction is approximated by the ratio of b and a

$$\frac{1}{\hat{\sigma}_0} \frac{d\hat{\sigma}}{d\boldsymbol{q}^2_{J/\psi}}\Big|_{\boldsymbol{q}^2_{J/\psi}=0} = \frac{b}{a} = -0.34 \text{ GeV}^{-2}\,, \tag{3.4}$$

If we use the result in Ref. [64] for the order-v^2 NRQCD matrix element

$$m_c^2 v^2 = 0.5, \tag{3.5}$$

we find that the order-v^2 correction decreases the cross section by only 8 %. The decrease is essentially coming from the reduction of the phase-space when the relative momentum is increased. We learn from the linearity of Fig. 3.1 that the v^4 correction is much smaller than the v^2 correction, so that the expansion is well behaved.

We can try to apply the same procedure in order to extract the order-v^2 correction that is associated with the process $e^+e^- \to J/\psi gg$. However, if we consider a non-vanishing value of the relative velocity v between the heavy quarks in the J/ψ, the short-distance coefficient develops infrared pôles that should be reabsorbed into color-octet matrix elements. One should therefore achieve the computation analytically, in dimensional regularization for example, in order to regularize the pôles. Here, we merely note that we can extract the order-v^2 correction for the cross section restricted to a limited phase-space area defined by a lower cutoff on the gluon energies. Our computation reproduces the results in [57] when we set the relative velocity and the cutoff to zero. We then compute the short-distance coefficient as a function of v. For the cutoff $E_g > 1$ GeV, we obtain

$$\frac{1}{\hat{\sigma}_0}\frac{d\hat{\sigma}}{d\boldsymbol{q}^2_{J/\psi}}\Big|_{\boldsymbol{q}^2_{J/\psi}=0} = \frac{b}{a} = 0.08 \text{ GeV}^{-2}\,, \tag{3.6}$$

whereas this value goes to zero when we increase the value of the cutoff to 1.5 GeV. We can therefore expect the v^2 correction to be small for this process as well. We conclude that the relativistic corrections have a very small impact on the ratio R_{cc} defined earlier.

3.1.2 Inclusive η_c production

The production of an η_c state from e^+e^- collisions has been studied in the context of associated production [110]. A typical Feynman diagram for this process is displayed in Fig. 3.2 (a). Using the inputs $\alpha_S = 0.26$, $\alpha_{EM} = \frac{1}{137}$, $\langle O\left({}^1S_0^{[1]}\right)\rangle = 0.387\,\text{GeV}^3$, we obtain

$$\sigma(e^+e^- \to \eta_c + c\bar{c}) = 58.7\,\text{fb}\,, \tag{3.7}$$

in agreement with the result obtained in Ref. [110].

The contribution to η_c production coming from associated production with light partons has not been studied so far. The reason is that, for color-singlet production, neglecting the exchange of an off-shell Z, there is no such processes at order $\alpha_{EM}^2\alpha_S^2$, owing to color conservation and charge-conjugation symmetry. However, at order $\alpha_{EM}^2\alpha_S^3$ the following processes can occur:

$$e^+e^- \to \eta_c ggg, \qquad e^+e^- \to \eta_c q\bar{q}g\,, \tag{3.8}$$

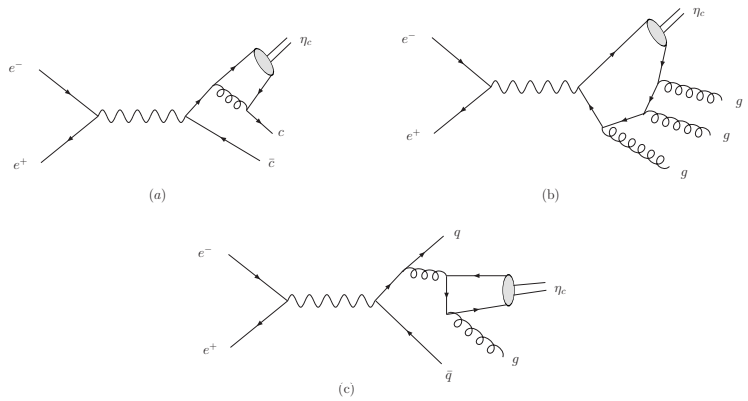

Figure 3.2: Representative diagrams for η_c electroproduction via color-singlet transition: at order α_S^2 in association with a $c\bar{c}$ pair (a), and at order α_S^3 with three gluons (b) and with a light-quark pair (c).

which are finite and could give a non-negligible cross section owing to the larger phase space available. Typical Feynman diagrams for these processes are shown in Fig. 3.2 (b,c). Using our generator MadOnia, we checked that the channel η_c+ light partons constitutes approximately 10% of the inclusive cross section. The plots in Fig. 3.3 display the differential cross section with respect to $z = \frac{2|\boldsymbol{P}_{\eta_c}|}{\sqrt{s}}$, the fraction of momentum taken by the η_c, and with respect to the transverse momentum of the η_c. The total cross sections are given by

$$\sigma(e^+e^- \to \eta_c ggg) = 3.72\,\text{fb}, \quad \sigma(e^+e^- \to \eta_c q\bar{q}g) = 1.63\,\text{fb} \tag{3.9}$$

As a result, the associated production is dominating the η_c production:

$$\frac{\sigma(e^+e^- \to \eta_c c\bar{c})}{\sigma(e^+e^- \to \eta_c X)} = 91.6\% \tag{3.10}$$

This feature is to be contrasted with the case of the inclusive J/ψ production, where the associated production is predicted to be subdominant at leading order. It would therefore be interesting to measure the ratio in Eq. (3.10).

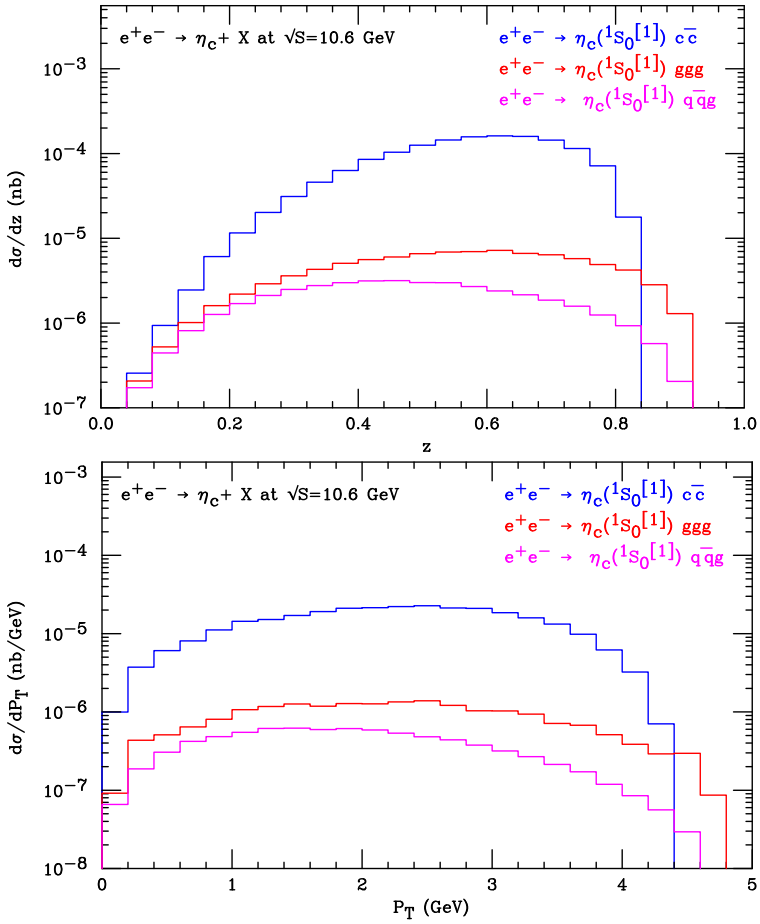

Figure 3.3: Momentum fraction (upper) and transverse momentum (lower) of an η_c in e^+e^- collisions at $\sqrt{s} = 10.6$ GeV.

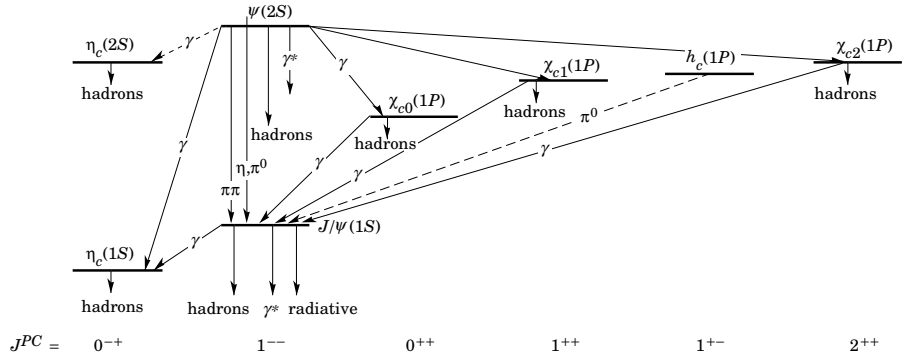

Figure 3.4: Spectrum and transitions of the charmonium family (from Ref. [114]).

3.2 Inclusive quarkonium production in hadron colliders

Inclusive J/ψ, ψ' and $\Upsilon(nS)$ production at hadron colliders has been of interest for many years. As we mentioned earlier, such states have the right quantum numbers to decay into a pair of leptons via a virtual photon. They therefore offer a uniquely clean signature, provided that the resolution of lepton momenta is good.

The most accurate measurements for quarkonium hadroproduction at high energy come from the Tevatron proton-antiproton collider at Fermilab. The Tevatron first operated at a center-of-mass energy of $E_{\text{cm}} = 1.8$ TeV (Run I). In 2002, the energy was increased to reach 1.96 TeV. The two collaborations CDF and D0, whose detectors record the signatures from the $p\bar{p}$ collisions at the Tevatron, have both published measurements of quarkonium cross sections. New analyses are still being carried on at the current time.

The experimental number of quarkonium events reconstructed through the leptonic channel $\mathcal{Q}(1^{--}) \rightarrow l^+l^-$ by the CDF and D0 collaborations cannot be compared to the prediction of NRQCD for the *direct* production, in which it is assumed that the heavy-quark pair is created from the initial partons over distance of order $\frac{1}{m_Q}$ or smaller. Indeed, the production of the state $\mathcal{Q}$ can proceed via the decay of a heavier resonant state. In the case of charmonium production, a fraction of reconstructed J/ψ and ψ' originates from the decay of a B meson. As the B meson decays weakly, its lifetime leads to a displaced vertex (called a secondary vertex), which in principle can be resolved experimentally.

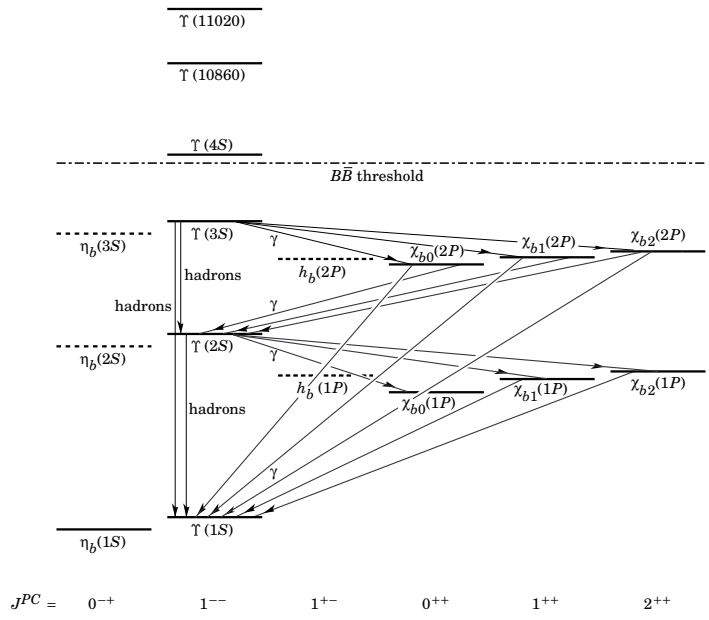

Figure 3.5: Spectrum and transitions of the bottomonium family (from Ref. [114]).

The J/ψ can also originate from the decay of an excited charmonium state as illustrated in Fig. 3.4. The feed-down from charmonium states with a mass above $2m_D$ decay is negligible, as these states decay almost exclusively into charm mesons. In the case of ψ' production, as this state is the heaviest state below the charm meson threshold, there is no feed-down from charmonium states. Similarly for the bottomonium family, the feed-down from excited states has to be considered only for the $\Upsilon(1S)$ and $\Upsilon(2S)$, but not for the $\Upsilon(3S)$ which lies just below the double-B-meson threshold (see Fig. 3.5).

In order to distinguish the different modes for the production of quarkonium states in the following, we use the conventional terminology:

- the production is *prompt* if it does not come from the decay of a B-meson,
- the production is *direct* if it is prompt and it does not come from an excited charmonium state.

The CDF detector has a silicon microstrip detector (SVX) close to the beam that allows the separation of the non-prompt fraction of J/ψ or ψ' production. Up to now, there has been no measurement of the prompt fraction by the D0 collaboration.

The direct production was also measured by the CDF collaboration [115]. In the case of the J/ψ, the feed-down contribution from χ_c states has been identified for events with $P_T(J/\psi) > 4$ GeV by observing the photon that originates in the electromagnetic transition $\chi_c \to J/\psi\gamma$. The feed-down from the ψ' was estimated from the prompt ψ' cross section, and from Monte-Carlo simulation of the decays $\psi' \to J/\psi X$. In the case of the $\Upsilon(1S)$, the fraction of events originating from $\chi_b(1P)$ states and $\chi_b(2P)$ states has been measured for events with $P_T(\Upsilon(1S)) > 8$ GeV only [116].

Measurements of quarkonium cross sections at the Tevatron have been extensively compared to NRQCD predictions (for a recent review, see [101, 117]). In contrast with the situation in e^+e^- collisions, the rôle of the color-octet transitions has been highlighted, as the associated short-distance cross sections are enhanced by a large factor compared to the order-α_s^3 cross section of a heavy-quark pair in a color-singlet ${}^3S_1$ state. However, despite the successes of NRQCD, vector-like quarkonium production at the Tevatron is still a subject of debate. Considering the P_T differential cross sections measured by the CDF collaboration, it seems that color-octet transitions are needed to fill the gap between the color-singlet yield and the data [37, 66, 65, 13]. But once we use the color-octet LDME's fitted to reproduce the cross section, the NRQCD prediction for the polarization [62, 118, 119, 120, 121] disagrees with the CDF measurement [15]. Up to now, it is still unclear which transitions dominate heavy-quarkonium hadroproduction

In view of this situation, it is worthwhile to improve the accuracy of the NRQCD predictions. Concerning inclusive production, one should try to extend the knowledge of cross sections beyond the leading order in α_s and v. Relativistic corrections to the color-singlet yield prove to be very small in the case of S-wave state production [122], as we confirmed with our automatic procedure that is described in Section 2.1.3. On the contrary, higher-order-in-α_s contributions are especially important for color-singlet production: as was analyzed in Refs. [91, 123], NLO corrections raise the differential cross section for the color-singlet transition by a large factor in the region of large transverse momentum.

3.2.1 Higher-order corrections to the color-singlet cross section

The cross section for $p\bar{p} \to \mathcal{Q} + X$ with $\mathcal{Q} = J/\psi$ or Υ, has been computed in [91, 123] at NLO accuracy. Here we use the implementation in MCFM [91, 124]. As we have seen in Chapter 2 Section 2.5, the real polarized amplitude is provided by MadOnia. The quarkonium state is decayed into leptons, keeping track of the spin correlations. This allows us to extract the polarization, as is discussed in Section 2.2.

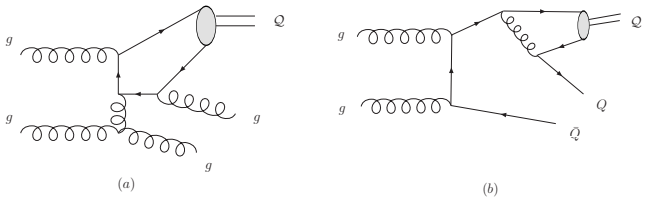

Figure 3.6: Typical Feynman diagrams for (a) J/ψ or Υ hadroproduction + two jets, (b) J/ψ or Υ production plus a heavy-quark pair of the same flavor.

In our calculation, we set $m_c = 1.5$ GeV and $m_b = 4.75$ GeV. We use the PDF set CTEQ6L1 (resp. CTEQ6_M) [125] for LO (resp. NLO) cross sections, and always keep the factorization scale equal to the renormalization scale: $\mu_f = \mu_r$. The central scale is fixed at $\mu_0 = \sqrt{4m_c^2 + P_T^2}$. We use the saturation approximation to relate the long-distance matrix elements for production to those involved in quarkonium decays. We then use the values related to the Buchmüller-Tye potential [31]: $\langle \mathcal{O}_1^{J/\psi}\left({}^3S_1\right)\rangle = 1.16$ GeV^3 and $\langle \mathcal{O}_1^{\Upsilon}\left({}^3S_1\right)\rangle = 9.28$ GeV^3.

In the following, we consider that the production is prompt (i.e. the quarkonium does not come from the decay of a B hadron) and direct (i.e. the quarkonium does not originate from the decay of an excited quarkonium state). The results are compared with the data collected by the CDF collaboration at the Tevatron. For J/ψ production, we consider the prompt measurement at $\sqrt{s} = 1.96$ TeV in Ref. [126], multiplied by the average direct fraction obtained in [115]. For $\Upsilon(1S)$ production, we consider the prompt measurement at $\sqrt{s} = 1.8$ TeV in Ref. [127], multiplied by the average direct fraction obtained in Ref. [116].

Differential cross section at NLO

The differential cross section at NLO is displayed in Fig. 3.7. The uncertainty bands correspond to the variation of the scale $\frac{\mu_0}{2} < \mu_{r,f} < 2\mu_0$, and to the variation of the heavy quark masses 1.4 GeV $< m_c <$ 1.6 GeV, 4.5 GeV $< m_b <$ 5 GeV. These uncertainties have been combined in quadrature. The NLO yield is plotted in yellow. For comparison, we also show the LO cross section in dark blue. The ligh-blue band corresponds to the associated production $\mathcal{Q} + Q\bar{Q}$, which is a fraction of the NLO yield.

For J/ψ production, NLO contributions raise the cross section by more than one order of magnitude at large P_T. Indeed, at α_s^4, new channels become available to produce a high-P_T J/ψ at a lower kinematic price: the parton-level processes $gg \to J/\psi + gg$

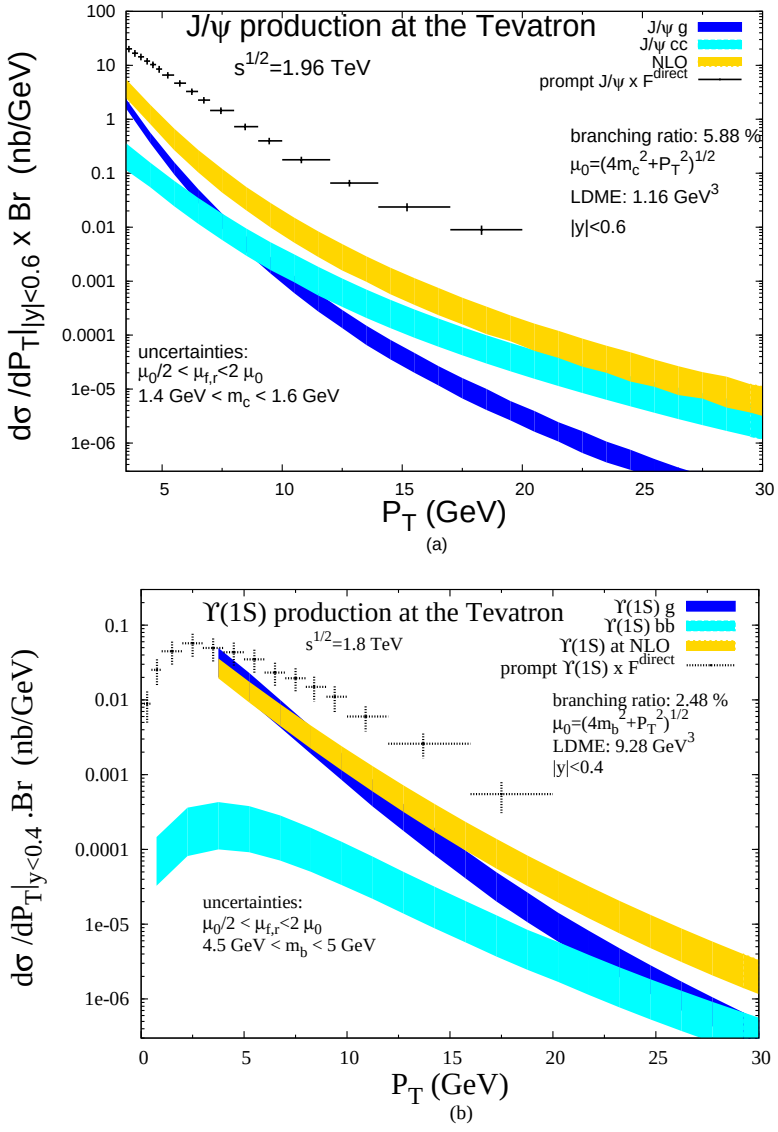

Figure 3.7: (a) J/ψ production via a color-singlet transition, up to NLO accuracy. Experimental points are from [115, 126]. (b) Υ production via a color-singlet transition, up to NLO accuracy. Experimental points are from [116, 127].

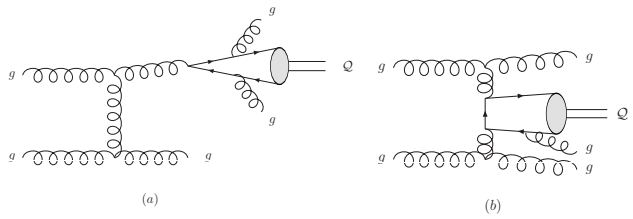

Figure 3.8: Typical Feynman diagrams for J/ψ or Υ hadroproduction + three jets: (a) color-singlet gluon fragmentation channel (b) high-energy-enhanced contribution.

and $gg \rightarrow J/\psi + c\bar{c}$ (see Fig. 3.6) behave as $\frac{1}{P_T^6}$ and $\frac{1}{P_T^4}$, respectively, at large transverse momentum. This also explains why the associated production $J/\psi + c\bar{c}$ dominates the NLO yield at large P_T. Although NLO contributions reduce the gap between the color-singlet prediction and the CDF data, there is still a discrepancy of more than than an order of magnitude.

The situation for the $\Upsilon(1S)$ is similar, although the asymptotic behavior is reached at much higher values of P_T, owing to the fact that $m_b > m_c$. In particular, the associated production $\Upsilon + b\bar{b}$ remains a subdominant fraction among the NLO contributions in the region $P_T < 30$ GeV, as it suffers from a phase-space suppression owing to the large invariant mass in the final state. We also note that the gap between the color-singlet prediction at NLO and the CDF data is much smaller than in the case of J/ψ production.

Contributions from $\mathcal{Q} + 3$jets

As we can see from Fig. 3.7, the color-singlet production at NLO in α_s fails to reproduce the data, especially at large P_T. The associated production $\mathcal{Q} + Q\bar{Q}$, has the right P_T slope, but overall it is suppressed in comparison to the measurement. Therefore, it seems that a production mechanism with a P_T behavior that is similar to that in the associated production is missing.

If we consider the color-singlet production at order-α_s^5, new parton-level mechanisms become available. The gluon fragmentation channel via a color-singlet transition (Fig. 3.8, a) is one of them, and has the correct P_T shape (asymptotically as $\frac{1}{P_T^4}$). At this order, the quarkonium can also produced by two slightly off-shell gluons (plus the emission of a third one) that give part of the transverse momentum to the quarkonium state (Fig. 3.8, b). This contribution has been approximated in the k_t factorization approach [42, 43, 44, 45, 47]. These α_s^5 contributions, or more generally $p\bar{p} \rightarrow \mathcal{Q} +$

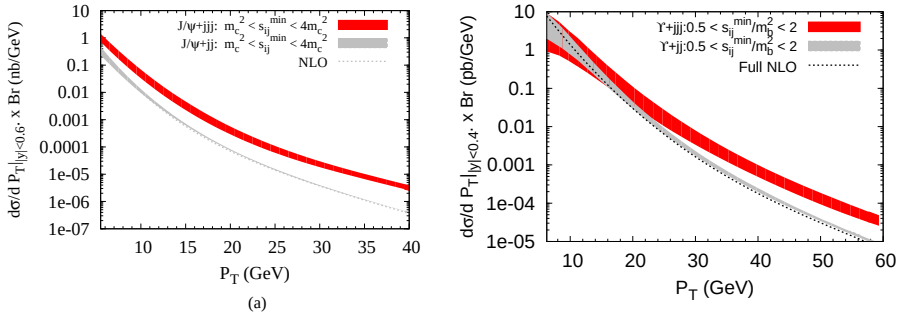

Figure 3.9: (a) J/ψ production at the Tevatron, run II: NLO production without the associated production (dotted line), $J/\psi + 2$ light jets (gray band), $J/\psi + 3$ light jets (red band). (b) Υ production at the Tevatron, run I: NLO production without the associated production (dotted line), $\Upsilon + 2$ light jets (gray band), $\Upsilon + 3$ light jets (red band).

$3j$, provide us with new mechanisms to produce a high-P_T quarkonium at a lower kinematic cost. They are therefore expected to dominate over the production of $\mathcal{Q}+1j$ and $\mathcal{Q}+2j$ at sufficiently large transverse momentum.

In order to quantify these arguments, we present here an estimate of these dominant order-α_S^5 contributions at large p_T, bypassing the presently out-of-reach inclusive calculation of $p\bar{p} \to \mathcal{Q} + X$ at NNLO accuracy. We consider the whole set of α_S^5 processes contributing to the color-singlet production of a quarkonium (either J/ψ or Υ) associated with three light partons. We use MadOnia to generate the squared amplitude of each subprocess. In order to protect the integrated cross section from soft and collinear divergences, we impose a "democratic" invariant-mass cut s_{ij}^{min} of the order of m_Q^2 to any pair of light partons, so that the phase-space integration remains finite. For new channels opening up at α_S^5, the dependence on the value of s_{ij}^{min} is expected to be small in the region $p_T \gg m_Q$, since no collinear or soft divergences can appear there. For channels whose Born-level contribution occurs at α_S^3 or α_S^4, the invariant-mass cut results in potentially large logarithms of s_{ij}/s_{ij}^{min} in the differential cross sections. However, these logs factorize over lower order amplitudes that are suppressed by powers of p_T compared to the dominant α_S^5 contributions. The result is that the sensitivity to the value chosen for the minimal invariant mass cut s_{ij}^{min} is expected to die away as p_T increases. Also, this behavior can already be checked explicitly for the NLO cross section: we can approximate the NLO yield by the real α_s^4 contribution $\mathcal{Q} + 2j$, with a cut on the invariant mass of any pair of light partons. The sensitivity to the s_{ij}^{min} cut is illustrated in Fig. 3.9. The gray bands correspond to

the production of $\mathcal{Q}+2$ jets, and converge rapidly to the NLO cross sections[1] (dotted lines). The bands associated with $\mathcal{Q}+3$ jets (in black) are much wider, especially in the region $P_T \approx m_Q$. Still we see that the uncertainty related to the choice of the cut s_{ij}^{min} decreases as P_T increases. We note also that the contribution $\mathcal{Q}+3$ jets lies well above the NLO yield at large P_T, both for the J/ψ and Υ cases.

We now add the contribution from $\mathcal{Q}+3$ jets to the NLO color-singlet cross section for direct quarkonium production, and compare the resulting curve (called NNLO*) with the CDF data. The corresponding plots are displayed in Fig. 3.10. We only consider the uncertainties resulting from the variation of the scales μ_r and μ_f, and from the variation of the cut s_{ij}^{min}. The values of the quark masses remain fixed at $m_c = 1.5$ GeV and $m_b = 4.75$ GeV.

In the case of J/ψ production, we see that the gap between the color-singlet yield and the CDF data is much smaller after the inclusion of $J/\psi + 3j$ channels. However the P_T shape is not well described: despite the inclusion of $J/\psi + 3$ jet channels, the differential cross section still drops too fast compared to the CDF data. We also note that the color-octet contribution has the right shape with P_T to fill the gap between the color-singlet prediction and the data.

The situation for the Υ is rather different. First, all the experimental points are compatible with the NNLO* uncertainty band associated with the color-singlet production. Second, even if the prediction of the normalization is rather poor due to the large width of the uncertainty band, the experimental slope in P_T seems to be well reproduced.

ψ' differential cross section

The CDF collaboration has recently carried on a new measurement of the prompt ψ' cross section [128], using 1.1 fb^{-1} data collected at run II. This analysis covers the kinematic range 2.0 GeV $< P_T(\psi') < 30$ GeV and $|y| < 0.6$. As for the case of previous J/ψ and ψ' cross section measurements, the fraction of prompt ψ' events is separated from the decay of the long-lived b hadrons, as the second production mode can be tagged by the presence of a secondary vertex from which the ψ' originates.

All the arguments presented in the previous section apply naturally to the hadroproduction of the ψ'. The resulting prediction can be compared directly to the CDF measurement, as the feed-down from excited states is negligible. The comparison is displayed in Fig. 3.11. As for the J/ψ case, the real contribution at order-α_s^5 is seen

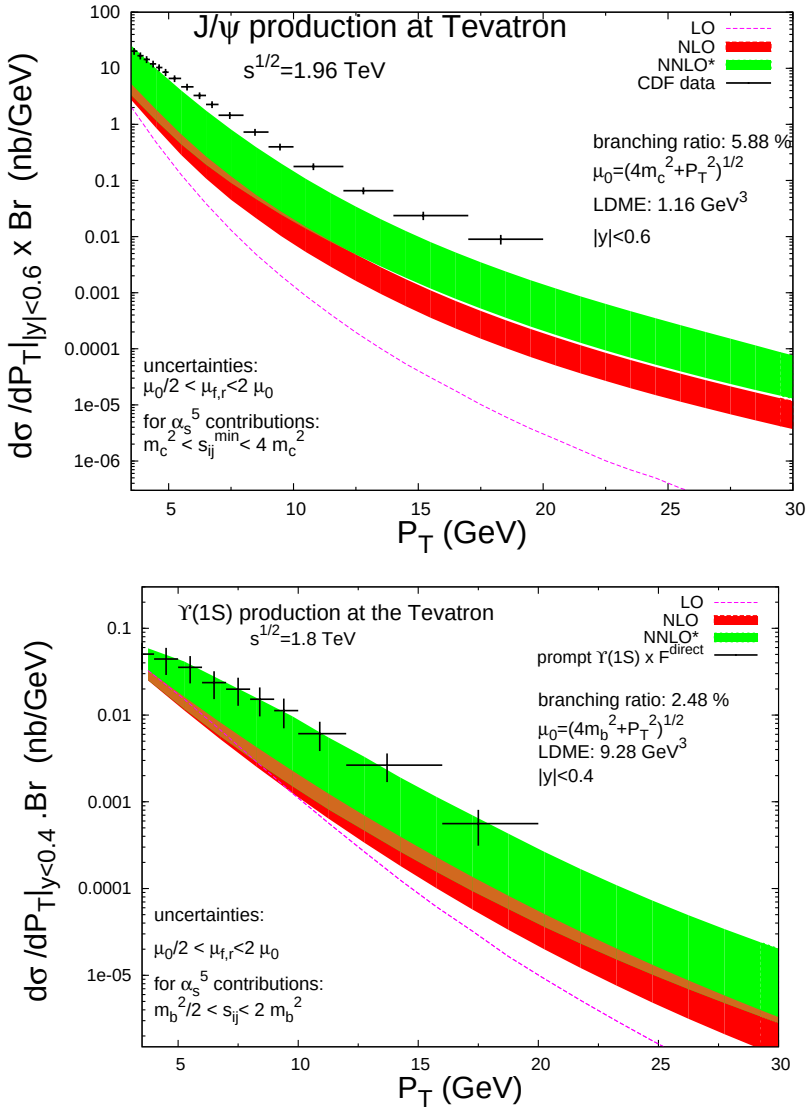

Figure 3.10: (a) J/ψ production at the Tevatron, Run II. The light-gray band is the NLO yield, the dark-gray band is the sum of the NLO plus the α_s^5 contributions. (b) Υ production at the Tevatron, run I. Same legend as in (a).

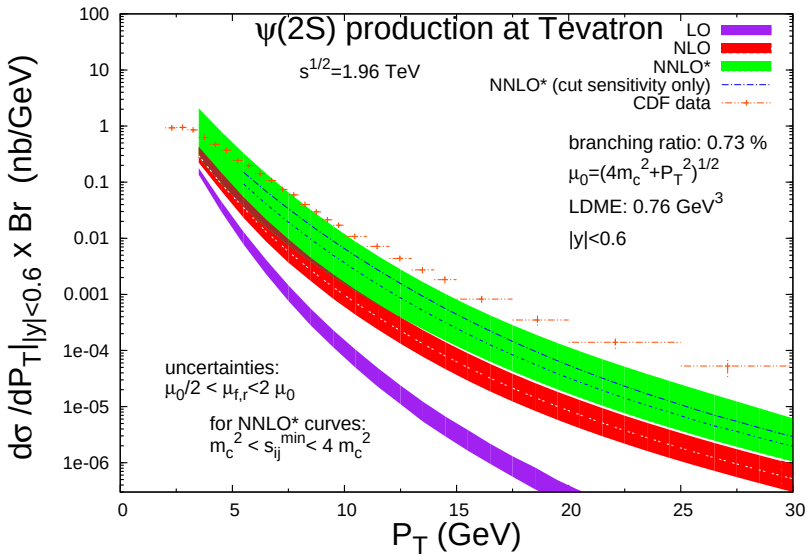

Figure 3.11: ψ' production at the Tevatron, Run II. The red band is the NLO yield, the green band is the sum of the NLO plus the α_s^5 contributions

to increase the differential cross section by a large factor. Still, at large transverse momentum, the color-singlet yield fails to reproduce the data.

3.2.2 Impact of α_s corrections on the polarization

We now turn to the polarization observable. J/ψ and Υ states have been decayed into leptons in our code, keeping track of the spin correlations. Defining θ as the angle between the ℓ^+ direction in the quarkonium rest frame and the quarkonium direction in the laboratory frame, we find that the normalized angular distribution $I(\cos\theta)$ reads

$$I(\cos\theta) = \frac{3}{2(\alpha+3)}(1+\alpha\,\cos^2\theta)\,, \tag{3.11}$$

from which we have extracted the polarization parameter α bin by bin in P_T.

As is shown in Fig. 3.12, α_s corrections have a strong impact on the polarization parameter. For the Υ, QCD corrections bring the polarization parameter down to ≈ -0.5 at middle-large P_T. The Υ produced in association with a b-quark pair is unpolarized, but this has almost no effect on the polarization at NLO, as the associated production

[1] In Fig. 3.9, the associated production is not included in the NLO curve.

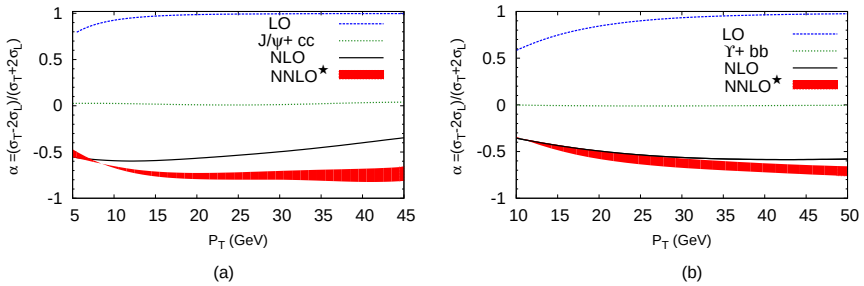

Figure 3.12: (a) Polarization parameter for J/ψ production at the Tevatron, run II. (b) Polarization parameter for Υ production at the Tevatron, run I.

is only a small fraction of the NLO yield below $P_T \approx 40$ GeV. The channels $\Upsilon + 3$ jets give rise to the same value of α as the one at NLO.

For the J/ψ case, QCD corrections also push down the value of the polarization parameter. However, the situation is slightly different: the associated production, from which originate unpolarized J/ψ's, becomes rapidly a substantial fraction of the NLO yield. For this reason, the polarization parameter associated with the production at NLO increases at large P_T. This result agrees with the one in Ref. [123].

3.2.3 Contribution from charm-pair rescattering mechanism

A new mechanism for heavy-quarkonium production in high-energy collisions called the "s–channel cut" was proposed by Lansberg *et al.* in 2005 [129]. It can be identified as a contribution to the imaginary part of the amplitude for quarkonium production in gluon-gluon collisions that corresponds to a Cutkosky cuts through Q and $\bar{Q}$ lines only. It is thus associated with a discontinuity of the amplitude in the square of the center-of-mass energy of the colliding gluons. A physical description of this mechanism is $Q\bar{Q}$ rescattering. It corresponds to the creation of the heavy quark and antiquark through the parton scattering process $gg \to Q\bar{Q}$ followed by the formation of quarkonium through the rescattering of the $Q\bar{Q}$ pair. Lansberg *et al.* proposed a model to estimate this contribution to inclusive J/ψ production. In this model, they introduce a vertex function Γ_μ that connects the perturbative charm quarks to the J/ψ. The on-shell condition is not forced for the pertubative charm quarks that attach to the vertex function. Gauge invariance is restored by the introduction of a four-point vertex $\Gamma_{\mu\nu}$. The free parameters associated with the vertex function introduce large theoretical uncertainties. Moreover, the prescription given by Lansberg *et al.* is spe-

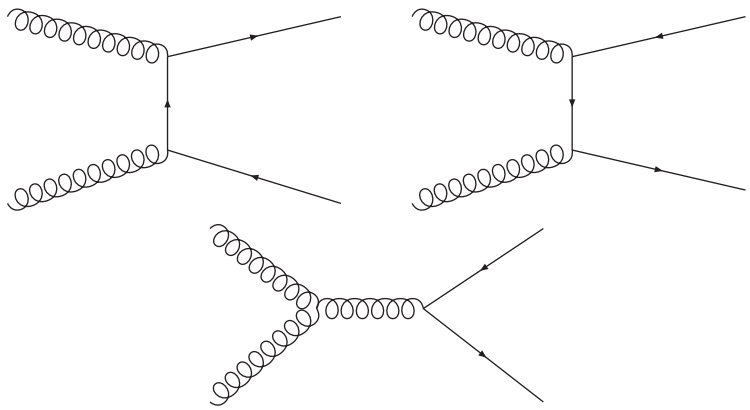

Figure 3.13: Feynman diagrams for $g\,g \to c\,\bar{c}$.

cific to J/ψ hadroproduction and does not generalize easily to include higher-order corrections.

As is discussed in Ref. [130], the s–channel cut mechanism for J/ψ production arises naturally at higher order in the theory of NRQCD, where no extra parameters are introduced. The leading imaginary terms in the scattering amplitude $gg \to J/\psi g$ are of order g_s^5. Using the Cutkosky cutting rules, the imaginary part can be expressed as a sum over the s–channel cuts through the diagrams, which separate the incoming gluons from the $c\bar{c}$ pair and the gluon in the final state. At order g_s^5, the only s–channel cuts are gg cuts and $c\bar{c}$ cuts. The s–channel $c\bar{c}$ cut, which is the charm-pair rescattering term, can be expressed as an integral over the solid angle Ω_c of the charm quark in the intermediate state. At leading order in v and in α_s, the amplitude for the charm-pair rescattering contribution reads

$$\begin{aligned}&\mathrm{Im}\mathcal{M}_{c\bar{c}\,\mathrm{cut}}[g\,g \to c\bar{c}_1(^3S_1)\,g] = \\ &\frac{(\hat{s}-4m_c^2)^{1/2}}{64\pi^2\hat{s}^{1/2}}\int d\Omega_c \sum \mathcal{M}[g\,g \to c\,\bar{c}]\mathcal{M}[c\,\bar{c} \to c\bar{c}_1(^3S_1)\,g]. \qquad (3.12)\end{aligned}$$

The prefactor comes from multiplying the 2-body phase space for c and $\bar{c}$ by a factor of 1/2 from the optical theorem. The sum is over the helicities and the color indices of the intermediate c and $\bar{c}$. The first invariant matrix element $\mathcal{M}$ on the right side of Eq. (3.12) is the sum of the three Feynman diagrams for $g\,g \to c\,\bar{c}$ in Fig. 3.13. The second invariant matrix element $\mathcal{M}$ on the right side of Eq. (3.12) is the sum of the five Feynman diagrams for $c\,\bar{c} \to c\bar{c}(^3S_1^{[1]})\,g$ in Fig. 3.14. In the expression for $\mathrm{Im}\mathcal{M}_{c\bar{c}\,\mathrm{cut}}$ that comes directly from the optical theorem, the last factor in Eq. (3.12) is the complex conjugate of the invariant matrix element for $c\bar{c}(^3S_1^{[1]})\,g \to c\,\bar{c}$. The

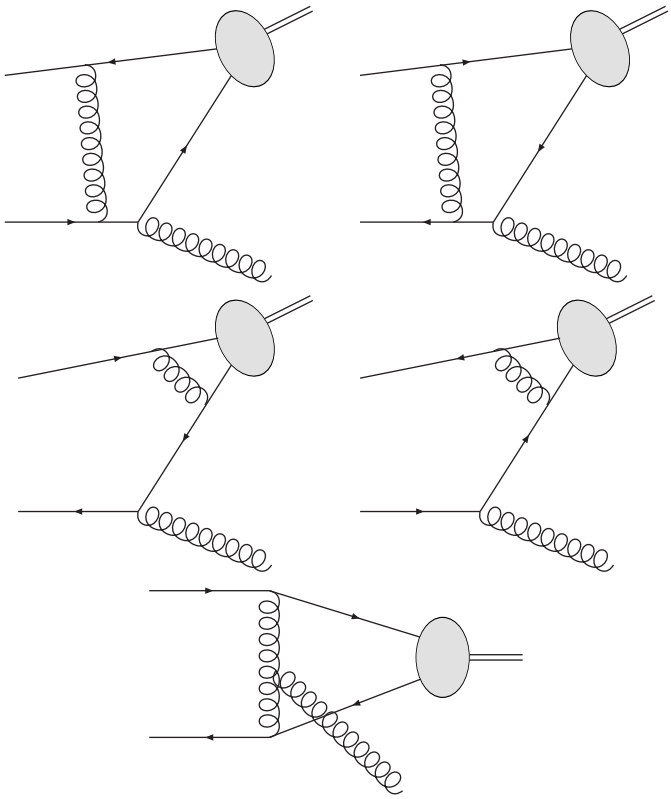

Figure 3.14: Feynman diagrams for $c\,\bar{c} \to J/\psi\, g$.

time reversal symmetry of QCD has been used to express this as the invariant matrix element for $c\,\bar{c} \to c\bar{c}(^3S_1^{[1]})\,g$.

We proceed to explain how we calculate the cross section for this process. We use a helicity basis for the polarization vectors of the gluons and the $c\bar{c}$ pair. The helicity amplitudes $\mathcal{M}[g\,g \to c\,\bar{c}]$ and $\mathcal{M}[c\,\bar{c} \to c\bar{c}_1(^3S_1)\,g]$ are evaluated with MadOnia. Squaring the amplitude in Eq. (3.12) and integrating over the two-body phase space for $c\bar{c}(^3S_1^{[1]})+g$, we obtain a 3-fold angular integral. Including the integration over parton momentum fractions, we have an 8-dimensional integral that is calculated numerically using the adaptive integration program VEGAS [85].

We now evaluate the charm-pair rescattering contribution to the inclusive color-singlet cross section for J/ψ production in $p\bar{p}$ collisions at the Tevatron. We compare our results, which have no additional parameters, to those from models for the s–channel cut contributions proposed by Lansberg et al. [129, 131]. The parton cross section for charm-pair rescattering in the color-singlet model depends only on α_s, m_c, and the NRQCD matrix element $\langle\mathcal{O}_1^{J/\psi}(^3S_1)\rangle$. To compare our results with those of Lansberg et al., we use parameters that are as close to theirs as possible. They used a large value for the charm quark mass: $m_c = 1.87$ GeV. They did not specify the scale μ that they used for the running coupling constant $\alpha_s(\mu)$, but we take both the factorization and the renormalization scales to be $\sqrt{4m_c^2 + P_T^2}$. They determined the normalization factor in their vertex Γ_μ by fitting the partial width for $J/\psi \to e^+e^-$. At leading order in α_s, the NRQCD factorization formula for the partial width for $J/\psi \to e^+e^-$ is

$$\Gamma[J/\psi \to e^+e^-] = \frac{8\pi\alpha^2}{81m_c^2}\langle\mathcal{O}_1^{J/\psi}(^3S_1)\rangle\,, \tag{3.13}$$

where we have used the relation $\langle\mathcal{O}_1^{J/\psi}(^3S_1)\rangle = 3\langle\mathcal{O}_1(^3S_1)\rangle_{J/\psi}$ between the standard NRQCD production and decay matrix elements [10]. Setting $m_c = 1.87$ GeV and $\alpha = 1/129.6$, we determine the NRQCD matrix element to be $\langle\mathcal{O}_1^{J/\psi}(^3S_1)\rangle = 1.05\,\text{GeV}^3$. In Refs. [129, 131], the momentum scale of the Gaussian factor in the vertex Γ_μ was chosen to be $\Lambda = 1.8$ GeV. In Ref. [131], there were also two additional parameters associated with the vertex $\Gamma_{\mu\nu}$. They were adjusted to fit the inclusive cross sections for direct J/ψ production at transverse momenta up to 10 GeV that were measured by the CDF Collaboration. Following Lansberg et al., we set the center-of-mass energy of the colliding p and $\bar{p}$ to $\sqrt{s} = 1.8$ TeV and we use the MRST parton distributions at leading order [132]. We also impose a pseudo-rapidity cut $|\eta| < 0.6$ on the J/ψ. In Fig. 3.15, our result for the charm-pair rescattering (s–channel cut) contribution is compared to the results from Refs. [129] and [131]. Our result is reasonably close to that from Ref. [129] but much smaller than that from Ref. [131]. This suggests that the model for the vertex $\Gamma_{\mu\nu}$ used in Ref. [131] is unrealistic.

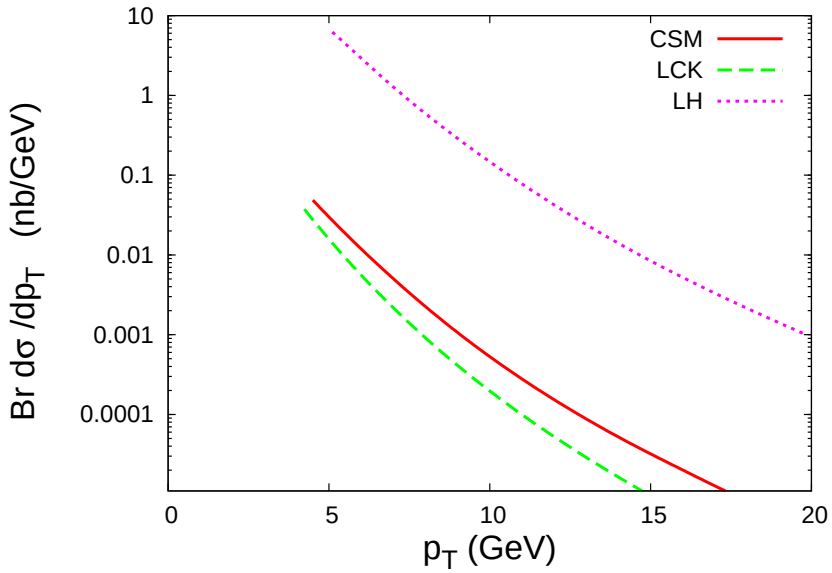

Figure 3.15: Differential cross section for inclusive J/ψ production at the Tevatron from charm-pair rescattering (s–channel cut). The differential cross section $d\sigma/dp_T$ integrated over the pseudorapidity interval $|\eta| < 0.6$ and multiplied by the branching fraction for $J/\psi \to \mu^+\mu^-$ is shown as a function of p_T. The solid line is our prediction in the CSM at α_s^5 accuracy. The dashed and dotted lines are the predictions calculated in the model of Lansberg, Cudell, and Kalinovsky in Ref. [129] and in the model of Lansberg and Haberzettl in Ref. [131], respectively.

We now proceed to assess the phenomenological importance of the contribution of the charm rescattering mechanism in the CSM. To this purpose, we consider the experimental data published by the CDF collaboration. In Fig 3.16 we plot the prompt differential cross section from [126] multiplied by the direct fraction measured in Ref. [115] and by the branching fraction $\mathrm{Br}[J/\psi \to \mu^+\mu^-] = 0.0588$. For a consistent comparison with these data, we set $\sqrt{s} = 1.96$ TeV and apply a rapidity cut $|y| < 0.6$. We set $m_c = 1.5$ GeV, which is natural as it close to half the mass of the J/ψ. We use the value of wave function at the origin derived from the Buchmüller and Tye potentiel [31], i.e. $\langle \mathcal{O}_{J/\psi}(^3S_1^{[1]}) \rangle = 1.16\ \mathrm{GeV}^3$. We also use a more recent set of parton distributions [125]. We stick to the choice $\mu = \sqrt{4m_c^2 + P_T^2}$ for the factorization and renormalization scales.

The resulting theoretical predictions are shown in Fig. 3.16. Together with the charm rescattering component (solid line), we plot the color-singlet differential cross sec-

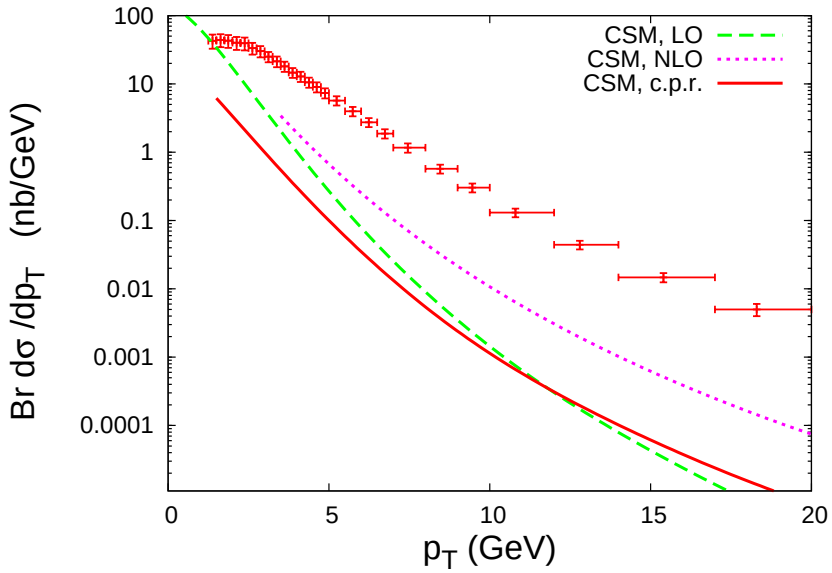

Figure 3.16: Color-singlet contributions to the differential cross section for inclusive J/ψ production at the Tevatron compared to data from the CDF collaboration [126, 115]. The differential cross section $d\sigma/dp_T$ integrated over the rapidity interval $|y| < 0.6$ and multiplied by the branching fraction for $J/\psi \to \mu^+\mu^-$ is shown as a function of p_T. The curves are the predictions of the color-singlet model at LO (dashed line), through NLO (dotted line), and at NNLO from charm-pair rescattering (solid line).

tions at leading order (dashed line) and next-to-leading order (dotted line) in α_s. The charm recattering component is a negligible contribution to the total color-singlet cross section. It is interesting to note, though, that the associated differential cross section shows a rather mild decrease in P_T, so that it dominates the leading order color-singlet distribution above $P_T = 12$ GeV (see Fig. 3.16). Still the charm rescattering contribution is subdominant in the whole P_T range compared to the color-singlet yield at NLO, and cannot be claimed to account for the dominant part of the cross section measured by the CDF collaboration.

3.3 J/ψ hadroproduction in association with a charm-quark pair

As was discussed in Section 3.2, higher-order corrections in α_s to the J/ψ hadroproduction open new channels, i.e. parton-level configurations that do not necessarily factorize over the Born-level topology. These contributions are relevant for the phenomenology, as they can be kinematically enhanced at large transverse momentum. At NLO in α_s, one particular manifestation of such contributions is in the production of a J/ψ in association with a pair of charm quarks. In this process, the charm quarks produced in addition to the J/ψ are expected to evolve most of the time into charm mesons. In order to identify the process experimentally, one needs to reconstruct at least one charm meson in addition to the J/ψ. As the associated production leads to a distinct signature, it can be measured and compared against the predictions of NRQCD. Hence, this more exclusive channel offers the opportunity to assess further the relevance of the factorization procedure for charmonium production.

Associated production has been studied in e^+e^- collisions, as we discussed in Section 3.1. The measurements by Belle and BABAR collaborations revealed an excess of events compared to the leading-order NRQCD predictions, suggesting that the perturbative expansion might not be well behaved, or that the non-factorisable color-transfer effect [50] might lead to an enhancement of the cross section. The analog situation in hadroproduction is not known, as there has been no experimental analysis of associated production in hadronic collisions so far. We argue in this section that such a measurement would provide valuable information on the mechanisms at work for J/ψ production. In particular, this signature could be used to probe the importance of the color-octet transitions. Along with the P_T spectrum and the polarization, the direction of flight of the charm mesons is also indicative of the transition at work, as we shall see in Section 3.3.2, and therefore provides additional observables to disentangle the various modes of production.

Distributions of events displayed within this section will be calculated at leading order in α_s, using our Monte Carlo generator MadOnia. We first produce samples of unweighted events, and then make use of the plotting interface MadAnalysis to draw the various distributions displayed below. One may fear that these leading-order predictions give an inaccurate description of the distributions of events, owing to the potentially large higher-order corrections. As we have seen in Section 3.2.1 the Born approximation for inclusive color-singlet production is not relevant to describe the way in which events populate the phase space, as the distribution of events is affected by large radiative corrections. For the associated production, though, the situation is different. Already the leading-order computation predicts that short-distance production takes place over distances of order $\frac{1}{m_Q}$. The amplitude at α_s^4 is therefore expected

to capture the important features in the distributions of events in a more accurate way than in the case of the inclusive production. Still, one has to keep in mind that large corrections may arise from higher-order-in-α_s corrections.

Associated production is a signature that could be studied during the first stage of the LHC. The muons originating from the J/ψ decay can be used to trigger the events. Reconstruction of the charm mesons could be achieved in the kaon+pion two-body and three-body decay modes by fitting the invariant mass distribution of the possible signatures, as has been done at the Tevatron in the case of the inclusive charm cross section [133]. Considering the startup conditions, we will assume that the center-of-mass energy of the proton-proton collisions is 10 TeV. Most of the angular distributions presented in the following sections can be applied to associated J/ψ production in $p\bar{p}$ collisions at 1.96 TeV, as the mechanisms at work are the same. Therefore, as far as the Tevatron is concerned, we only present the expected rates.

3.3.1 Production rates

As for the case of inclusive J/ψ production, direct associated production is dominated by gluon fusion at the LHC energy. We have checked that the light-quark-initiated process for $J/\psi + c\bar{c}$ production is suppressed by three orders of magnitude, and thus this contribution is neglected in the following.

In the present analysis we consider the following conditions:

- pp collisions at $\sqrt{s} = 10$ TeV;
- $\mu_0 = \sqrt{(4m_c)^2 + P_T^2}$;
- $m_c = 1.5$ GeV;
- pdf set: CTEQ6M [125].

The scale defined in this section differs from the choice adopted for inclusive production. It is bounded from below by $4m_c$, which is the minimal invariant mass in the final state. The color-singlet matrix element is extracted from the wave function related to the Buchmüller and Tye potential [31] For the octet case, the long-distance matrix elements must be fitted from experimental data. Here we use the values extracted at the Tevatron. As was first emphasized in [65], the short distance coefficients $\hat{\sigma}(p\bar{p} \to c\bar{c}\left({}^3P_J^{[8]}\right) + X)$ and $\hat{\sigma}(p\bar{p} \to c\bar{c}\left({}^1S_0^{[8]}\right) + X)$ at order α_s^3 lead to a similar slope for the cross section differential in $P_T(J/\psi)$ at middle-large transverse momentum. As a result, the predicted yield associated with these two transitions at the

$\langle O_1(^3S_1)\rangle_{J/\psi}$	$\langle O_8(^3S_1)\rangle_{J/\psi}$	$\langle O_8(^1S_0)\rangle_{J/\psi}$	$\langle O_8(^3P_0)\rangle_{J/\psi}/m_c^2$
116	0.39	1.5	1.5

Table 3.1: Values of the long-distance matrix elements considered for the associated production, in $10^{-2}\times$ GeV^3.

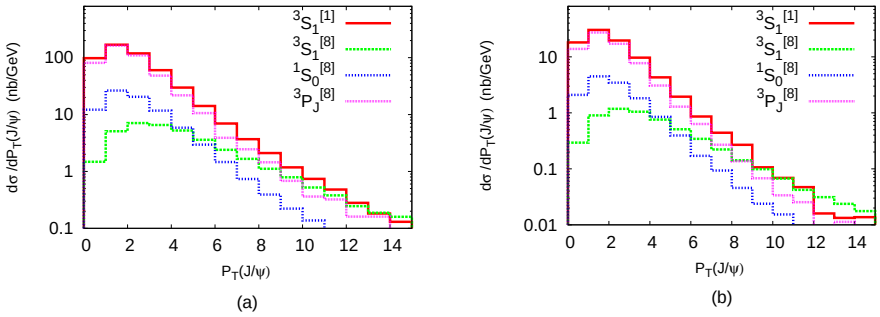

Figure 3.17: Cross sections differential in the transverse momentum of the J/ψ (a) for the process $pp \to J/\psi + c\bar{c}$ at the LHC, $\sqrt{s} = 10$ TeV, (b) for the process $p\bar{p} \to J/\psi + c\bar{c}$ at the Tevatron, $\sqrt{s} = 1.96$ TeV.

Tevatron is only sensitive to the combination

$$\langle O_8(^1S_0)\rangle_{J/\psi} + k\frac{\langle O_8(^3P_0)\rangle_{J/\psi}}{m_c^2}, \tag{3.14}$$

with the parameter k close to 3 above $P_T > 5$ GeV. Several fits have been performed to extract the values of the color-octet LDME's [13]. The results are rather strongly dependent on the assumptions of the fit. In this section, we decide to stick to the values obtained in [119]:

$$\langle O_8(^3S_1)\rangle_{J/\psi} = 0.39\,10^{-2}\text{ GeV}^3, \quad \langle O_8(^1S_0)\rangle_{J/\psi} + k\frac{\langle O_8(^3P_0)\rangle_{J/\psi}}{m_c^2} = 6.6\,10^{-2}\text{ GeV}^3 \tag{3.15}$$

with $k = 3.4$. We note that these values are close to the recent result of the fit in [134], where the authors used the NLO computations of order α_s^4 for the short-distance cross sections $\hat{\sigma}(p\bar{p} \to c\bar{c}\left(^3S_1^{[8]}\right) + X)$ and $\hat{\sigma}(p\bar{p} \to c\bar{c}\left(^1S_0^{[8]}\right)) + X$, and set the parameter k in Eq. (3.14) to zero.

Although the inclusive cross sections associated with the transitions $^1S_0^{[8]}$ and $^3P_J^{[8]}$ share the same properties for the P_T spectrum in hadron collisions, some observables

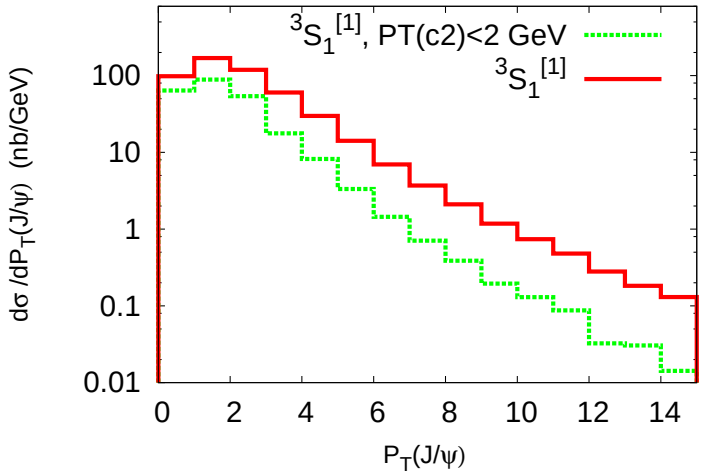

Figure 3.18: Comparison between the full color-singlet yield (in red) and the partial contribution from phase-space regions in which at least one charm quark is soft (in green). The notation $c2$ refers to the charm quark with the lowest transverse momentum.

may have a different behavior for these transitions (the polarization of the J/ψ is an example). For these observables, it is mandatory to assign a specific value to each of the two long distance matrix elements appearing in Eq. (3.14). Here we will make the arbitrary assumption

$$\langle O_8(^1S_0)\rangle_{J/\psi} = \frac{\langle O_8(^3P_0)\rangle_{J/\psi}}{m_c^2}. \tag{3.16}$$

The resulting values of the various LDME's are summarized in Table 3.3.1.

In Fig. 3.17 we show the P_T distributions for both the singlet and the octet channels, without any restriction on the pseudo-rapidity range. For comparison, we also plot the analogous distributions expected at the Tevatron. For the color-singlet case, we note that the P_T distribution peaks at $P_T \simeq m_c$ and then it starts a quick decrease, dropping by two orders of magnitude at $P_T \simeq 15$ GeV. We verified that the topologies in which the J/ψ is produced by two different quark lines always dominate. This behaviour is similar to J/ψ production at e^+e^- colliders, where the presence of two extra charm mesons seems to result in the J/ψ being created most often from two different quark lines as well. We also checked that contributions in which at least one charm quark is soft are subdominant at large P_T, as illustrated in Fig. 3.18. Such

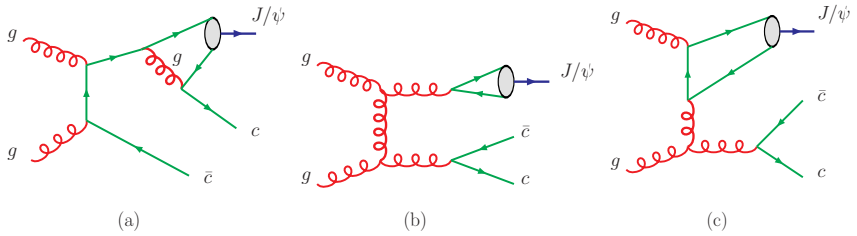

Figure 3.19: Typical Feynman diagrams for the associated-production process $gg \to c\bar{c}J/\psi$ via (a) a color-singlet ${}^3S_1$ transition, (b) a color-octet ${}^3S_1$ transition, (c) a color-octet ${}^1S_0$ or ${}^3P_J$ transition.

contributions have been partially considered through the study of the c-quark-initiated process $cg \to cJ/\psi$. Indeed, in this process, the initial charm quark originates from the splitting of a gluon into a pair of charm quarks collinear to the beam. One of the quarks interacts with a gluon to produce the J/ψ; the other quark is lost in the beam pipe. The comparison displayed in Fig. 3.18 shows that the yield associated with these contributions drops faster in P_T than the total yield. This is expected, since the presence of the two propagators in the c-quark-initiated process disfavors this mechanism at large P_T, compared to fragmentation contributions.

In contrast to the situation in e^+e^- collisions [110], in associated J/ψ hadroproduction the color-octet transitions play an important role. Although negligible at small P_T, the ${}^3S_1^{[8]}$ transition starts to compete with the color-singlet transition at $P_T \approx 12$ GeV, and dominates the associated production at larger values of the J/ψ transverse momentum. The ${}^3S_1^{[8]}$ cross section, integrated over the whole P_T range, remains small compared to the color-singlet one. The preponderance of the ${}^3S_1^{[8]}$ transition at large P_T is due to the kinematically-enhanced channel

$$gg \to c\bar{c}g^*, \quad g^* \to cc\,({}^3S_1^{[8]}), \tag{3.17}$$

where the J/ψ is produced via the fragmentation of a nearly on-shell gluon (see diagram (b) of Fig. 3.19). In this fragmentation topology, the partonic subprocess behaves as $\frac{1}{P_T^4}$. The fragmentation of a gluon into a J/ψ is not allowed in the case of the order-α_s^4 color-singlet production, which is therefore sub-dominant at large transverse momentum. The color-singlet fragmentation of a charm-quark into a J/ψ (see diagram (a) of Fig. 3.19) also behaves as $\frac{1}{P_T^4}$. However, in this case, the invariant mass of the products of the fragmentation is larger than in the case of the gluon fragmentation. Charm-quark fragmentation is therefore expected to be kinematically suppressed at large P_T compared to gluon fragmentation, as it is confirmed by the P_T spectrum in Fig. 3.17.

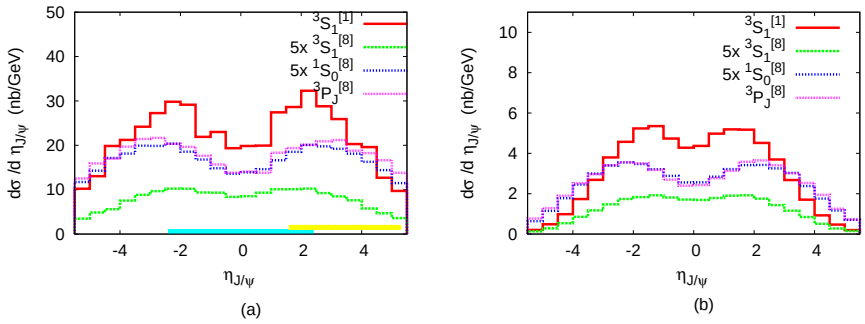

Figure 3.20: Cross sections differential in the pseudo-rapidity of the J/ψ (a) for the process $pp \to J/\psi + c\bar{c}$ at the LHC, $\sqrt{s} = 10$ TeV, (b) for the process $pp \to J/\psi + c\bar{c}$ at the Tevatron, $\sqrt{s} = 1.96$ TeV.

The color-octet ${}^1S_0$ and ${}^3P_J$ transitions have the same P_T shape as the color-singlet production, indicating that the cross section differential in P_T is an observable of limited power to disentangle the transitions at work. We have checked that the total cross sections $\sigma(c\bar{c}c\bar{c}({}^1S_0^{[8]}))$ and $\sigma(c\bar{c}c\bar{c}({}^3P_J^{[8]}))$ are dominated by topologies with gluon exchange in the t-channel, as is illustrated in Fig. 3.19, diagram (c). The ratio of the corresponding differential cross sections shows a similar behavior to that in the case of the inclusive production [65]: it decreases slightly in P_T to reach the asymptotic value ≈ 3.

The pseudo-rapidity distributions resulting from the various transitions are shown in Fig. 3.20 for the cut $P_T(J/\psi) > 1$ GeV. For comparison, we also plot the analogous distributions expected at the Tevatron. The yellow line on the x axis indicates the solid angle covered by the LHCb experiment, whereas the cyan line corresponds to the region in which the muons are reconstructed in the CMS and ATLAS detectors. We do not quote the exact rate of events in the two experiments, as it is very much dependent on the acceptance cut and the reconstruction algorithm.

As is mentioned in Section 3.2, J/ψ events can originate from the decay of higher-energy resonances. This contribution has not been taken in the predictions made so far, and so we come back to this point now. The non-prompt fraction can be disentangled experimentally by making use of a vertex separation criterion, so that we do not need to bother ourselves with this contribution. The possibility to identify the feed-down from χ_c states has been investigated by the ATLAS collaboration in the case of the inclusive production, but this analysis is rather intricate. For this reason, we briefly comment on this contribution for the case of associated production. Among the charmonium P-wave states, only the χ_{c1} and the χ_{c2} have a large probability to

decay into the J/ψ through an $E1$ transition:

$$Br(\chi_{c1} \to J/\psi\gamma) = 36\%, \quad Br(\chi_{c2} \to J/\psi\gamma) = 20\%. \tag{3.18}$$

We first consider the color-singlet contribution, with the long-distance matrix element derived from the Buchmüller-Tye potential [31]:

$$\langle O_1(^3P_J)\rangle_{\chi_{cJ}} = (2J+1) \times 0.1074\,\text{GeV}. \tag{3.19}$$

We have checked that the P_T spectrum for $pp \to \chi_{cJ} c\bar{c}$ has a similar shape as the color-singlet yield $pp \to J/\psi + c\bar{c}$ above 4 GeV, but is suppressed by a factor ≈ 1.7 for the case $J = 1$ and a factor ≈ 2.5 for the case $J = 2$. Taking into account the branching ratios in Eq. (3.18), feed-down from color-singlet χ_c states is about $\approx 30\%$ of the direct color-singlet contribution at middle-large P_T. At leading order in v, χ_c states can also be produced via a $^3S_1^{[8]}$ intermediate state. In first approximation, the related feed-down contributes through a rescaling of the spectrum associated with the direct yield via the $^3S_1^{[8]}$ transition by a factor

$$\sum_J \frac{\langle \mathcal{O}_8\left(^3S_1\right)\rangle_{\chi_{cJ}}}{\langle \mathcal{O}_8\left(^3S_1\right)\rangle_{J/\psi}} \text{Br}(\chi_{cJ} \to \gamma J/\psi). \tag{3.20}$$

3.3.2 Identifying the transitions at work

As we mentioned in the previous section, the measurement of the P_T spectrum of the J/ψ in the process $pp \to c\bar{c}J/\psi$ would not provide enough information to identify unambiguously the transition at work. Other observables, with distinct behaviors for the different transitions, are required to test the universality of the LDME's.

One such observable is the angular distribution of the muons, or equivalently the polarization of the J/ψ. Here we consider the polarization parameters λ and ν (see section 2.2) for the helicity spin quantization axis. As we can see in Fig. 3.21, these parameters reveal different features for the various transitions. Whereas the J/ψ produced via a color-singlet transition is unpolarized independently of the value of its transverse momentum, the transverse polarization state dominates the color-octet $^3S_1$ transition above $P_T = 5$ GeV. This feature is to be related to the polarization studies for the α_s^3 inclusive color-octet J/ψ production, which is also rapidly dominated by gluon fragmentation at large P_T. J/ψ's produced via a color-octet ^3P_J transition are strongly polarized at low P_T, as it can be seen by examining the azimuthal distribution of the muons with respect to the J/ψ momentum (controlled by the ν parameter). A more clever orientation of the spin-quantization axis could be used to maximize the polar asymmetry —see e.g. the analysis in [135] for the inclusive J/ψ production— which

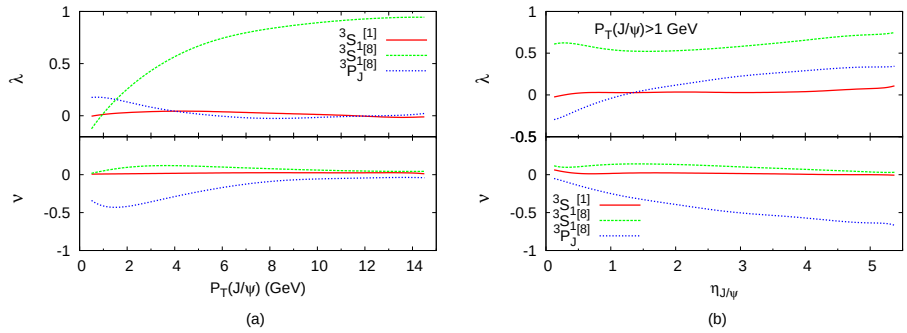

Figure 3.21: Polarization parameters for J/ψ hadroproduction in association with a charm quark pair, as a function of the transverse momentum of the J/ψ (a), and the pseudo-rapidity of the J/ψ (b).

would lead to the measurement only of the λ parameter, but we do not perform this analysis here. We do not display the expected values of the polarization parameters for the color-octet $^1S_0$ transition, as in this case the distribution of the muons in the J/ψ rest frame is trivially uniform.

The presence of charm mesons in the final state also offer to opportunity to define new observables that help us in identifying the relative importance of the different transitions. The measurement of the transverse momentum of charm mesons is in general a delicate operation, especially if they are reconstructed through leptonic decay channels. The direction of flight of the charm mesons is often measured with a much better

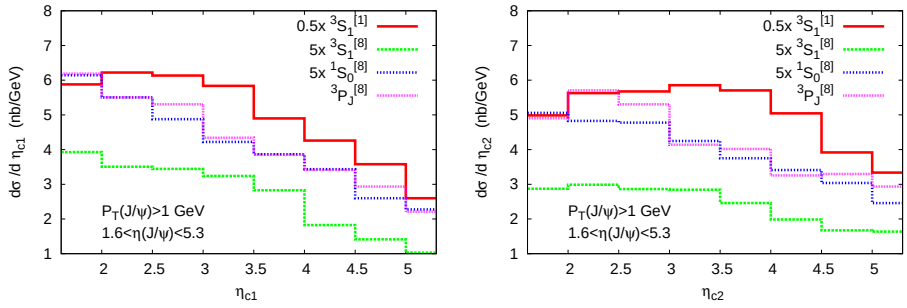

Figure 3.22: Pseudo-rapidity distributions of the charm quarks produced in association with a J/ψ in the LHCb acceptance region.

accuracy. For this reason, we will stick to observables that can be constructed from only the polar and azimuthal angles of the charm mesons. We assume that the direction of the charm meson and the direction of the charm quark from which it originates are the same. Energies of charm quarks are integrated over in the following prediction, but we order the two charm quarks in P_T: we denote by "c1" the charm quark with the higher transverse momentum and by "c2" the charm quark with the lower transverse momentum. We also consider two different regions of the phase space:

- the low P_T and forward region (called region I below)

$$P_T(J/\psi \gtrsim 1\,\text{GeV}), \quad 1.6 < \eta(J/\psi) < 5.3 \tag{3.21}$$

  which is relevant for the LHCb detector,

- the high P_T and central region (called region II below)

$$P_T(J/\psi > 10\,\text{GeV}), \quad |\eta(J/\psi)| < 2.4 \tag{3.22}$$

  which is relevant for the ATLAS and CMS detectors.

We start with the region I. In Fig. 3.22 we plot the pseudo-rapidity distributions of the charm quarks in the region of LHCb acceptance. The various transitions have been rescaled. As expected, the ${}^3S_1^{[8]}$ transition is subdominant. The yield associated with the ${}^1S_0^{[8]}$ and ${}^3P_J^{[8]}$ transitions shows the same linear decrease in pseudo-rapidity, and so the pseudo-rapidity distributions do not resolve these transitions separately. The sum of their contributions competes with the color-singlet yield, for which the charm-quark distribution in pseudo-rapidity has a different shape. Whether this difference is sufficient to measure the relative weight between the singlet and octet contributions is not clear, as it depends on the resolution in the angles of the reconstructed mesons and on the way in which the distributions for charm quarks displayed in Fig. 3.22 deviate from those for charm mesons.

We now turn to region II. We show the angular separation $\Delta_R = \sqrt{\Delta\phi^2 + \Delta\eta^2}$ between the J/ψ and the charm quarks in Fig. 3.23. As expected, the hardest charm quark is emitted in the opposite direction from the J/ψ. We note that the decrease above $\Delta_R \approx 3$ is different for the singlet and octet contributions. More significantly, the mean angular separation between the J/ψ and the softest charm quark is substantially lower in the case of the color-singlet transition, as is illustrated in the second distribution of Fig. 3.23. Also, the angular separation between the two charm quarks in the case of the singlet transition is marginally different from the distribution associated with the other transitions. We may obtain an intuitive explanation of these features by looking at the topologies in Fig. 3.19. In the case of the color-singlet transition, neither the gluon fragmentation channel (diagram b) nor the t-channel gluon

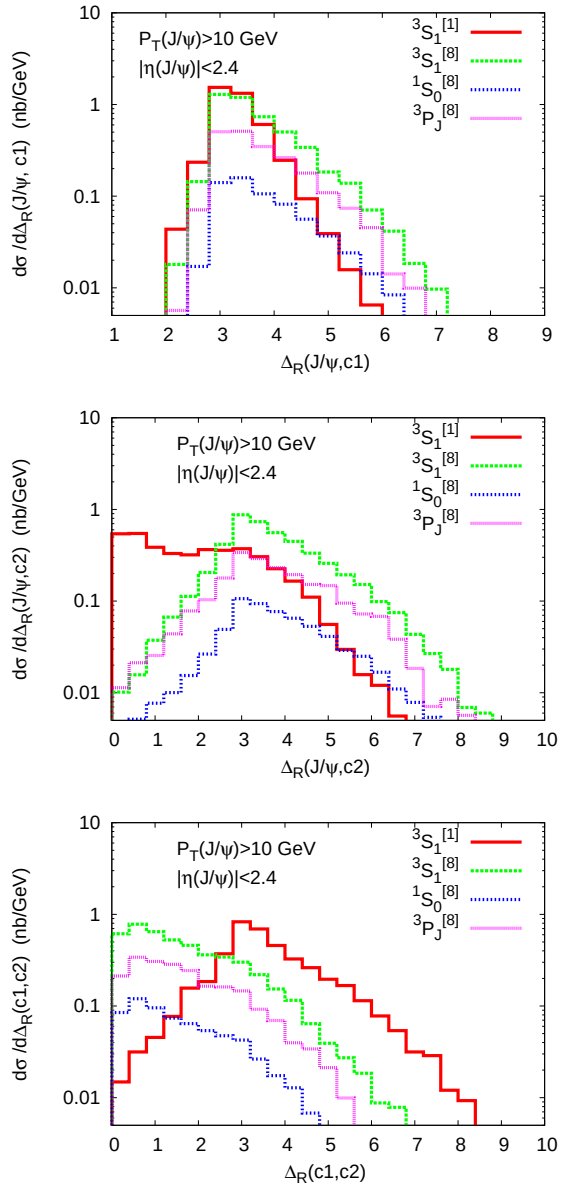

Figure 3.23: Δ_R distributions for the associated production process $J/\psi + c\bar{c}$ in hadron collisions at large transverse momentum.

exchange (diagram c) contribute. Since in these topologies, both quarks are expected to be emitted in the recoil direction of the J/ψ, this explains the trends of the angular distributions of the charm quarks.

3.4 J/ψ photoproduction

We now move on to J/ψ photoproduction at HERA, which has been measured by both the ZEUS and the H1 collaborations [136, 137].

3.4.1 Tree-level mechanisms

The relevant kinematic variables for J/ψ photoproduction are the energy of the photon-proton system (W) and the fraction of the photon energy carried by the J/ψ in the proton rest frame (z),

$$W = \sqrt{(p_\gamma + p_p)^2}, \quad z = \frac{p_\psi . p_p}{p_\gamma . p_p} \,, \tag{3.23}$$

as well as the transverse momentum of the J/ψ (P_T). Near the end-point region $z \approx 1$, $P_T \approx 0$ GeV, J/ψ production is enhanced by diffractive contributions characterized by the exchange of colorless states. These contributions cannot be correctly accounted for by the NRQCD factorization scheme, and hence they must be excluded from experimental measurements in order to make a meaningful comparison with predictions from perturbative QCD. As the diffractive production leads to a steeper slope for the P_T spectrum of the J/ψ, the cut $P_T > 1$ GeV eliminates most of the diffractive events. Whether this cut is enough to select a clean sample of inelastic events is still a subject of experimental investigation[138].

Already at tree-level, J/ψ production from the photon-proton interaction can proceed through different mechanisms. These mechanisms contribute in different phase-space regions, as we review here. We set $m_c = 1.5$ GeV and choose $\mu_r = \mu_f = 2m_c$. For the long-distance matrix elements, we use the same values as in Section 3.3. For each initiated parton state, we also give the integrated cross section $\sigma(P_T > 1 \text{ GeV})$. However one should keep in mind that NRQCD factorization likely holds only for $P_T \gg m_Q$. So the use of NRQCD factorization probably cannot be justified for the computation of these total cross sections, which are dominated by the low P_T region.

In the *direct* mechanisms, the photon interacts directly with a parton originating from the proton over distances of order $\frac{1}{m_c}$ or less. At leading order in v —the relative velocity in the J/ψ— the charm-quark pair has to reach a color-singlet state over short distances, which requires two gluons to connect the charm quark line, in addition to the photon. The corresponding mechanism is depicted in Fig. 3.24, (a). At order $\alpha\alpha_s^2$, there are six Feynman diagrams, related by the permutation of the gauge bosons. This born-level contribution to the color-singlet transition is finite over the whole J/ψ phase-space, and leads to a rather flat distribution in energy (see Fig. 3.25,

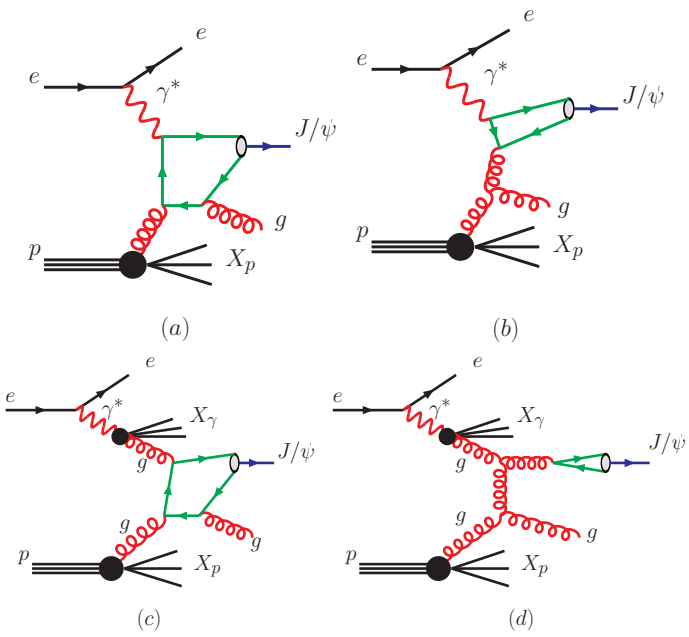

Figure 3.24: Tree-level contribution to J/ψ photoproduction.

(a)). At relative-order v^4, J/ψ production can proceed through an intermediate state ${}^1S_0^{[8]}$ or ${}^3P_J^{[8]}$. Each of these states can be reached by attaching a gluon and a photon to the charm-quark line. This leads to an order-$\alpha\alpha_s$ contribution to the production of a J/ψ at zero transverse momentum. Away from $P_T = 0$, the production involves the emission of a gluon, which balances the transverse momentum of the J/ψ. A typical Feynman diagram for this $\alpha\alpha_s^2$ contribution is illustrated in Fig. 3.24 (b). Since this is a higher-order contribution, the associated tree-level computation develops an infrared singularity when the transverse momentum of the final gluon goes to zero. Experimentally, the low-P_T region is cut off in order to get rid of the diffractive contributions. If we apply the same cut in the prediction, then the phase-space integration leads to a finite contribution. The z distribution for $P_T > 1$ GeV is displayed in Fig. 3.25, (b). The peak at $z = 1$ clearly signals that the perturbation expansion breaks down and that resummation of soft gluon emission is required [139].

The production can also proceeds via an intermediate state ${}^3S_1^{[8]}$. Such a state can be reached in the diagram displayed in Fig. 3.24 (a), which leads to a z distribution that is suppressed by the ratio of the long distance matrix elements $\langle \mathcal{O}_{J/\psi}\left({}^3S_1^{[8]}\right)\rangle / \langle \mathcal{O}_{J/\psi}\left({}^3S_1^{[1]}\right)\rangle$. Another possibility comes from the interaction of the photon with a light quark originating from the proton. This quark-initiated fragmentation contribution is only com-

transition\initial state	γg	γu	$\gamma \bar{u}$	γd	$\gamma \bar{d}$
${}^3P_1^8$	207	14.2	4.6	12.2	7.7
${}^1S_0^{[8]}$	36.9	2.4	0.8	2.1	1.3
${}^3S_1^{[8]}$	0.1	0.01	0.006	0.003	0.003

Table 3.2: Total cross section $\sigma(P_T > 1\ \text{GeV})$ in nb for the direct color-octet components. d stands for a down or strange quark. W is set to 100 GeV.

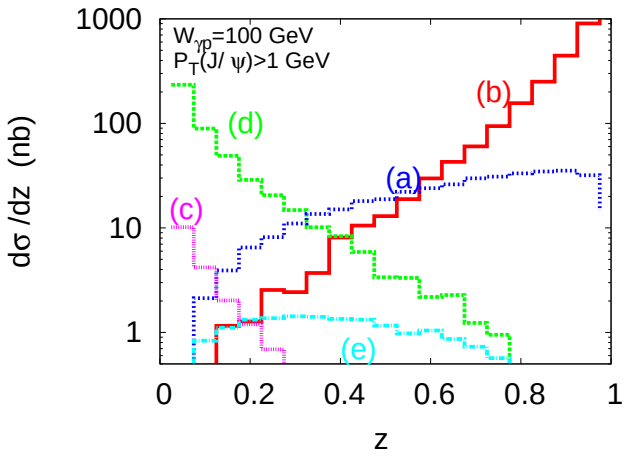

Figure 3.25: Tree-level contributions to the cross section differential in z: (a) color-singlet direct, (b) color-octet direct, (c) color-singlet resolved, (d) color-octet resolved, (e) direct color-singlet associated production.

petitive at high transverse momentum. The direct color-octet contributions are summarized in Table 3.2.

So far, we have only considered the *direct* processes, in which the photon directly connects to a parton with a large virtuality. Alternatively, the photon can fragment into a pair of on-shell collinear light quarks, one of them interacting with the proton. The splitting $\gamma(p) \to q(xp)$ cannot be described perturbatively and requires the convolution with a non-pertubative distribution $f_{q/\gamma}(x, Q)$ [140]. As the collinear quarks originating from the photon have a certain probability to hadronize into a vector-like light hadron, which is a source of gluons, one also introduces the distribution $f_{g/\gamma}(x, Q)$ which corresponds to the splitting $\gamma(p) \to g(xp)$. These mechanisms are classified as *resolved-photon* contributions, and lead to other processes of J/ψ production. At

transition\initial partons	qg	$\bar{q}g$	gg	gq	$g\bar{q}$	$\bar{q}q$	$q\bar{q}$
${}^3P_1^8$	64.3	64.3	6.3	0.9	0.2	0.08	0.08
${}^1S_0^{[8]}$	12.0	12.0	1.17	0.18	0.04	0.008	0.008
${}^3S_1^{[8]}$	17.5	17.5	0.8	0.2	0.04	0.3	0.3

Table 3.3: Total cross section $\sigma(P_T > 1 \text{ GeV})$ in nb for the resolved color-octet components. q stands for a light quark u, d or s. W is set to 100 GeV.

leading order in α_s, color-singlet resolved production is initiated by two gluons, as displayed in Fig. 3.24, (c). For color-octet production, the resolved component opens several new contributions, initiated by quarks or gluons. One important new channel is color-octet gluon fragmentation, $g \to c\bar{c}\left({}^3S_1^{[8]}\right)$, which is displayed in Fig. 3.24, (d).

Resolved contributions are relevant only in the low z region, as the fragmentation of a photon into an energetic parton is very rare. As can be seen in Fig. 3.25, the resolved color-singlet contribution is negligible for $z \gtrsim 0.2$. The resolved color-octet component gives a more substantial contribution, but is nevertheless significant only for $z \lesssim 0.4$.

Inelastic contributions to J/ψ production also include the feed-down from excited charmonium states, which we do not take into account here. Feed-down from the $\psi(2S)$ is seen to lead to a 15% increase in the J/ψ cross section [136], whereas contributions from the χ_c states are expected to be smaller ($\approx 1\%$).

3.4.2 Color-singlet observables at Next-to-Leading Order in α_s

The cross section $\sigma(\gamma p \to J/\psi + X)$ in the color-singlet model has been computed in [141] at NLO accuracy in α_S. We reproduced this computation by using the method and the results presented in [91] for the hadro-production case, which also allows us to keep track of the J/ψ polarization through the angular correlations of the J/ψ decay products, $J/\psi \to \ell^+\ell^-$. We have compared the results of the two calculations for several inclusive observables, finding very good agreement.

The ZEUS collaboration has published a measurement of the differential cross sections for J/ψ photoproduction produced from electron-proton collisions, with $E_p =$

$\mu_r \backslash \mu_f$	$0.5\mu_0$	μ_0	$2\mu_0$
$2\mu_0$	8.07	9.67	10.6
μ_0	9.45	10.2	10.3
$0.5\mu_0$	10.6	8.28	5.96

Table 3.4: Scale dependence of the total cross section $\sigma(P_T > 1GeV)$ (expressed in nb). W is set to 100 GeV. Other input parameters are explained in the text.

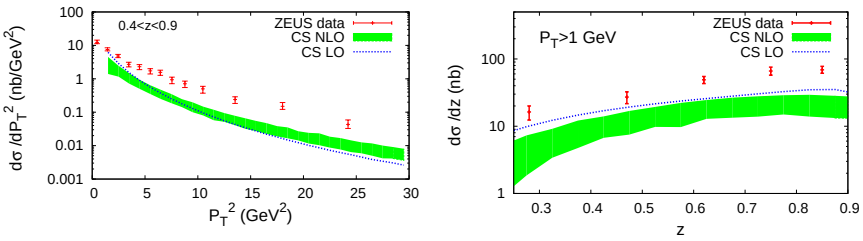

Figure 3.26: Differential cross sections with respect to P_T^2 (a) and to z (b), compared with the ZEUS data [136].

820 GeV and $E_e = 27.5$ GeV [136]. In their analysis, they consider the range 50 GeV $< W <$ 180 GeV, and convert electro-production cross sections into photo-production cross sections by dividing by the photon flux integrated in this range. This is estimated within the Weizsäcker-Williams approximation: using $Q^{max} = 1$ GeV, they obtain $F_{\text{photon}} = 0.0987$. For a consistent comparison with this measurement, our $\gamma - p$ cross sections are convoluted with the photon flux, using the Weizsäcker-Williams approximation, and then divided by the integrated flux quoted above.

In our photoproduction analysis, we fix $\langle \mathcal{O}_{J/\psi}(^3S_1[1]) \rangle = 1.16$ GeV^3 and we use the CTEQ6M pdf set [125]. As the experimental P_T is not really large, we prefer to use a fixed scale. In order to estimate the scale uncertainty, we set $\mu_0 = 4m_c$ with $m_c = 1.5$ GeV, and then vary the factorization and renormalization scales between $\frac{\mu_0}{2}$ and $2\mu_0$ under the condition $0.5 < \frac{\mu_f}{\mu_r} < 2$. We note that this range covers the more physical choice $\mu_{r,f} = \sqrt{4m_c^2 + P_T^2}$. The scale dependence of the total cross section $\sigma(P_T > 1$ GeV$)$ is displayed in Table 3.4. In our prediction for the differential cross sections, we also vary the charm-quark mass in the range $1.4 - 1.6$ GeV. Scale and mass uncertainties are combined in quadrature. The resulting distributions in P_T and z are displayed in Fig. 3.26.

For comparison, we also plot the color-singlet prediction at leading order in α_S, for which we use the CTEQ6L1 pdf set. As can be seen from Fig. 3.26, the α_S corrections

increase the differential cross section in the high P_T region, where the yield is dominated by the new channels that open up at order α_S^3. Nevertheless, the color-singlet yield at NLO clearly undershoots the ZEUS data. The plots in Fig. 3.26 differ from the comparison presented in [136], where rather extreme values for the renormalization scale were used that have the effect of artificially increasing the normalization. We do not display here the comparison with the P_T^2 and z distributions measured by the H1 collaboration [137] since it shares the same features.

We now turn to the polarization. Experimentally, the polarization of the J/ψ's can be determined by analyzing the angular distribution of the leptons originating from the decay of the J/ψ. As we have seen in Section 2.2, it is convenient to decompose this angular distribution in terms of the polar and azimuthal angles θ and ϕ in the J/ψ rest frame:

$$\begin{aligned}\frac{d\sigma}{d\Omega dy} \quad &\propto \quad 1+\lambda(y)\cos^2\theta+\mu(y)\sin 2\theta\cos\phi \\ &\quad +\frac{\nu(y)}{2}\sin^2\theta\cos 2\phi \end{aligned} \tag{3.24}$$

where y stands for a certain (set of) variable(s) (either P_T or z in the following). If the polar axis coincides with the spin quantization axis, the parameters λ, μ, ν can be related to the spin density matrix elements (see Section 2.2).

The spin information that we extract in this way depends on the choice of the quantization axis. Here, we decide to work in the target frame ($\hat{\boldsymbol{z}} = -\frac{\boldsymbol{p}_{\rm p}}{|\boldsymbol{p}_{\rm p}|}$) as this frame has been chosen in the recent analysis performed by the ZEUS collaboration.

As we have mentioned above, in our NLO computation the J/ψ decays into leptons, in order to extract λ (resp. ν), we have integrated the cross sections over ϕ (resp. θ) and extracted the polarization parameters by fitting the resulting distributions. In so doing, we have used the same cuts as those considered by the ZEUS collaboration: $E_p = 920$ GeV, $E_e = 27.5$ GeV, $P_T > 1$ GeV, $z > 0.4$ and $\quad 50\text{ GeV} < W < 180\text{ GeV}$. Notice that the cut $z < 0.9$ previously considered for the differential cross sections has been relaxed here. The measurement of the polarization versus P_T is therefore subject to a larger contamination from diffractive contributions.

The NLO predictions of the polarization parameters associated with color-singlet production are displayed in Fig. 3.27, together with the LO predictions and the recent ZEUS measurements [142]. The band comes from the uncertainties associated with the choice of the scales —varied between $\frac{\mu_0}{2}$ and $2\mu_0$— which appeared to be much larger then the mass uncertainty. For some specific values of the scales (namely $\mu_r = 0.5$), the λ and ν parameters appear to be unphysical in some bins. This is due to the fact that, under certain conditions for the scales, our calculation leads to a

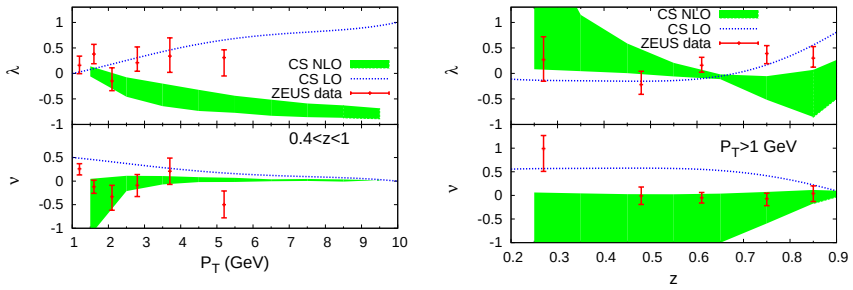

Figure 3.27: Polarization parameters for color-singlet production at leading order and next-to-leading order in α_S, compared with the ZEUS measurement [142].

negative value for the diagonal components of the spin density matrix at $P_T \approx 1$ GeV, and hence cannot be trusted anymore in this region.

QCD corrections to color-singlet production have a strong impact on the polarization prediction. The most spectacular effect comes from the behavior of the λ parameter at large transverse momentum, for which the prediction is rather stable under the variation of the scales. At leading order in α_S, the color-singlet transition gives a transverse polarization for the J/ψ at large P_T. Including QCD corrections, we see that the λ parameter decreases rapidly and has a large negative value above $P_T = 4 - 5$ GeV. This situation is similar to what happens in hadro-production, where the J/ψ produced via a color-singlet transition is longitudinal at large transverse momentum. Such a correction for the λ parameter at moderate and high P_T, as well as the decrease at $z \approx 0.8$, is not supported by the data from the ZEUS collaboration, suggesting the presence of other mechanisms for J/ψ production. In the low z region, the scale uncertainty is too large to draw any conclusion. QCD corrections to color-singlet production also affect the value of the ν parameter, which goes closer to the experimental data in comparison with the prediction at leading order.

Discussion

For several years, it has been believed that the color-singlet contribution alone explains measurements of J/ψ photoproduction cross sections. However, as we have shown in the previous section, even when we take into account the order-α_S corrections, color-singlet production alone does not describe all features of the data collected at HERA. With a natural choice for the renormalization scale, the predicted rate is smaller than the data, even though the shapes of the differential distributions are well described.

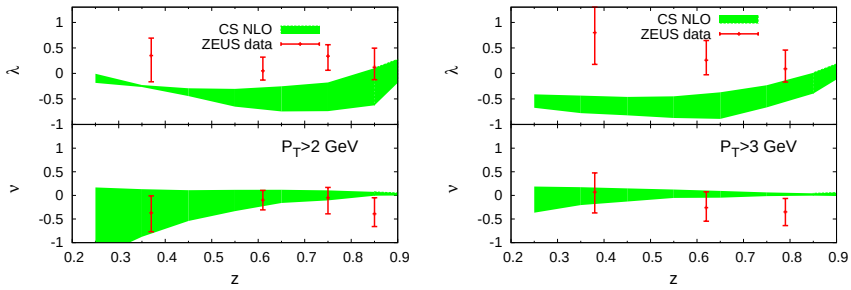

Figure 3.28: Distribution of the polarization parameters for color-singlet production at leading order and next-to-leading order in α_S, as a function of z for the regions $P_T > 2$ GeV and $P_T > 3$ GeV.

Moreover, the recent measurement of the J/ψ polarization by the ZEUS collaboration as a function of the P_T shows a very different trend than the theoretical predictions. As we have already stressed, the NLO prediction of the polarization parameters is not well behaved in the region $P_T \approx 1$ GeV, as some of the diagonal entries of the spin density matrix become negative in this region. As is illustrated in Fig. 3.28, the scale uncertainty is substantially reduced by imposing a more stringent cut $P_T > 2$ GeV or even $P_T > 3$. The corresponding ZEUS data points for the λ parameter are systematically higher than the color-singlet prediction, the discrepancy being of the order of one σ.

New channels appearing at NNLO in α_S (including fragmentation processes) may increase the differential cross section, as we have pointed out in the hadroproduction case. Although the kinematics differ in photoproduction, such contributions could give an enhancement at large transverse momentum ($P_T > 5$ GeV). However, no reliable estimate of NNLO contributions in the P_T region accessible at HERA is presently available.

The current discrepancies could possibly be solved by invoking color-octet transitions, i.e. contributions from the intermediate states ${}^1S_0^{[8]}$ and ${}^3P_J^{[8]}$. Unfortunately, any phenomenological analysis of the impact of these contributions on differential cross sections and polarization observables is limited by the omission of higher-order corrections that are currently unknown. A complete α_S^3 computation, particularly for the prediction of the polarization of the J/ψ produced via a $P-$wave color-octet state, would be welcome in order to shed further light on the mechanisms at work in photoproduction.

Conclusion

In this thesis, we have presented several new results for quarkonium production in e^+e^- annihilation at B-factories, in hadron collisions at the Tevatron and the LHC colliders, and in photoproduction at HERA. They can be schematically summarized as follows:

- We have analysed the relativistic correction to J/ψ production through a color-singlet transition in e^+e^- annihilation. After having cross-checked the computation of the v^2 correction to the exclusive production process $e^+e^- \to J/\psi+\eta_c$ we have presented an original result for the complete v^2 correction to $e^+e^- \to J/\psi + c\bar{c}$, including the relativistic expansion of the phase-space, and found that the overal correction is small. We also showed that corrections to the wave function of higher order in v are small, and can be safely neglected. We argued that analogous corrections to $e^+e^- \to J/\psi gg$ are also small. The inclusive color-singlet J/ψ yield in e^+e^- annihilation is therefore largely dominated by the leading term in the v expansion.

- We have combined our results for the real polarized quarkonium amplitudes with the external computation of the one-loop amplitude for $gg \to c\bar{c}(^3S_1^{[1]})+g$ or $g\gamma \to c\bar{c}(^3S_1^{[1]}) + g$ [91], to derive at NLO accuracy the polarization of the J/ψ produced via a color-singlet transition in photon-proton and hadron-hadron collisions. In the later case, we also gave the corresponding results for the Υ. We showed that radiative corrections change dramatically the prediction for the polarization.

- Starting from previous observations that new important topologies for the color-singlet hadroproduction of spin-triplet S-wave states arise at order α_s^5 —such as the gluon fragmentation channel or the t-channel gluon exchange, which is approximated in the k_t factorization approach—, we estimated the impact of the

channels $pp \to Q\bar{Q}(^3S_1^{[1]}) + 3$ light partons. In the case of the Υ, we argued that such channels can fill the gap between the color-singlet yield and the data collected by the CDF collaboration.

- We have presented the computation of the α_s^5 s-channel cut contributions to inclusive J/ψ hadroproduction via a color-singlet transition. Whereas previous phenomenological models [129, 131] have a number of free parameters and hence suffer from a large theoretical uncertainties, such contributions arise naturally at order α_s^5 in the framework of NRQCD, without the introduction of any additional parameter.

- We have studied the hadroproduction of a J/ψ in association with a charm-quark pair. We have presented several observables that can be used to scrutinize the factorization principle of NRQCD, which is expected to break down for this signature at NNLO [50, 51].

Beside these specific calculations, we have presented an innovative approach in quarkonium production by suggesting to extend the set of observables analysed so far. In particular, one can gain some insights on the mechanisms at work by analysing not only the distribution of events with respect to the quarkonium energy or direction, but also the kinematics of the other particles in the events. This direction opens the door to many new and potentially interesting analyses that can be stimulated by Monte Carlo techniques. With this in mind, we have presented a quarkonium Monte Carlo generator, aimed at producing parton-level events in the NRQCD framework, for any phenomenologically relevant transition, at tree-level. The code can be interfaced with a program that takes care of the parton showering and the hadronization[2]. The hadron-level events can then be passed though an experiment-dependent code for the simulation of the detector. This automated generation of events up to the detector level can be used to simulate experimental analyses aimed at investigating the phenomenological pertinence of new theoretical ideas. Let us recall a few interesting features of the tool:

- we keep track of all spin correlation effects (see Sections 2.1.2, 2.2),

- we keep track of the heavy-quark mass effects, and hence take into account potentially large corrections that are ignored in the fragmentation approximation (see Section 2.3),

- our algorithm is general enough to handle the production of B_c mesons (see Section 2.1.4),

- quarkonium production beyond the standard model can readily be implemented.

[2] In our code we set up the interface with Pythia.

The events can be generated via a user-friendly web interface, accessible to all users, that parallelizes the jobs and run them on a cluster.

In the near future, we plan to extend the interface between our matrix-element based generator and a given parton shower algorithm to describe all multi-jet configurations at leading order. This approach has already been developed for other processes by making use of the *matching* proceedure [143, 144, 145, 146]: hard radiations are described by the matrix element, whereas soft radiations are generated by the parton-shower generator in such a way as to avoid the double counting of a given configuration. The predictions derived from this method are found to be in agreement with the data [147]. The matching procedure appears to be particularly relevant for inclusive hadroproduction of the J/ψ or the Υ via the color-singlet transition, given the importance of higher jet multiplicities (see Section 3.2.1). Further studies in this direction could improve the prediction for inclusive J/ψ or Υ production and decrease the theoretical uncertainties.

Bibliography

[1] J. J. Aubert et al. Experimental Observation of a Heavy Particle J. *Phys. Rev. Lett.*, 33:1404–1406, 1974.

[2] J. E. Augustin et al. Discovery of a Narrow Resonance in e+ e- Annihilation. *Phys. Rev. Lett.*, 33:1406–1408, 1974.

[3] S. W. Herb et al. Observation of a dimuon resonance at 9.5-GeV in 400-GeV proton - nucleus collisions. *Phys. Rev. Lett.*, 39:252–255, 1977.

[4] B. Aubert et al. Observation of the bottomonium ground state in the decay $\upsilon_{3S} \to \gamma eta_b$. *Phys. Rev. Lett.*, 101:071801, 2008.

[5] Stephen Godfrey and Stephen L. Olsen. The Exotic XYZ Charmonium-like Mesons. *Ann. Rev. Nucl. Part. Sci.*, 58:51–73, 2008.

[6] Johann H. Kuhn, Jean Kaplan, and El Ghali Oudrhiri Safiani. Electromagnetic Annihilation of e+ e- Into Quarkonium States with Even Charge Conjugation. *Nucl. Phys.*, B157:125, 1979.

[7] B. Guberina, Johann H. Kuhn, R. D. Peccei, and R. Ruckl. Rare Decays of the Z0. *Nucl. Phys.*, B174:317, 1980.

[8] Edmond L. Berger and Daniel L. Jones. Inelastic photoproduction of J/ψ and Υ by gluons. *Phys. Rev.*, D23:1521–1530, 1981.

[9] Wai-Yee Keung and I. J. Muzinich. BEYOND THE STATIC LIMIT FOR QUARKONIUM DECAYS. *Phys. Rev.*, D27:1518, 1983.

[10] Geoffrey T. Bodwin, Eric Braaten, and G. Peter Lepage. Rigorous QCD analysis of inclusive annihilation and production of heavy quarkonium. *Phys. Rev.*, D51:1125–1171, 1995.

[11] Geoffrey T. Bodwin, Eric Braaten, and G. Peter Lepage. Rigorous QCD predictions for decays of p wave quarkonia. 1992.

[12] Eric Braaten and Yu-Qi Chen. Dimensional regularization in quarkonium calculations. *Phys. Rev.*, D55:2693–2707, 1997.

[13] Michael Kramer. Quarkonium production at high-energy colliders. *Prog. Part. Nucl. Phys.*, 47:141–201, 2001.

[14] F. Maltoni et al. Analysis of charmonium production at fixed-target experiments in the NRQCD approach. *Phys. Lett.*, B638:202–208, 2006.

[15] A. Abulencia et al. Polarization of J/ψ and ψ_{2S} mesons produced in $p\bar{p}$ collisions at $\sqrt{s} = 1.96$ TeV. 2007.

[16] Torbjorn Sjostrand, Stephen Mrenna, and Peter Skands. PYTHIA 6.4 physics and manual. *JHEP*, 05:026, 2006.

[17] G. Corcella et al. HERWIG 6.5 release note. 2002.

[18] P. Artoisenet. J/ψ production in association with a charm-quark pair at the Tevatron. *Proceedings of 9th Workshop on Non-Perturbative Quantum Chromodynamics*, 2008.

[19] P. Artoisenet. QCD corrections to heavy quarkonium production. *AIP Conf. Proc.*, 1038:55–62, 2008.

[20] P. Artoisenet. Improved predictions for Υ hadroproduction. *Proceedings of DIS 2008*, 2008.

[21] J. P. Lansberg et al. Perspectives on heavy-quarkonium production at the LHC. *AIP Conf. Proc.*, 1038:15–44, 2008.

[22] Geoffrey T. Bodwin, Eric Braaten, and Jungil Lee. Comparison of the color-evaporation model and the NRQCD factorization approach in charmonium production. *Phys. Rev.*, D72:014004, 2005.

[23] T. Kinoshita. Mass singularities of Feynman amplitudes. *J. Math. Phys.*, 3:650–677, 1962.

[24] T. D. Lee and M. Nauenberg. Degenerate Systems and Mass Singularities. *Phys. Rev.*, 133:B1549–B1562, 1964.

[25] Andrea Petrelli, Matteo Cacciari, Mario Greco, Fabio Maltoni, and Michelangelo L. Mangano. NLO production and decay of quarkonium. *Nucl. Phys.*, B514:245–309, 1998.

[26] Eric Braaten and Yu-Qi Chen. Helicity Decomposition for Inclusive J/ψ Production. *Phys. Rev.*, D54:3216–3227, 1996.

[27] S. Catani and M. H. Seymour. The dipole formalism for the calculation of QCD jet cross sections at next-to-leading order. *Phys. Lett.*, B378:287–301, 1996.

[28] Gabor Somogyi and Zoltan Trocsanyi. A subtraction scheme for computing QCD jet cross sections at NNLO: integrating the subtraction terms I. *JHEP*, 08:042, 2008.

[29] Geoffrey T. Bodwin and Andrea Petrelli. Order v^4 corrections to S-wave quarkonium decay. *Phys. Rev.*, D66:094011, 2002.

[30] Geoffrey T. Bodwin, Eric Braaten, and G. Peter Lepage. Rigorous QCD analysis of inclusive annihilation and production of heavy quarkonium. *Phys. Rev.*, D51:1125–1171, 1995.

[31] Estia J. Eichten and Chris Quigg. Quarkonium wave functions at the origin. *Phys. Rev.*, D52:1726–1728, 1995.

[32] Eric Braaten, King-man Cheung, and Tzu Chiang Yuan. Z0 decay into charmonium via charm quark fragmentation. *Phys. Rev.*, D48:4230–4235, 1993.

[33] J. P. Ma. Quark fragmentation into p wave triplet quarkonium. *Phys. Rev.*, D53:1185–1190, 1996.

[34] Yu-Qi Chen. Perturbative QCD predictions for the fragmentation functions of the P wave mesons with two heavy quarks. *Phys. Rev.*, D48:5181–5189, 1993.

[35] Eric Braaten and Tzu Chiang Yuan. Gluon fragmentation into heavy quarkonium. *Phys. Rev. Lett.*, 71:1673–1676, 1993.

[36] Eric Braaten and Tzu Chiang Yuan. Gluon fragmentation into spin triplet S wave quarkonium. *Phys. Rev.*, D52:6627–6629, 1995.

[37] Eric Braaten and Tzu Chiang Yuan. Gluon fragmentation into P wave heavy quarkonium. *Phys. Rev.*, D50:3176–3180, 1994.

[38] Peter L. Cho, Mark B. Wise, and Sandip P. Trivedi. Gluon fragmentation into polarized charmonium. *Phys. Rev.*, D51:2039–2043, 1995.

[39] Bo Andersson et al. Small x phenomenology: Summary and status. *Eur. Phys. J.*, C25:77–101, 2002.

[40] Jeppe R. Andersen et al. Small x phenomenology: Summary and status 2002. *Eur. Phys. J.*, C35:67–98, 2004.

[41] S. P. Baranov. Probing the BFKL gluons with J/psi leptoproduction. *Phys. Lett.*, B428:377–382, 1998.

[42] Ph. Hagler, R. Kirschner, A. Schafer, L. Szymanowski, and O. V. Teryaev. Direct J/ψ hadroproduction in k^- perpendicular factorization and the color octet mechanism. *Phys. Rev.*, D63:077501, 2001.

[43] Feng Yuan and Kuang-Ta Chao. Polarizations of J/ψ and ψ' in hadroproduction at Tevatron in the k_t factorization approach. *Phys. Rev. Lett.*, 87:022002, 2001.

[44] P. Hagler, R. Kirschner, A. Schafer, L. Szymanowski, and O. V. Teryaev. Towards a solution of the charmonium production controversy: k^- perpendicular factorization versus color octet mechanism. *Phys. Rev. Lett.*, 86:1446–1449, 2001.

[45] S. P. Baranov. Highlights from the kT factorization approach on the quarkonium production puzzles. *Phys. Rev.*, D66:114003, 2002.

[46] A. V. Lipatov and N. P. Zotov. Inelastic J/psi production at HERA in the colour singlet model with k(T)-factorization. *Eur. Phys. J.*, C27:87–99, 2003.

[47] S. P. Baranov and N. P. Zotov. Production and polarization of υ mesons in the k_{T-} factorization approach in more detail. 2008.

[48] Gouranga C. Nayak, Jian-Wei Qiu, and George Sterman. Fragmentation, factorization and infrared poles in heavy quarkonium production. *Phys. Lett.*, B613:45–51, 2005.

[49] Gouranga C. Nayak, Jian-Wei Qiu, and George Sterman. Fragmentation, NRQCD and NNLO factorization analysis in heavy quarkonium production. *Phys. Rev.*, D72:114012, 2005.

[50] Gouranga C. Nayak, Jian-Wei Qiu, and George Sterman. Color transfer in associated heavy-quarkonium production. *Phys. Rev. Lett.*, 99:212001, 2007.

[51] Gouranga C. Nayak, Jian-Wei Qiu, and George Sterman. Color transfer enhancement for heavy quarkonium production. *Phys. Rev.*, D77:034022, 2008.

[52] Geoffrey T. Bodwin, Xavier Garcia i Tormo, and Jungil Lee. Factorization theorems for exclusive heavy-quarkonium production. *Phys. Rev. Lett.*, 101:102002, 2008.

[53] Yu-Jie Zhang, Yan-Qing Ma, and Kuang-Ta Chao. Factorization and NLO QCD correction in $e^+e^- \to J/\psi(\psi(2S)) + \chi_{c0}$ at B Factories. *Phys. Rev.*, D78:054006, 2008.

[54] T. Stelzer and W. F. Long. Automatic generation of tree level helicity amplitudes. *Comput. Phys. Commun.*, 81:357–371, 1994.

[55] Kingman Cheung and Wai-Yee Keung. Split supersymmetry, stable gluino, and gluinonium. *Phys. Rev.*, D71:015015, 2005.

[56] William Shepherd, Tim M. P. Tait, and Gabrijela Zaharijas. WIMPonium. 2009.

[57] K. Hagiwara, E. Kou, Z. H. Lin, C. F. Qiao, and G. H. Zhu. Inclusive J/ψ productions at e^+e^- colliders. *Phys. Rev.*, D70:034013, 2004.

[58] P. Artoisenet, J. P. Lansberg, and F. Maltoni. Hadroproduction of J/ψ and Υ in association with a heavy-quark pair. *Phys. Lett.*, 653:60, 2007.

[59] F. Maltoni, K. Paul, T. Stelzer, and S. Willenbrock. Color-flow decomposition of QCD amplitudes. *Phys. Rev.*, D67:014026, 2003.

[60] H. Murayama, I. Watanabe, and K. Hagiwara. HELAS: Helicity amplitude subroutines for feynman diagram evaluations. KEK-91-11.

[61] M. Beneke and I. Z. Rothstein. Psi' polarization as a test of colour octet quarkonium production. *Phys. Lett.*, B372:157–164, 1996.

[62] Adam K. Leibovich. Psi' polarization due to color-octet quarkonia production. *Phys. Rev.*, D56:4412–4415, 1997.

[63] Geoffrey T. Bodwin, Daekyoung Kang, Taewon Kim, Jungil Lee, and Chaehyun Yu. Relativistic corrections to $e^+e^- \to J/\psi + \eta_c$ in a potential model. *AIP Conf. Proc.*, 892:315–317, 2007.

[64] Geoffrey T. Bodwin, Daekyoung Kang, and Jungil Lee. Potential-model calculation of an order-v^2 NRQCD matrix element. *Phys. Rev.*, D74:014014, 2006.

[65] Peter L. Cho and Adam K. Leibovich. Color-octet quarkonia production II. *Phys. Rev.*, D53:6203–6217, 1996.

[66] Peter L. Cho and Adam K. Leibovich. Color octet quarkonia production. *Phys. Rev.*, D53:150–162, 1996.

[67] Bernd A. Kniehl, Caesar P. Palisoc, and Lennart Zwirner. Associated production of heavy quarkonia and electroweak bosons at present and future colliders. *Phys. Rev.*, D66:114002, 2002.

[68] Bernd A. Kniehl, Caesar P. Palisoc, and Lennart Zwirner. Associated production of bottomonia and higgs bosons at hadron colliders. *Phys. Rev.*, D69:115005, 2004.

[69] C. H. Chang, C. Driouichi, P. Eerola, and X. G. Wu. Bcvegpy: An event generator for hadronic production of the B_c meson. *Comput. Phys. Commun.*, 159:192, 2004.

[70] C. H. Chang, J. X. Wang, and X. G. Wu. Bcvegpy2.0: A upgrade version of the generator bcvegpy with an addendum about hadroproduction of the P-wave B_c states. *Comput. Phys. Commun.*, 174:241, 2006.

[71] A. V. Berezhnoy, V. V. Kiselev, and A. K. Likhoded. Non-abelian nature of asymmetry in the production of B_c mesons in gluon photon interactions. *Phys. Atom. Nucl.*, 61:252–259, 1998.

[72] A. V. Berezhnoi, A. K. Likhoded, and M. V. Shevlyagin. Photonic production of B_c mesons. *Phys. Lett.*, B342:351–355, 1995.

[73] A. V. Berezhnoi, V. V. Kiselev, and A. K. Likhoded. Photonic production of the P-wave states of B_c mesons. *Phys. Lett.*, B381:341–347, 1996.

[74] Eric Braaten and Jungil Lee. Exclusive double-charmonium production in e^+e^- annihilation. *Phys. Rev.*, D67:054007, 2003.

[75] Kui-Yong Liu, Zhi-Guo He, and Kuang-Ta Chao. Search for excited charmonium states in e^+e^- annihilation at $\sqrt{s} = 10.6$ GeV. *Phys. Rev.*, D77:014002, 2008.

[76] K. Abe et al. Observation of double c anti-c production in e+ e- annihilation at $\sqrt{s} \approx 10.6$ GeV. *Phys. Rev. Lett.*, 89:142001, 2002.

[77] B. Aubert et al. Measurement of double charmonium production in e^+e^- annihilations at $\sqrt{s} = 10.6$ GeV. *Phys. Rev.*, D72:031101, 2005.

[78] R. Mertig, M. Bohm, and Ansgar Denner. FEYN CALC: Computer algebraic calculation of Feynman amplitudes. *Comput. Phys. Commun.*, 64:345–359, 1991.

[79] M. Beneke, M. Kramer, and M. Vanttinen. Inelastic photoproduction of polarised J/ψ. *Phys. Rev.*, D57:4258–4274, 1998.

[80] Eric Braaten, Michael A. Doncheski, Sean Fleming, and Michelangelo L. Mangano. Fragmentation production of J/ψ and ψ' at the Tevatron. *Phys. Lett.*, B333:548–554, 1994.

[81] Matteo Cacciari and Mario Greco. J / psi production via fragmentation at the Tevatron. *Phys. Rev. Lett.*, 73:1586–1589, 1994.

[82] Cong-Feng Qiao and Jian-Xiong Wang. J/ψ + c + $\bar{c}$ photoproduction in e^+e^- scattering. *Phys. Rev.*, D69:014015, 2004.

[83] Chao-Hsi Chang, Yu-Qi Chen, Guo-Ping Han, and Hong-Tan Jiang. On hadronic production of the B(c) meson. *Phys. Lett.*, B364:78–86, 1995.

[84] A. V. Berezhnoi, V. V. Kiselev, and A. K. Likhoded. Hadronic production of S- and P- wave states of anti-b c quarkonium. *Z. Phys.*, A356:79–87, 1996.

[85] G. Peter Lepage. VEGAS: AN ADAPTIVE MULTIDIMENSIONAL INTEGRATION PROGRAM. CLNS-80/447.

[86] Costas G. Papadopoulos. PHEGAS: A phase space generator for automatic cross- section computation. *Comput. Phys. Commun.*, 137:247–254, 2001.

[87] F. Krauss, R. Kuhn, and G. Soff. AMEGIC++ 1.0: A matrix element generator in C++. *JHEP*, 02:044, 2002.

[88] Ronald Kleiss and Roberto Pittau. Weight optimization in multichannel Monte Carlo. *Comput. Phys. Commun.*, 83:141–146, 1994.

[89] Johan Alwall et al. MadGraph/MadEvent v4: The New Web Generation. *JHEP*, 09:028, 2007.

[90] Fabio Maltoni and Tim Stelzer. Madevent: Automatic event generation with MadGraph. *JHEP*, 02:027, 2003.

[91] J. Campbell, F Maltoni, and F Tramontano. QCD corrections to J/ψ and Υ production at hadron colliders. *Phys. Rev. Lett.*, 98:252002, 2007.

[92] R. Keith Ellis and Sinisa Veseli. Strong radiative corrections to W b anti-b production in p anti-p collisions. *Phys. Rev.*, D60:011501, 1999.

[93] S. Catani and M. H. Seymour. A general algorithm for calculating jet cross sections in NLO QCD. *Nucl. Phys.*, B485:291–419, 1997.

[94] Bob McElrath. Invisible quarkonium decays as a sensitive probe of dark matter. *Phys. Rev.*, D72:103508, 2005.

[95] M. L. Mangano and P. Nason. Radiative quarkonium decays and the NMSSM Higgs interpretation of the hyperCP $\Sigma^+ \to p\mu^+\mu^-$ events. *Mod. Phys. Lett. A*, 22:1373, 2007.

[96] Bob McElrath. Light higgses and dark matter at bottom and charm factories. 2007.

[97] Miguel-Angel Sanchis-Lozano. A light non-standard higgs boson: to be or not to be at a (super) b factory? 2007.

[98] P Nason. QCD radiative corrections to Υ decay into scalar $+\gamma$ and pseudoscalar $+\gamma$. *Phys.Lett.B*, 175:223, 1986.

[99] M. Klasen, Bernd A. Kniehl, L. N. Mihaila, and M. Steinhauser. Evidence for colour-octet mechanism from CERN LEP2 $\gamma\gamma \to J/\psi + X$ data. *Phys. Rev. Lett.*, 89:032001, 2002.

[100] K. Abe et al. Study of double charmonium production in e^+e^- annihilation at $\sqrt{s} \approx 10.6$ GeV. *Phys. Rev.*, D70:071102, 2004.

[101] N. Brambilla et al. Heavy quarkonium physics. 2004.

[102] Yu-Jie Zhang, Ying-jia Gao, and Kuang-Ta Chao. Next-to-leading order QCD correction to e+ e- –> J/psi + eta/c at s**(1/2) = 10.6-GeV. *Phys. Rev. Lett.*, 96:092001, 2006.

[103] Bin Gong and Jian-Xiong Wang. QCD corrections to J/ψ plus η_c production in e^+e^- annihilation at $S^{(1/2)}$ = 10.6-GeV. *Phys. Rev.*, D77:054028, 2008.

[104] A. E. Bondar and V. L. Chernyak. Is the BELLE result for the cross section $\sigma(e^+e^- \to J/\psi + \eta_c)$ a real difficulty for QCD? *Phys. Lett.*, B612:215–222, 2005.

[105] Geoffrey T. Bodwin, Daekyoung Kang, and Jungil Lee. Reconciling the light-cone and NRQCD approaches to calculating $e^+e^- \to J/\psi + \eta_c$. *Phys. Rev.*, D74:114028, 2006.

[106] Geoffrey T. Bodwin, Jungil Lee, and Chaehyun Yu. Resummation of Relativistic Corrections to $e^+e^- \to J/\psi + \eta_c$. *Phys. Rev.*, D77:094018, 2008.

[107] T. V. Uglov. Double production at Belle. *Eur. Phys. J.*, C33:s235–s237, 2004.

[108] P. Pakhlov et al. Measurement of the $e + e - - > J/psic\bar{c}$ cross section at $\sqrt{s}\ 10.6GeV$. 2009.

[109] Seungwon Baek, P. Ko, Jungil Lee, and H. S. Song. Color octet mechanism and J/ψ polarization at LEP. *Phys. Rev.*, D55:6839–6843, 1997.

[110] Kui-Yong Liu, Zhi-Guo He, and Kuang-Ta Chao. Inclusive charmonium production via double $c\bar{c}$ in e^+e^- annihilation. *Phys. Rev.*, D69:094027, 2004.

[111] Yu-Jie Zhang and Kuang-Ta Chao. Double charm production $e^+e^- \to J/\psi + c\bar{c}$ at B factories with next-to-leading order QCD correction. *Phys. Rev. Lett.*, 98:092003, 2007.

[112] Yan-Qing Ma, Yu-Jie Zhang, and Kuang-Ta Chao. QCD correction to $\boldsymbol{e^+e^- \to J/\psi gg}$ at B Factories. 2008.

[113] Zhi-Guo He, Ying Fan, and Kuang-Ta Chao. Relativistic corrections to j/ψ exclusive and inclusive double charm production at B factories. *Phys. Rev.*, D75:074011, 2007.

[114] C. Amsler et al. Review of particle physics. *Phys. Lett.*, B667:1, 2008.

[115] F. Abe et al. Production of J/ψ mesons from χ_c meson decays in $p\bar{p}$ collisions at $\sqrt{s} = 1.8$ TeV. *Phys. Rev. Lett.*, 79:578–583, 1997.

[116] Anthony Allen Affolder et al. Production of $\Upsilon(1S)$ mesons from χ_b decays in $p\bar{p}$ collisions at $\sqrt{s} = 1.8$ TeV. *Phys. Rev. Lett.*, 84:2094–2099, 2000.

[117] J. P. Lansberg. J/ψ, ψ' and Υ production at hadron colliders: A review. *Int. J. Mod. Phys.*, A21:3857–3916, 2006.

[118] Martin Beneke and Michael Kramer. Direct J/ψ and ψ' polarization and cross-sections at the Tevatron. *Phys. Rev.*, D55:5269–5272, 1997.

[119] Eric Braaten, Bernd A. Kniehl, and Jungil Lee. Polarization of prompt J/ψ at the Tevatron. *Phys. Rev.*, D62:094005, 2000.

[120] Eric Braaten, Sean Fleming, and Adam K. Leibovich. NRQCD analysis of bottomonium production at the tevatron. *Phys. Rev.*, D63:094006, 2001.

[121] Eric Braaten and Jungil Lee. Polarization of υ_{nS} at the Tevatron. *Phys. Rev.*, D63:071501, 2001.

[122] Ying Fan, Yan-Qing Ma, and Kuang-Ta Chao. Relativistic Correction to J/ψ Production at Hadron Colliders. 2009.

[123] Bin Gong and Jian-Xiong Wang. QCD corrections to J/psi polarization of hadronproduction at Tevatron and LHC. 2008.

[124] P. Artoisenet, John M. Campbell, J. P. Lansberg, F. Maltoni, and F. Tramontano. υ Production at Fermilab Tevatron and LHC Energies. *Phys. Rev. Lett.*, 101:152001, 2008.

[125] J. Pumplin et al. New generation of parton distributions with uncertainties from global QCD analysis. *JHEP*, 07:012, 2002.

[126] Darin E. Acosta et al. Measurement of the J/ψ meson and $b-$hadron production cross sections in $p\bar{p}$ collisions at $\sqrt{s} = 1960$ GeV. *Phys. Rev.*, D71:032001, 2005.

[127] Darin E. Acosta et al. Upsilon production and polarization in $p\bar{p}$ collisions at $\sqrt{s} = 1.8$-TeV. *Phys. Rev. Lett.*, 88:161802, 2002.

[128] T. Aaltonen et al. Production of psi(2S) Mesons in ppbar Collisions at 1.96 TeV. 2009.

[129] J. P. Lansberg, J. R. Cudell, and Yu. L. Kalinovsky. New contributions to heavy-quarkonium production. *Phys. Lett.*, B633:301–308, 2006.

[130] P. Artoisenet and E. Braaten. Charm Pair rescattering Mechanism for Charmonium Production in High-energy Collisions. *arXiv:0907.0025*, 2009.

[131] J. P. Lansberg and H. Haberzettl. J/ψ production at the Tevatron and RHIC from s^- channel cut. *AIP Conf. Proc.*, 1038:83–92, 2008.

[132] A. D. Martin, R. G. Roberts, W. J. Stirling, and R. S. Thorne. NNLO global parton analysis. *Phys. Lett.*, B531:216–224, 2002.

[133] Darin E. Acosta et al. Measurement of prompt charm meson production cross sections in $p\bar{p}$ collisions at $\sqrt{s} = 1.96$ TeV. *Phys. Rev. Lett.*, 91:241804, 2003.

[134] Bin Gong, Xue Qian Li, and Jian-Xiong Wang. QCD corrections to J/ψ production via color octet states at Tevatron and LHC. *Phys. Lett.*, B673:197–200, 2009.

[135] Eric Braaten, Daekyoung Kang, Jungil Lee, and Chaehyun Yu. Optimal spin quantization axes for quarkonium with large transverse momentum. 2008.

[136] S. Chekanov et al. Measurements of inelastic J/psi and psi' photoproduction at HERA. *Eur. Phys. J.*, C27:173–188, 2003.

[137] C. Adloff et al. Inelastic photoproduction of J/psi mesons at HERA. *Eur. Phys. J.*, C25:25–39, 2002.

[138] A. Aktas et al. Diffractive photoproduction of J/psi mesons with large momentum transfer at HERA. *Phys. Lett.*, B568:205–218, 2003.

[139] M. Beneke, I. Z. Rothstein, and Mark B. Wise. Kinematic enhancement of non-perturbative corrections to quarkonium production. *Phys. Lett.*, B408:373–380, 1997.

[140] M. Gluck, E. Reya, and A. Vogt. Photonic parton distributions. *Phys. Rev.*, D46:1973–1979, 1992.

[141] Michael Kramer. QCD corrections to inelastic J/ψ photoproduction. *Nucl. Phys.*, B459:3–50, 1996.

[142] ZEUS Collaboration. Measurement of J/ψ helicity distributions in inelastic photoproduction at HERA. 2009.

[143] S. Catani, F. Krauss, R. Kuhn, and B. R. Webber. QCD matrix elements + parton showers. *JHEP*, 11:063, 2001.

[144] F. Krauss. Matrix elements and parton showers in hadronic interactions. *JHEP*, 08:015, 2002.

[145] Leif Lonnblad. Correcting the colour-dipole cascade model with fixed order matrix elements. *JHEP*, 05:046, 2002.

[146] Michelangelo L. Mangano, Mauro Moretti, Fulvio Piccinini, and Michele Treccani. Matching matrix elements and shower evolution for top- quark production in hadronic collisions. *JHEP*, 01:013, 2007.

[147] J. Alwall et al. Comparative study of various algorithms for the merging of parton showers and matrix elements in hadronic collisions. *Eur. Phys. J.*, C53:473–500, 2008.